SpringerBriefs in Physics

For further volumes:
http://www.springer.com/series/8902

Vladimir G. Plekhanov

Isotope Low-Dimensional Structures

Elementary Excitations and Applications

Springer

Vladimir G. Plekhanov
Mathematics and Physics Department
Computer Science College
Erika Street 7a
10416 Tallinn
Estonia

ISSN 2191-5423 ISSN 2191-5431 (electronic)
ISBN 978-3-642-28612-4 ISBN 978-3-642-28613-1 (eBook)
DOI 10.1007/978-3-642-28613-1
Springer Heidelberg New York Dordrecht London

Library of Congress Control Number: 2012936757

Printed on acid-free paper

Springer is part of Springer Science+Business Media (www.springer.com)

Preface

The experience of the past shows that throughout constant technology improvement electronics (*optoelectronics*) has become more reliable, faster, more powerful, and less expensive by reducing the dimensions of integrated circuits. These advantages will lead to the development of modern microelectronics. The long-term goal of this development will lead to *nanoelectronics*. Advancing to the nanoscale is not just a step toward miniaturization, but requires the introduction and consideration of many additional phenomena. At the *nanoscale*, most phenomena and processes are dominated by quantum physics and they exhibit unique behavior. *Nanotechnology* includes the integration of man-made nanostructures into larger material components and systems (see, e.g. [1–4]). Importantly, within these larger scale systems, the active elements of the system will remain at nanoscale.

Low-dimensional structures have become one of the most active research not only in nanoscience and nanotechnology but also isotopetronics. Quantum wells, quantum wires, and quantum dots structures produced in the main by epitaxial growth techniques (mainly molecular beam epitaxy (MBE) and metal-organic chemical vapor deposition (MOCVD) and their various variations such as chemical beam epitaxy (CBE), atomic layer epitaxy (ALE), etc. (see, e.g. [5–10]). MBE and MOCVD are of considerable technological interest since they are used as active components in modern devices. These devices are high-electron-mobility transistors, diodes and lasers, as well as quantum dots from quantum computations and communications perspectives.

The seminal works of Esaki and Tsu [11] and others on the semiconductor superlattice stimulated a vast international research effort to understand the fabrication and electronic properties of superlattice, quantum wells, quantum wires, and quantum dots (see, for example, [1–4]). The dimensional scale of such samples between 10 and 100 nm which are the subject of *nanoscience*—is a broad and interdisciplinary field of emerging research and development. Nanoscience and nanotechnology are concerned with materials, structures, and systems whose components exhibit novel and significantly modified physical, chemical properties

due to their nanoscale sizes. The new direction of nanoscience is isotope-engineered materials, which is studied the more low-dimensional in size, as a rule the sizes of the sample of isotope-engineered materials compare with the atomic size. *Nuclear* technology—neutron irradiation [12]—is a very useful method for preparing low-dimensional structure: quantum wells, quantum wires, and quantum dots [13]. A principal goal of isotope-engineered materials as new directions of the nanotechnology is to control and exploit their new properties in structures and devices at atomic, three molecular, and supramolecular levels. The minituarization required by modern electronics is one of the driving forces for isotope-engineered materials (*isotopetronics*)—new direction of nanotechnology (see, also [14]).

Modern *nanoscience* and *nanotechnology* is a fertile ground for teaching, as it brings together the quantum theory of materials, novel physics in the electronic and optical properties of solids, the engineering of small structures, and the design of high performance electronic, photonic, and optoelectronic systems. The treatments attempt to be introductory, comprehensive, and phenomenological in the main. The new physics described in this book comes from one important consideration—length scale (see, also [1, 2, 15, 16]) especially in *mesoscopic* physics. As we all know, mesoscopic physics deals with structures which have a size between the macroscopic and the microscopic or atomic one. These structures are also called mesoscopic systems, or nanostructures [3] in a more colloquial way since their size usually ranges from a few nanometers to about 100 nm. The electrons in such mesoscopic systems show their wavelike properties [15, 16] and therefore their behavior is markedly dependent on the geometry of the samples. In this case, the states of the electrons are wave-like and somewhat similar to electromagnetic waves (see, e.g. [16]).

As mentioned above for the description of the behavior of electrons in solids, it is very convenient to define a series of characteristic lengths. If the dimension of the solids in which the electron embedded is of the order of, or smaller than these characteristic lengths (λ_B de Broglie wavelength, or a_{ex}—exciton radius, etc.) the material might show new properties, which in general are more interesting than the corresponding ones in macroscopic materials. On the contrary, a mesoscopic system approaches its macroscopic limit if its size is several times its characteristic length.

As mentioned above, when the dimensions of the solid get reduced to a size comparable with, or smaller λ_B, then the particles behave wavelike and quantum mechanics should be used. Let us suppose that we have an electron confined within a box of dimensions L_x, L_y, L_z. If the characteristic length is l, we can have the following situations:

1. $l \langle L_x, L_y, L_z$. In this case the electron behaves as in regular 3D bulk *semiconductor* (*insulator*).
2. $l \rangle L_x$ and $L_x \langle\langle L_y, L_z$. In this situation we have a 2D semiconductor perpendicular to the x-axis. This mesoscopic system is also called a quantum well (for details see Chap. 3).

3. $l \rangle L_x$, L_y and L_x, $L_y \langle\langle L_z$. This case corresponds to a 1D semiconductor or quantum wire, located along the z-axis.
4. $l \rangle\rangle L_x$, L_y, L_z. In this case it is said that we have a 0D or a quantum dot [1, 2].

In general, we say in mesoscopic physics that a solid, very often a crystal, is of reduced dimensionality if at least one of its dimensions L_i is smaller than the characteristic length. For instance, if L_x and L_y are smaller than l we have a crystal of dimensionality equal to one. We could also have the case that l is comparable, or a little larger, than one of the dimensions of the solid but much smaller than the other two. Then we have a quasi 2D system, which in practice is a very thin film, but not thin enough to show quantum size effect (for details see Chap. 3).

This review is organized into four chapters. In Chap. 1, I review the present status of elementary excitations in solids. Preparation methods of low-dimensional structures are described in Chap. 2. Chapter 3 deals with physics of low-dimensional structure. In this chapter of the most frequently structures—quantum dots are revised. The applications of low-dimensional structures is done in Chap. 4.

Tallinn Vladimir G. Plekhanov

Acknowledgments

Many thanks are due to Prof. W. Reder for carefully reading the manuscript as well as to Dr. N. Write for improving my English. I appreciate the invaluable help given by Mr. M. T. Kivi (Dr. of Medicine) during my difficult period. Again it is a pleasure to thank the Staff of Springer, in particular Dr. C. Ascheron and Elke Sauer, for the continued excellent cooperation. I deeply thank the authors and publishers who have kindly permitted us to reproduce figures and tables from their papers and books. In a few cases I have been unable to contact the authors, and I would be grateful if they would nevertheless retrospectively give me the necessary permission. I wish to express my deep gratitude to my family for their patience during the long preparation of this book.

Tallinn Vladimir G. Plekhanov

Contents

Chapter 1
Elementary Excitations of Isotope: Mixed Crystals

1.1 Introduction

The modern view of solid-state physics is based on the presentation of *elementary excitations*, having mass, quasiimpuls, electrical charge and so on (see, e.g. [17]). According to this presentation the elementary excitations of non-metallic materials are *electrons* (*holes*), *excitons* (*polaritons* [18]), and *phonons* [19]. The latter are the elementary excitations of the crystal lattice, the dynamics of which is described in harmonic approximation (see e.g. [20]). As is well known, the basis of such a view on solids is the multiparticle approach. In such a view, the quasiparticles of solids are ideal gas, which describe the behavior of the system, e.g. noninteracting electrons. We should include such approach to consider the theory of elementary excitations as a suitable model for the application of the common methods of quantum mechanics for the solution of solid-state physics tasks. In this part of our review we briefly consider not only the manifestations of the isotope effect in different solids, but also bring the new accurate results, showing the quantitative changes of different characteristics of phonons and electrons (excitons) in solids with isotopical substitution (see, also [21]). The isotopic effect becomes more pronounced when we deal with solids. For example, on substitution of H with D the change in energy of the electron transition in solid state (e.g. LiH) is two orders of magnitude larger than in atomic hydrogen (see, e.g. [22]). The use of elementary excitations to describe the complicated motion of many particles has turned out to be an extraordinarily useful device in contemporary physics, and it is the view of a solid which we describe in this part of the book.

The basic Hamiltonian of our solid model is of the form [21]

$$\mathrm{H} = \mathrm{H}_{\mathrm{ion}} + \mathrm{H}_{\mathrm{electron}} + \mathrm{H}_{\mathrm{electron-ion}} \tag{1.1}$$

where

$$\mathrm{H}_{\mathrm{ion}} = \sum_i \frac{p_i^2}{2m} + \frac{1}{2}\sum_{i \neq j} V(R_i - R_j), \tag{1.2}$$

V. G. Plekhanov, *Isotope Low-Dimensional Structures*, SpringerBriefs in Physics,
DOI: 10.1007/978-3-642-28613-1_1, © The Author(s) 2012

$$\mathrm{H_{electron}} = \sum_i \frac{p_i^2}{2m} + \frac{1}{2}\sum_{i\neq j} \frac{\mathrm{e}^2}{|r_i - r_j|}, \tag{1.3}$$

$$\mathrm{H_{electron-ion}} = \sum_{i,j} \mathrm{v}(\mathrm{r}_i - \mathrm{R}_j). \tag{1.4}$$

$\mathrm{H_{ion}}$ describes a collection of ions (of a single species) which interacts through a potential $\mathrm{V}(\mathrm{R}_i - \mathrm{R}_j)$ and which depends only on the distance between ions. By ion we mean a nucleus plus the closed-shell, or core, electrons, that is, those electrons that are essentially unchanged when the atoms are brought together to make a solid. $\mathrm{H_{electron}}$ presents the valence electrons (the electrons outside the last closed shell), which are assumed to interact via a *Coulomb* interaction. Finally, $\mathrm{H_{electron-ion}}$ describes the interaction between the electrons (excitons) and the ions, which is again assumed to be represented by a suitable chosen potential.

In adopting (1.1) as our basic Hamiltonian, we have already made a number of approximations in the treatment of a solid. Thus, in general the interaction between ions is not well—represented by a potential V(R), when the coupling between the closed-shell electrons on different ions begins to play an important role (see, e.g. [23, 24]). Again, in using a potential to represent electron–ion interaction, we have neglected the fact that the ions possess a structure (the core electrons); again, when the Pauli principle plays an important role in the interaction between the valence electrons, that interaction may no longer be represented by a simple potential. It is desirable to consider the validity of these approximations in detail (for details see, e.g. [24]). In general, one studies only selected parts of the Hamiltonian (1.1). Thus, for example, the band theory of solids is based upon the model Hamiltonian [23, 24]

$$\mathrm{H}_B = \sum_i \frac{p_i^2}{2m} + \sum_{i,j} \mathrm{v}(\mathrm{r}_i - \mathrm{R}_{j0}) + \mathrm{V_H}(\mathrm{r}_i), \tag{1.5}$$

where R_{j0} represents the fixed equilibrium positions of the ions and the potential V_H describes the (periodic) Hartree potential of the electrons. One studies the motion of a single electron in the periodic field of the ions and the Hartree potential, and takes the Pauli principle into account in the assignment of one-electron states. In so doing one neglects aspects other than the Hartree potential of the interaction between electrons. On the other hand, where one is primarily interested in understanding the interaction between electrons in metals, it is useful to consider only (1.3), replacing the effect of the ion cores by a uniform distribution of positive charge [25]. In this way one can approximate the role that electron interaction plays without having present the additional complications introduced by the periodic ion potential. Of course one wants finally to keep both the periodic ion potential and the electron interactions, and to include also the effects associated with departure of the ions from the equilibrium positions, since only in this way one does not arrive at a generally adequate description of the solid. Usually for the elementary excitations in solids

this is by first considering various different parts of the Hamiltonian (1.1) and then taking into account the remaining terms which act to couple different excitations.

1.2 Energy Band Structure

As mentioned above, the detailed study of the electronic band structure is the key to understand the behavior of electrons in solids, as well as their interaction with the lattice vibrations (phonons). The properties of a solid containing of the order of 10^{23} atoms/cm^3 are very complicated to predict. Several approaches to solve this problem were followed in the past providing a great amount of work in this field [23, 24]. For example, calculations of the band structure were performed using methods as $\vec{k} \cdot \vec{p}$, tight binding or LCAO, pseudo potentials, etc. (for details, see [23–26]).

Below, a simple basic frame to understand the electronic properties of crystal will be presented. It is not the author's purpose to give a detailed derivation of the fundamental equations governing the band structure, but to present the main ideas to understand the physical origin of the electronic band structure, phonon dispersion relations, and *electron–phonon interactions*, responsible, for instance, for the *Raman effect* (see also [20]).

First, we write the Hamiltonian describing a perfect crystal as [26]:

$$H = \sum_i \frac{p_i^2}{2m_i} + \sum_j \frac{P_j^2}{2M_j} + \frac{1}{2}\bar{\sum_{j'j}} \frac{Z_j Z_{j'} e^2}{4\pi\varepsilon_0 |R_j - R_{j'}|} - \sum_{ji} \frac{Z_j e^2}{4\pi\varepsilon_0 |r_i - R_j|} + \frac{1}{2}\sum_{ij} \frac{e^2}{4\pi\varepsilon_0 |r_i - r_j|}, \tag{1.6}$$

where r_i is the position of the ith electron, R_j the position of the jth nucleus, Z is the atomic number of the nucleus, p_i and P_j are the momentum operators of the electron and nucleus, respectively, e is the electronic charge, and $\bar{\sum}$ means that the summation is only over pairs of indices which are not identical. This many-particle Hamiltonian cannot be solved without a large list of simplifications:

1. **Valence electron approximation**. In the valence electron approximation we reduce the number of electrons, neglecting the core electrons [26]. We will take advantage of the fact that the core electrons are tightly bound to the nucleus forming the so-called ion core. Thus, the core electrons will no longer appear explicitly. For example, in the case of Si the electronic structure can be written as $1s^2 2s^2 2p^6 3s^2 3p^2$, where the 3s and 3p electrons are the only ones that hold are taken into account (see, also [27]).

2. **Born-Oppenheimer or adiabatic approximation [28]**. This approximation relies on the fact that ions are much heavier than electrons so they move much slowly.

Typically, the energy scales involved in the ionic motion is of the order of tens of meV, whereas the excitation energies for electrons is of the order of 1 eV. Converting these values into frequencies we obtain 10^{13} and $10^{15}\,\mathrm{s}^{-1}$ for lattice and electron vibrations, respectively. That is, the electronic frequencies are two orders of magnitude larger than the ionic vibrations, therefore the electrons 'see' the ions essentially stationary. Based on this we rewrite the Hamiltonian in Eq. (1.6) decoupling in part the movement of the electrons from that of the lattice as (see also [29]) was done above in Eq. (1.1). The purely electronic contribution to the Hamiltonian (1.1) $\mathrm{H}_{\mathrm{electron}}$ is the one responsible for the electronic excitation spectra in crystals, but still another approximation must be done in order to deal with the problem.

3. **Mean field approximation**. Taking only the electronic part in Eq. (1.1), we rewrite it as follows:

$$\mathrm{H}_e = \sum_i \frac{p_i^2}{2m_i} + \frac{1}{2}\sum_{i,i'}^{-} \frac{\mathrm{e}^2}{4\pi\varepsilon_0|\mathrm{r}_i - \mathrm{r}_{i'}|} - \sum_{i,j} \frac{\mathrm{Z}_j\mathrm{e}^2}{4\pi\varepsilon_0|\mathrm{r}_i - \mathrm{R}_{j0}|}, \tag{1.7}$$

where the first term is the kinetic energy of the electrons, the second is the *Coulomb* repulsion between electrons, and the last term is the Coulomb attraction between the nucleus in their equilibrium positions and the electrons. The mean field approximation replaces the Colombian terms in (1.7) by an average potential (see, e.g. [24]). The resulting Hamiltonian is given by:

$$\mathrm{H}_e = \sum_i \left[\frac{p_i^2}{2m_i} + \mathrm{V}(\mathrm{r}_i)\right] \Rightarrow \mathrm{H}_{1e} = \frac{p^2}{2m} + \mathrm{V}(\mathrm{r}), \tag{1.8}$$

where H_{1e} is the one-electron Hamiltonian and V(r) is the average potential. The first term in (1.8) is the free-electron Hamiltonian with plane waves as solutions. The energy spectrum is described by a parabolic dispersion relation as $\mathrm{E} = \frac{\hbar^2 k^2}{2m}$. The presence of the potential V(r) gives to the opening of the gap, and to the typical band structure of solid (see e.g. [26]). In order to obtain quantitative results, the one-electron potential V(r) is obtained, for example, using first principle calculations or semi-empirical methods.

The last step to obtain the band structure of solid is to take into account the rotational and translational symmetry of the crystalline structure. In this way, the wave functions that are solutions of (1.8) must have the same symmetry as the crystalline structure. By using group theory [30] it is possible to obtain these symmetries for each lattice structure and, thus, for the wave functions. Figure 1.1 shows the calculated band structure for Si in some highly symmetric directions of the *Brillouin zone*. As observed in this figure, the band structure of Si is indirect since the minimum transition energy is not at the zone center but in the $\Gamma \longrightarrow \mathrm{X}$.

The dependence of the band gap energy on *isotopic composition* has already been observed for insulators and lowest (indirect–direct) gap of different semiconductors (see also [22]). It has been shown to result primarily from the effect of the aver-

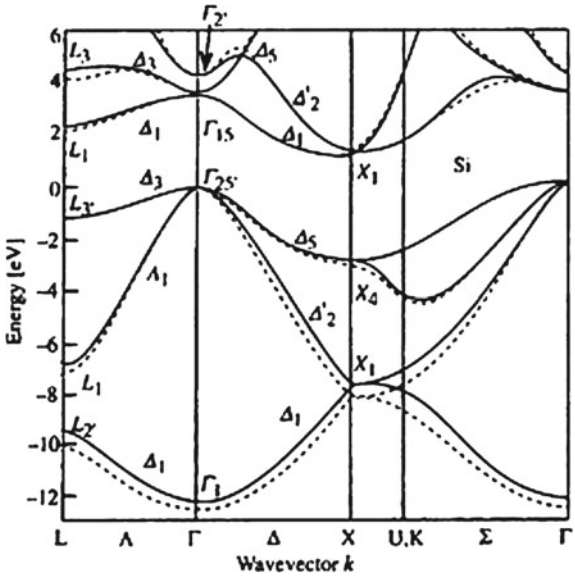

Fig. 1.1 Electronic band structure of Si calculated by pseudopotential technique. The *solid* and the *dotted lines* represent calculations with a nonlocal and a local pseudopotential, respectively (after [27])

age isotopic mass on the electron-phonon interaction (for details see below), with a smaller contribution from the change in lattice constant. This simplest approximation, in which crystals of mixed isotopic composition are treated as crystals of identical atoms having the average isotopic mass is referred to as *virtual crystal approximation* (*VCA*). Going beyond the VCA, in isotopically mixed crystals one would also expect local fluctuations in the band gap energy from statistical fluctuations in local isotopic composition within some effective volume, such as that of an exciton. Figure 91 of [31] shows the concentration dependence of the energy of interband transition E_g. As can be seen from this figure the VCA method cannot describe the observed experimental results. By now the change in E_g caused by isotopic substitution has been observed for many broad-gap and narrow-gap compounds (see Table 1.1). In Table 1.1 the variation of E_g and $\partial E_g / \partial M$ are shown at the isotopic effect. We should hihglight here that the most prominent isotope effect is observed in LiH crystal (see, also [22]).

1.3 Phonon States and Raman Spectra

The simplest kind of motion in solids is the vibration of atoms around the equilibrium point. The interaction of the crystal forming particles with one another at the move of one atom entangles neighbor atoms [20]. The analysis of this kind of motion shows that the elementary form of motion is the wave of the atom displacement. As is well known the quantization of the vibrations of the crystal lattice and after introduction of

Table 1.1 Values of the coefficients $\partial E_g/\partial M$ (meV) and energies of the band-to-band transitions E_g (eV) according to indicated references (after [22])

Substance	$\partial E_g/\partial M$ (meV)	E_g (eV)
$^{13}C \longrightarrow {}^{12}C$	14.6 [32]	5.4125 [32]
$^{7}LiH \longrightarrow {}^{7}LiD$	103 [33]	4.992 $\longrightarrow$ 5.095 [33]
$^{7}LiH \longrightarrow {}^{6}LiH$	12 [33]	4.980 [33]
$CsH \longrightarrow CsD$	60 [34]	4.440 [34]
$^{30}Si \longrightarrow {}^{28}Si$	2 [35]	3.652 [35]
$^{30}Si \longrightarrow {}^{28}Si$	2.09 [36]	1.166 [36]
$^{68}ZnO \rightarrow {}^{64}ZnO$	0.372 [37]	3.400 [37]
$Zn^{18}O \rightarrow Zn^{16}O$	3.533 [37]	3.400 [37]
$^{68}ZnO \rightarrow {}^{64}ZnO$	0.40 [38]	3.400 [37]
$Zn^{18}O \rightarrow Zn^{16}O$	3.20 [38]	3.400 [37]
$^{69}GaP \longrightarrow {}^{71}GaP$	0.19 [39]	2.400 [39]
$^{65}CuCl \rightarrow {}^{63}CuCl$	−0.076 [40]	3.220 [40]
$Cu^{37}Cl \rightarrow Cu^{35}Cl$	0.364 [41]	3.220 [41]
$Cd^{34}S \rightarrow Cd^{32}S$	0.370 [42]	2.580 [42]
$^{110}CdS \rightarrow {}^{116}CdS$	0.040 ÷ 0.068 [43]	2.580 [42]
$Cu_2^{18}O \rightarrow Cu_2^{16}O$	1.116 [44]	2.151 [44]
$^{71}GaAs \rightarrow {}^{69}GaAs$	0.39 [40]	1.53 [40]
$^{76}Ge \rightarrow {}^{72}Ge$	0.225 [42–47]	1.53 [42–47]
$^{76} \rightarrow {}^{73} \rightarrow {}^{70}Ge$	0.37 [46, 47]	0.74 [46, 47]

the *normal coordinates*, the Hamiltonian of our task will have the following relation (see, e.g. [26]):

$$H(Q, P) = \sum_{i,q} \left[-\frac{\hbar^2}{2} \frac{\partial^2}{\partial Q^2(\vec{q})} + \frac{1}{2}\omega_j^2 Q_j^2(\vec{q}) \right] \tag{1.9}$$

In this relation, the sum, where every addend means the Hamiltonian of linear harmonic oscillator with coordinate $Q_j(\vec{q})$, the frequency $\omega_j(\vec{q})$ and the mass equal a unit. If the Hamiltonian system consists of the sum, where every addend depends on the coordinate and conjugates its quasiimpuls, then according to quantum mechanics [48–50] the wave function of the system equals the product of wave functions of every appropriate addend and the energy is equal to the sum of assigned energies. Any separate term of the Hamiltonian (1.9) corresponds, as indicated above, with the *linear oscillator*

$$-\frac{\hbar^2}{2}\frac{\partial^2 \Psi}{\partial Q^2} + \frac{1}{2}\omega^2 Q^2 \Psi = \varepsilon \Psi. \tag{1.10}$$

Solving the last equation and finding the eigenvalues and eigenfunctions and then expressing explicitly the frequency, we will obtain for the model with two atoms in primitive cell (with masses M_1 and M_2; $M_1 > M_2$) the following equation:

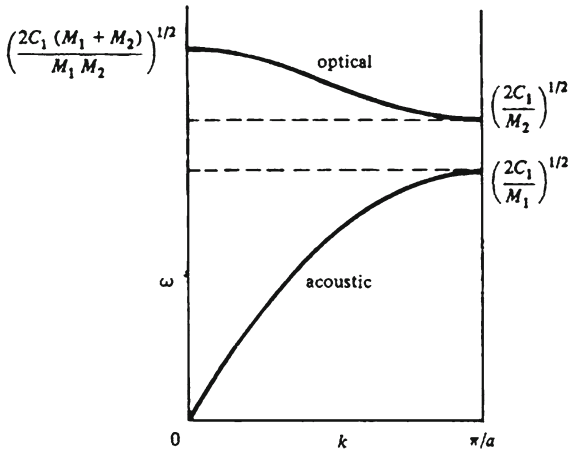

Fig. 1.2 Optical and acoustic modes. The optical modes lie at higher frequencies and show less dispersion than the acoustic modes (for details see text)

$$\omega^2 = \mathrm{C}\left(\frac{M_1+M_2}{M_1M_2}\right) \pm \left[\mathrm{C}^2\left(\frac{M_1+M_2}{M_1M_2}\right) - \frac{4C^2}{M_1M_2}\sin^2\frac{ka}{2}\right]$$

or

$$\omega_{\pm}^2 = \mathrm{A} \pm \left[\mathrm{A}^2 - \mathrm{B}\,\sin^2\frac{ka}{2}\right]^{1/2}. \tag{1.11}$$

There are now two solutions for ω^2, providing two distinctly separate groups of vibrational modes. The first group, associated with ω_-^2, contains the acoustic modes. The second group arises with ω_+^2 and contains the optical modes; these correspond to the movement of the different atom sorts in opposite directions (e.g. NaCl-structures), it is contra motion whereas the acoustic behavior is motion in unison.

For small ka we have from (1.11′) two roots:

$$\omega^2 \simeq 2\mathrm{C}\left(\frac{1}{M_1}+\frac{1}{M_2}\right)$$

and

$$\omega^2 \simeq \frac{\mathrm{C}}{2(M_1+M_2)}K^2a^2. \tag{1.12}$$

Taking into account that $K_{\max} = \pm\pi/a$, where a is a period of the crystal lattice, i.e., $K_{\max}$ respond to the border of the first *Brillouin zone* (see also Fig. 1.2)

$$\omega^2 = \frac{2\mathrm{C}}{M_1} \quad \text{and} \quad \omega^2 = \frac{2\mathrm{C}}{M_2} \tag{1.13}$$

As it is clear, formula (1.11′) describes the optical branch of vibrations whereas (1.12) the acoustical branch of vibrations. Usually the last formula is written as

follows:

$$\omega = \sqrt{\frac{\alpha}{M}}, \tag{1.14}$$

where α is the so-called force constant. Here, M is the mass of vibrated atom (ion). From the preceding relation it is clear that, as in molecular physics [21], in solids, the isotope effect directly manifests in vibration spectrum, which depends on the symmetry [30] measures either in IR—absorption or in *Raman scattering* of light. Before analyzing Raman scattering spectra of different solids we briefly consider the classical approximation of the mechanism of Raman effect [51–53].

Historically, Raman scattering denotes inelastic scattering of light by molecular vibrations or by optical phonons in solids. In a macroscopic picture, the Raman effect in crystals is explained in terms of the modulation of polarizability by the quasiparticle under consideration. The assumption that the polarization depends linearly upon the electric field strength [54] is a good approximation and is invariably used when discussing the scattering of light by crystal excited by lasers. However, the approximation is not valid for large strength such as can be obtained from pulsed lasers [55]. The polarization may then be expressed as

$$P = \alpha \mathrm{E} + \frac{1}{2}\beta \mathrm{E}^2 + \frac{1}{6}\gamma \mathrm{E}^3 + \frac{1}{24}\delta \mathrm{E}^4 + \ldots\ldots, \tag{1.15}$$

where β, the first hyperpolarizability coefficient, plays an important part for large values of E, since it is responsible for the phenomenon of optical harmonic generation using Q-switched lasers. Isolated atoms have $\beta = 0$, since, like μ the dipole moment, it arises from interactions between atoms. A simplified theory of Rayleigh scattering, the *Raman effect*, harmonic generation and hyper Raman scattering is obtained by setting (see, e.g. [55])

$$\mathrm{E} = \mathrm{E}_0 \cos \omega_0 \mathrm{t}, \tag{1.16}$$

$$\alpha = \alpha_0 + \left(\frac{\partial \alpha}{\partial Q}\right) Q, \tag{1.17}$$

$$\beta = \beta_0 + \left(\frac{\partial \beta}{\partial Q}\right) Q, \tag{1.18}$$

$$Q = Q_0 + \cos \omega_v \mathrm{t}. \tag{1.19}$$

Here, Q is a normal coordinate, ω_v is the corresponding vibrational frequency and ω_0 is the laser frequency. After that we have

$$\mathrm{P} = \alpha_0 \mathrm{E}_0 \cos\omega_v t + \frac{1}{2}\left(\frac{\partial\alpha}{\partial Q}\right) Q_0 \mathrm{E}_0 \cos\omega_0 \mathrm{t}\cos\omega_v t + \frac{1}{2}\beta_0 \mathrm{E}_0^2 \cos^2\omega_0 t + \frac{1}{2}\left(\frac{\partial\beta}{\partial Q}\right) \mathrm{Q}_0 \mathrm{E}_0^2 \cos^2\omega_0 \mathrm{t}\cos\omega_v t. \tag{1.20}$$

Then, after small algebra, we obtain

$$\mathrm{P} = \alpha_0 \mathrm{E}_0^2 \cos\omega_v t + \frac{1}{2}\left(\frac{\partial\alpha}{\partial Q}\right) Q_0 \mathrm{E}_0 \cos(\omega_0 - \omega_v)t + \cos(\omega_0 + \omega_v)t + \frac{1}{2}\beta_0 \mathrm{E}_0^2 + \frac{\beta_0}{4}\mathrm{E}_0^2 \cos\,2\omega_0 t + \frac{1}{2} Q_0 \mathrm{E}_0^2 \left(\frac{\partial\beta}{\partial \mathrm{Q}}\right) \cos(2\omega_0 - \omega_v)t + \cos(2\omega_0 - \omega_v)t. \tag{1.21}$$

In the last relation the first term describes the Rayleigh scattering, second—*Raman scattering*, third—d.c. polarization, fourth—frequency doubling and the last—hyper Raman effect. Thus the hyper Raman effect is observed with large electric field strength in the vicinity of twice the frequency of the exciting line with separations corresponding to the vibrational frequencies. α and β are actually tensors and β components $\beta_{\alpha\beta\gamma}$ which are symmetrical suffixes [30].

Semiconducting crystals (C, Si, Ge, $\alpha - \mathrm{Sn}$) with diamond-type structure present ideal objects for studying the isotope effect by the Raman light-scattering method. At present, this is facilitated by the availability of high-quality crystals grown from isotopically enriched materials (see, e.g [56] and references therein). In this part our understanding of first-order Raman light scattering spectra in isotopically mixed elementary and compound (CuCl, GaN, GaAs) semiconductors having a zinc blende structure is described. Isotope effect in light scattering spectra in Ge crystals was first investigated by Agekyan et al. [57]. A more detailed study of Raman light scattering spectra in isotopically mixed Ge crystals has been performed by Cardona and Thewalt [56].

It is known that materials having a diamond structure are characterized by the triply degenerate phonon states in the Γ point of the *Brillouin zone* ($\vec{k} = 0$). These phonons are active in the Raman scattering spectra, but not in the IR absorption one [51]. Figure 1.3a demonstrates the dependence of the shape and position of the first-order line of optical phonons in germanium crystal on the isotope composition at liquid nitrogen temperature (LNT) [58]. The coordinate of the center of the scattering line is proportional to the square root of the reduced mass of the unit cell, i.e., $\sqrt{M}$. It is precisely this dependence that is expected in the harmonic approximation. An additional frequency shift of the line is observed for the natural and enriched germanium specimens and is equal, as shown in Ref. [56] to 0.34 ± 0.04 and $1.06 \pm 0.04\,\mathrm{cm}^{-1}$, respectively (see, e.g. Fig. 4.7 in Chap. 4 of Ref. [59]).

First-order Raman light-scattering spectrum in diamond crystals also includes one line with maximum at $\omega_{\mathrm{LTO}}(\Gamma) = 1,332.5\,\mathrm{cm}^{-1}$. In Fig. 1.3b the first-order scattering spectrum in diamond crystals with different isotope concentrations is shown [60]. As shown below, the maximum and the width of the first-order scattering line in

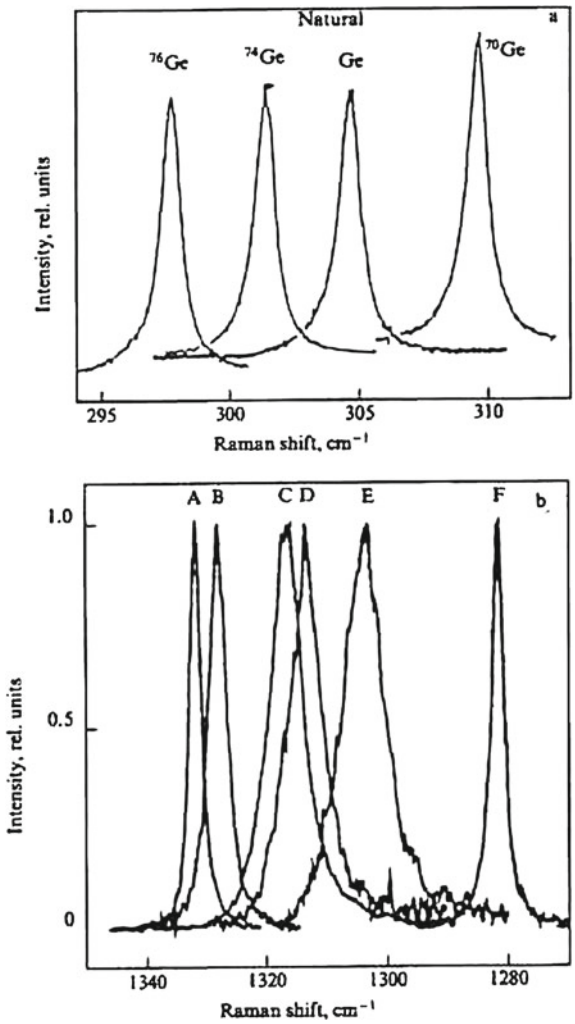

Fig. 1.3 **a** First-order Raman scattering spectra Ge with different isotope contents [56] and **b** First-order Raman scattering in isotopically mixed diamond crystals $^{12}C_x^{13}C_{1-x}$. The peaks A, B, C, D, E and F correspond to $x = 0.989$; 0.90; 0.60; 0.50; 0.30 and 0.001 (after [60])

isotopically mixed diamond crystals are nonlinearly dependent on the concentration of isotopes x. The maximum shift of this line is 52.3 cm^{-1}, corresponding to the two limiting values of $x = 0$ and $x = 1$. Analogous structures of first-order light scattering spectra and their dependence on isotope composition has by now been observed many times, not only in elementary Si and $\alpha - Sn$, but also in compound CuCl and GaN semiconductors (for more details see reviews [31, 56]). Already a shortlist of data shows a large dependence of the structure of first-order light-scattering spectra in diamond as compared to other crystals (Si, Ge). This is the subject of detailed discussion in [61].

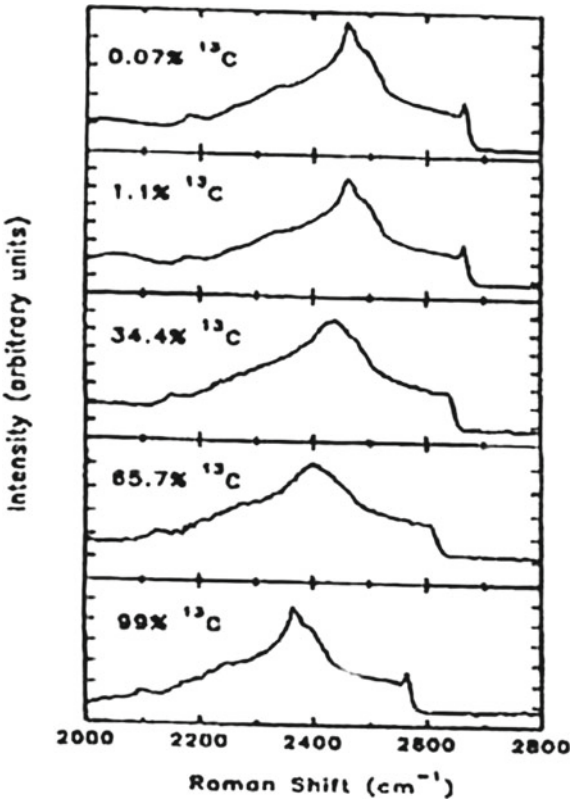

Fig. 1.4 Second-order Raman scattering spectra in synthetic diamond with different isotope concentration at room temperature (after [63])

Second-order Raman spectra in natural and isotopically mixed *diamonds* have been studied by Chrenko [62] and Hass et al. [63]. Second-order Raman spectra in a number of synthetic diamond crystals with different isotope compositions shown in Fig. 1.4 are measured wit resolution ($\sim 4\,\mathrm{cm}^{-1}$) worse than for first-order scattering spectra. The authors of the cited work explain this fact by the weak signal in the measurement of second-order Raman scattering spectra. It is appropriate to note that the results obtained in [63] for natural diamond ($C_{13_C} = 1.1\%$), agree well with the preceding comprehensive studies of Raman light-scattering spectra in natural diamond [64]. As is clearly seen from Fig. 1.4 the structure of second-order light scattering "follows" the concentration of the ^{13}C *isotope*. It is necessary to add that in the paper by Chrenko [64] one observes a distinct small narrow peak above the high-frequency edge of LO phonons and the concentration of ^{13}C x = 68%. Note in passing that second-order spectra in isotopically mixed diamond crystals were measured in the work by Chrenko [62] with a better resolution than the spectra shown in Fig. 1.4. Second-order Raman light scattering spectra and IR absorption spectra in crystals of natural and isotopically enriched ^{70}Ge can be found in [31].

A comprehensive interpretation of the whole structure of second-order Raman light-scattering spectra in pure LIH (LiD) crystals is given in [22, 61]. Leaving this question, let us now analyze the behavior of the highest frequency peak after the substitution of hydrogen for deuterium (see, also [65]).

Absorption behavior of an IR-active phonon in mixed crystals with a change in the concentrations of the components can be classified into two main types: one and two-mode (see, e.g. the review [66]). *Single-mode behavior* means that one always has a band in the spectrum with a maximum gradually drifting from one endpoint to another. *Two-mode behavior* is defined by the presence, in the spectrum, of two bands characteristic of each components leading not only to changes in the frequencies of their maxima, but mainly to a redistribution of their intensities. In principle, one and the same system can show different types of behavior at opposite ends [67]. The described classification is qualitative and is rarely realized in its pure form (see, also [67]). The most important necessary condition for the two-mode behavior of phonons (as well as of electrons [68]) is considered to be the appearance of the localized vibration in the localized defect limit. In the review [66] a simple qualitative criterion for determining the type of the IR *absorption behavior* in crystals with an NaCl structure type has been proposed (see also [68]). Since the square of the TO (Γ) phonon frequency is proportional to the reduced mass of the unit cell M, the shift caused by the defect is equal to

$$\Delta = \omega_{\mathrm{TO}}^2 \left(1 - \frac{\overline{\mathrm{M}}}{\overline{\mathrm{M}}'}\right). \tag{1.22}$$

This quantity is compared in [66] with the width of the optical band of phonons which, neglecting acoustical branches and using the parabolic dispersion approximation, is written as

$$W = \omega_{\mathrm{TO}}^2 \left(\frac{\varepsilon_0 - \varepsilon_\infty}{\varepsilon_0 + \varepsilon_\infty}\right). \tag{1.23}$$

A local or gap vibration appears, provided the condition $|\Delta| > (1/2)W$ is fulfilled. As mentioned, however, in [66] in order for the two peaks to exist up to concentrations of the order of $\sim$0.5, a stronger condition $|\Delta| > W$ has to met. Substituting the numerical values from Table 1.1 of [61] into formulas (1.22) and (1.23) shows that for LiH (LiD) there holds (since $\Delta = 0.44\,\omega_{\mathrm{TO}}^2$ and $W = 0.58\omega_{\mathrm{TO}}^2$) the following relation:

$$|\Delta| > (1/2)W. \tag{1.24}$$

Thereby, it follows that at small concentrations the local vibration should be observed. This conclusion is in perfect agreement with earlier described experimental data [65]. As to the second theoretical relation $\Delta > W$, one can see from the above discussion that for LiH (LiD) crystals the opposite relation, i.e., $W > \Delta$, is observed [20].

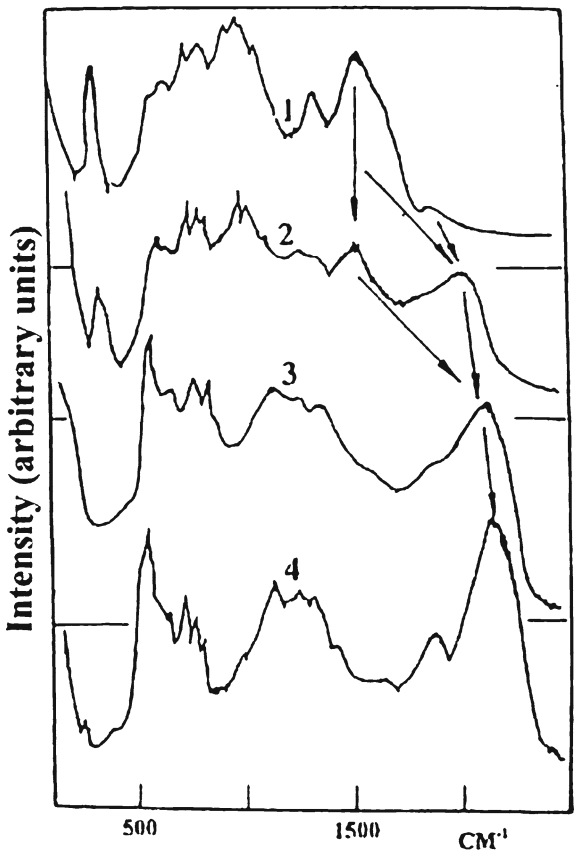

Fig. 1.5 Second-order Raman scattering spectra in the isotopically mixed crystals LiH_xD_{1-x} at room temperature. $1 - x = 0; 2 - 0.42; 3 - 0.76; 4 - 1$. The *arrows* point out a shift of LO(Γ) phonons in the mixed crystals (after [61])

Following the results of [69], in Fig. 1.5 we show the second-order Raman scattering spectra in mixed LiH_xD_{1-x} crystals at room temperature. In addition to what has been said on Raman scattering spectra at high concentration [69], we note that as the concentration grows further ($x > 0.15$) one observes in the spectra a decreasing intensity in the maximum of 2LO (Γ) phonons in LiD crystal with a simultaneous growth in intensity of the highest frequency peak in mixed LiH_xD_{1-x} crystals. The nature of the latter is in the renormalization of LO(Γ) vibrations in mixed crystal [70]. Comparison of the structure of Raman scattering spectra (curves 1 and 2 in Fig. 1.5) allows us, therefore, to conclude that in the concentration range of $0.1 < x < 0.45$ the Raman scattering spectra simultaneously contain peaks of the LO(Γ) phonon of pure LiD and the LO(Γ) phonon of the mixed $LiH_xD1 - x$ crystal. For further concentration growth ($x > 0.45$) one could mention two effects in the Raman scattering spectra of mixed crystals. The first is related to an essential reconstruction of the acoustooptical part of the spectrum. This straightforwardly follows from a comparison of the structure of curves 1–3 in Fig. 1.5. The second effect originates from a further shift of the highest frequency peak toward still higher frequencies, related to

the excitation of LO(Γ) phonons. The limit of this shift is the spectral location of the highest frequency peak in LiH. Finishing our description of the Raman scattering spectra, it is necessary to note that a resonance intensity growth of the highest frequency peak is observed at $x > 0.15$ in all mixed crystals (for more details see [72]).

One more reason for the discrepancy between theory and results of the experiment may be connected with not taking into account in theory the change of the *force-constant* at the *isotope substitution* of the smaller in size D by H ion [72]. We should stress once more that among the various possible isotope substitutions, by far the most important in vibrational spectroscopy is the substitution of hydrogen by deuterium. As is well known, in the limit of the Born-Oppenheimer approximation the force-constant calculated at the minimum of the total energy depends upon the electronic structure and not upon the mass of the atoms. It is usually assumed that the theoretical values of the phonon frequencies depend upon the force-constants determined at the minimum of the adiabatic potential energy surface. This leads to a theoretical ratio $\omega\,(\mathrm{H})\,/\omega\,(\mathrm{D})$ of the phonon frequencies that always exceed the experimental data. Very often anharmonicity has been proposed to be responsible for a lower value of this ratio. In isotope effect two different species of the same atom will have different vibrational frequencies only because of the difference in isotopic masses.

Chapter 2
Methods of the Preparation of Low-Dimensional Structures

2.1 Molecular Beam Epitaxy and Metal-Organic Chemical Vapor Deposition

During the 1980s two newer epitaxial techniques were introduced which are in widespread use today for the preparation of III–V (II–VI) semiconductor multilayers for both physics studies and device fabrication. These techniques are molecular beam epitaxy (MBE) and metal-organic chemical vapor deposition (MOCVD) [5–7, 73, 74]. With this it is possible to control both the chemical composition and the level of doping down to thickness that approaches an atomic monolayer, and certainly within less than one nanometer (10^{-9} m). MBE and MOVCVD thus approach the absolute limits of control for preparing layered semiconductor structures [5, 6].

Fabrication of a crystal layer upon wafer of a compatible crystal makes it possible to obtain very well-controlled growth regimes and to produce high-quality crystals with the desired crystalline orientation at temperatures typically well below the melting point of the substrate. The schematic heart of the MBE process is shown in Fig. 2.1, while the photograph of such equipment can be found in [75]. MBE is a conceptually simple crystal growth technique. An MBE machine consists of a stainless steel vessel of diameter approximately 1 m (Fig. 2.1) which is kept under ultrahigh vacuum (10^{-11} Torr) by a series of pumps [75]. Recent comprehensive reviews and monographs [5, 6, 73, 74] give an up-to-date description of the technique and its application to the growth of semiconductor layers for electronic devices. On one side (see Fig. 2.1) a number of cells (typically eight) are bolted onto the chamber. These Knudsen cells are of some complexity, again to control the processes for which they are responsible. Inside each a refractory material boat contains a charge of one of the elemental species (for example, Ga, Al or As) for growth of the semiconductor, Si (for n-type doping), and Be or B (for p-type doping). Each boat is heated so that a vapor is obtained which leaves the cell for the growth chamber through a small orifice. The vapor is accelerated by the pressure differential at the orifice and forms a beam that crosses the vacuum chamber to impinge on a GaAs substrate which is mounted on a holder controlled from the opposite site of the chamber. The substrate

V. G. Plekhanov, *Isotope Low-Dimensional Structures*, SpringerBriefs in Physics,
DOI: 10.1007/978-3-642-28613-1_2,

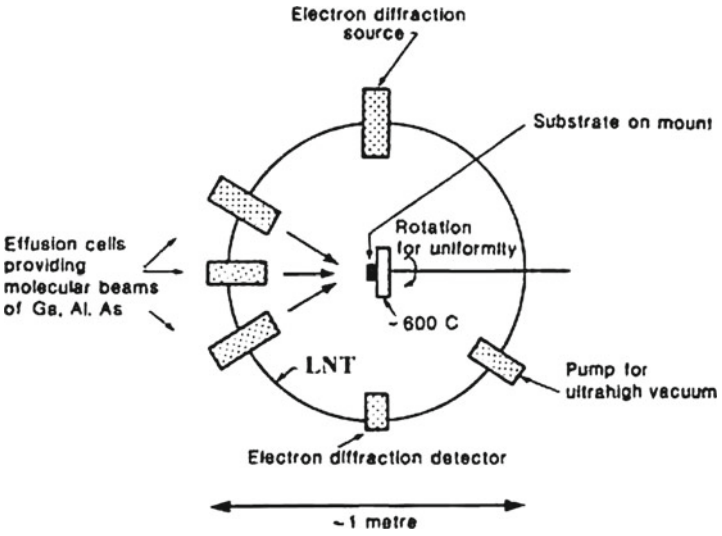

Fig. 2.1 The MBE method for the growth of hetero-structures

holder contains a heater, as the quality of the grown crystal is a sensitive function of the substrate temperature (about 580 and 630°C is best for GaAs and AlAs [5, 6]). The flux rate is controlled by the temperature within the Knudsen cell. The control and monitoring of the fluxes from the different cells ensure approximately that a monolayer's worth of molecular beam species impinge on the substrate in 1 s. Thus the growth rates of the layers are typically 10^{-6} mh^{-1}. Shutters in front of the orifices can be opened and closed in less than 0.1 s [74] and so combinations of Ga to Al flux can be varied to produce the species for growing $Al_xGa_{1-x}As$ alloys. The opening and closing of different shutters determines the multilayer structure that is grown in terms of both semiconductor composition and doping profile (see also [2, 76]).

The advantages of MBE are:

1. The use of only high-purity elemental sources rather than less pure compounds may ultimately result in the highest purity.
2. Growth occurs in UHV apparatus where background concentrations of undesirable gases such as H_2O, CO, and O_2 are very low.
3. In situ analytical tools (e.g. high-energy electron diffraction (RHEED), see Fig. 2.1) may be used to monitor the crystal structure and composition.
4. Extreme control of growth rate and composition leads to very abrupt ($\langle 20$ Å) changes in composition and/or doping level.
5. Pattern growth is possible through masks, by focused ion beams and on areas defined by electron beam writing.

BN is found to be an excellent crucible (boat) material for growth of high-purity III–V compounds [73]. A lower limit of the atomic or molecular flux from an diffusion cell (see e.g. [6, 74])

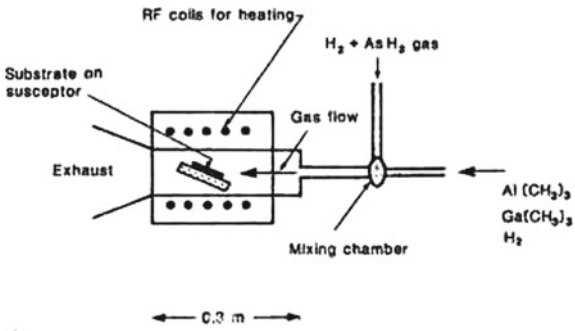

Fig. 2.2 A scheme of the growth cell of an MOCVD method

$$J = 1.11 \times 10^{22}[AP(T)]/d^2(mT)^{1/2}, \tag{2.1}$$

where the flux J is expressed in molecules $\mathrm{cm}^{-2}\,\mathrm{s}^{-1}$, A is the area of the opening, $P(T)$ is the equilibrium pressure at the cell temperature, d is the distance to the substrate, and m is the mass of the diffusing molecule. For typical systems, $A \sim 1\,\mathrm{cm}^2$, $d \cong 10\,\mathrm{cm}$ and P(T) ranges from 10^{-2} to 10^{-3} Torr. These values give a flux at the substrate of $10^{15} - 10^{16}$ molecules $\mathrm{cm}^{-2}\mathrm{s}^{-1}$ and a growth rate of 1–10 monolayers per second, the typical growth rate in MBE systems (for details see [5, 73–75]).

Today, most of the III–V binary, ternary, and a few quaternary semiconducting alloys have been grown by the MOCVD technique. GaAs and $Al_xGa_{1-x}As$ have been the most fully researched. MOCVD, which is also known as organometallic chemical vapor deposition (OMCVD), takes place in a glass reactor (the photograph see in [75]), typically about 0.3 m long and about 0.1 m in diameter (see Fig. 2.2). In that reactor is a heated substrate site at an angle to a laminar flow of gas. Radiofrequency (rf) inductive heating is used to achieve substrate temperature comparable to those for MBE growth, although research is aimed at being able to use even lower substrate temperatures while maintaining high-quality growth.

In the case of growth of Si layers, several different gases containing Si atoms can be used. They include silicon tetrachloride ($SiCl_4$), silane (SiH_4), and dichlorosilane (SiH_2Cl_2). In the case of silicon tetrachloride, the following reaction with hydrogen occurs:

$$SiCl_4 + 2H_2 \longrightarrow Si + 4HCl. \tag{2.2}$$

The reaction can be conducted at temperatures in the range of 1,150–1,250°C (see, e.g. [6]). In the case of using silane and dichlorosilane, the reaction can be conducted at even lower temperatures (1,000–1,100°C). These temperatures are well below the melting point of Si (T_m =1,412°C [73]). Thus, these reactions release atoms of Si, and the relatively low-temperature regimes provide efficient crystal growth onto the seed.

For growth of III–V compounds, the following reactions are used

$$\begin{aligned} A_{III}(CH_3)_3 + B_V H_3 &\longrightarrow A_{III}B_V, \\ A_{III}(CH_3)_3 + B_V H_3 &\longrightarrow A_{III}B_V + 3CH_4. \end{aligned} \tag{2.3}$$

Here, A_{III} is B, Al, Ga, IN, Tl and B_V is N, P, AS, Sb, Bi. These reactions take place at temperatures of ≈600–700°C [6]. Dopants zinc [$Zn(CH_3)_2$] or silane are used to provide the dopant species. It is important that epitaxial methods can be applied to produce new materials that are difficult to grow by other methods. Examples are wide-bandgap nitrides of the group III elements. These include INGaN and AlGaN compounds.

In conclusion, both group IV elements (C, Si, Ge, Sn, Pb) and III–V compounds are successfully grown with thickness control of the order of one monolayer. Different types of doping-uniform doping, modulation doping, and delta-doping are realized with high accuracy [3, 4]. Since in the chemical reactor the partial pressures of chemicals are much higher than the pressure in the molecular beams of the MBE method, the rate of crystal growth realized in the MOCVD method is higher than that of MBE. The former may be used in industrial production, while the latter is rather well suited for research laboratories.

The principles behind both MBE and MOCVD growth were established in the 1970s and refined in the 1980s, since which time further developments have taken place. New methods of growth research whose benefits will be realized during the last two decades can be found in references [5, 6, 73, 74].

2.2 Nanolitography and Etching Technologies

This paragraph describes the *nanolitography* and etching technologies used in fabrication of *semiconductor nanostructures* for physics and device studies. These state-of-the-art fabrication techniques are available precisely because they are foreseen as essential in one or other strategies for the fabrication of future devices (see, also [2, 3, 7]). As shown above, MBE and MOCVD grow high-quality single-crystal wafers and crystalline multilayered structures thicknesses may be on the nanometer scale. However, to produce an individual device or electric circuit scaled down to nanosize in two or three dimensions, one needs to exploit the so-called nanolitography. For these processes, whereby short-wave radiation, for example short-wave ultraviolet (UV), electron beams, X-radiation, and ion beams are used to produce finer structures. Figure 2.3 presents a rough overview of the different nanolitography methods. At first, it is possible to create ever finer structures by using higher-energy radiation. But it must be noted that the material defects also increase proportionally [16]. It is clear that one practical limit to the smallest feature sizes that can be faithfully be reproduced is the wavelength of that light, i.e., the diffraction limit with visible light, in the range 400–800 nm. According Grenville et al. [77] the optical litography

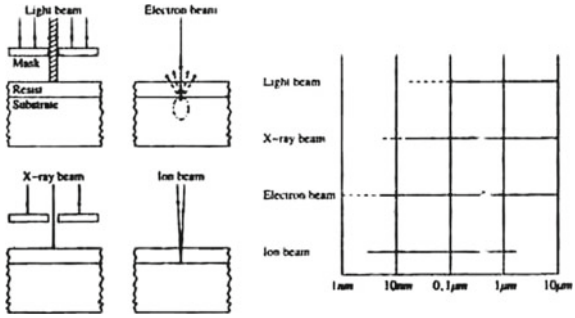

Fig. 2.3 Overview of different litography method

using visible light is available down to 0.15×10^{-6} m feature sizes in lithography for integrated circuits (see, also [1, 2]).

Electron-beam direct writing is a usual method to produce fine structures. The major disadvantage of this approach is that all individual structures must be written one after the other, which consumes a lot of time. That is why electron-beam writing is only economical for the mask production and not for direct structuring tasks on wafers. The X-ray lithography is very promising, although no usable lens systems and reflectors for wavelengths between 0.5 and 5 nm are known. The imaging has to be performed by so-called contact copies with special masks. The mask carrier is a thin silicon film ($\sim 2 \times 10^{-6}$ m), which is transparent for X-radiation. The actual masking part is a thin gold layer (10^{-6} m) structured by electron-beam writing. In order to avoid contact copy image defects on the semiconductor wafer, the X-ray beams should run as parallel as possible. When using a normal X-ray tube, the distance between the radiation source and the silicon wafer is so small that many image defects occur in the peripherical wafer area. This error ΔB can be simply measured by the following rule (see, e.g. [74]):

$$\Delta B = t\frac{B}{S}, \tag{2.4}$$

where t represents the mask-wafer distance, B equals the wafer radius, and S is the distance to the radiation source. To keep this deviation small, the distance S has to be increased as much as possible, which can be achieved by extracting X-ray beams from a synchrotron. When using such a synchrotron, the distance S can be chosen to be relatively large, say 10 m, so that the error ΔB is reduced to less than ± 10 nm.

The comparison between the different lithography methods, the highest throughput is still achieved by *optical lithography* [2, 14]. A higher resolution can be attained by using X-ray or electron beams. The single probe methods, whereby single atoms are manipulated, yields the best results. Remarkable results are also produced by a structure printing process, the so-called nanoprinting (see, also [1]). Another method should be mentioned in this context: the scanning tunneling microscope (STM) can be utilized to visualize and analyze the fine structure (for details see next paragraph).

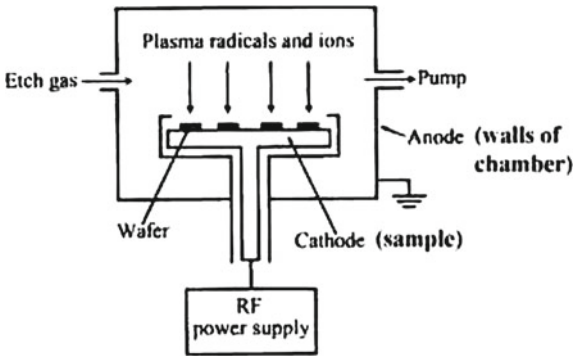

Fig. 2.4 Scheme of plasma etching

There are two principal forms of etching—using wet chemicals or using (dry) plasmas. Each method has advantages and disadvantages. Wet chemistry has been used since the earliest days of integrated circuit manufacture. The range of dilute acid and alkaline materials used is quite wide. For example HF reacts with SiO_2 and does not affect the photoresist or silicon. That is, this wet chemical etch is highly selective. However, the rate of etching is the same for any direction, lateral or vertical, so the etching is isotropic (see, however [1]). Using an isotropic etching technique is acceptable only for relatively large structures. For nanosize structures, anisotropic etching with faster vertical etching is preferable.

Anisotropic etching generally exploits a physical process, or some combination of both physical and chemical methods. The best-known method of anisotropic etching is reactive-ion etching. Reactive-ion etching is based on the use of plasma reactions. This method works as follows. An appropriate etching gas, for example a chlorofluorocarbon, fills the chamber with the wafers. The pressure is typically reduced, so that an rf voltage can produce a plasma. The wafer to etch is a cathode of this rf dicharge, while the walls of the chamber are grounded and act as an anode. Figure 2.4 illustrates a principal scheme for the ion-etching method. The electric voltage heats the light electrons and they ionize gaseous molecules, creating positive ions and molecular fragments (chemical radicals). Being accelerated in the electric field, the ions bombard the wafer normal to the surface. This normal incidence of bombarding ions contributes to the etching and makes the etching highly anisotropic. This process, unfortunately, is not selective. However, the chemical radicals present in the chamber give rise to chemical etching, which, as we pointed above, is selective. From this, we can conclude that the method combines both isotropic and anisotropic components and can give good results for etching on the nanoscale (see e.g. Fig. 3.4 in [1]). For further details on etching techniques see [78–80]).

2.3 Techniques for Characterization of Nanostructures

Progress in the fabrication, study, and use of *nanostructures* would not be possible without adequate techniques for the characterization of these structures. These techniques should allow one to determine the shape and geometrical parameters of nanostructures, the distribution of chemical composition, the strain fields, etc. Knowing all of these one can predict the electronic and optical properties which will ultimately be relevant in applications. In this paragraph we briefly describe the next techniques:

1. Hall measurements;
2. Secondary ion mass spectrometry (SIMS);
3. Methods for optical characterization;
4. Scanning tunneling microscopy (STM);
5. Atomic-force microscopy (AFM);
6. Transmission electron microscopy (TEM);

1. The simplest method for checking of doping levels (electrical characterization) in bulk semiconductors is the Hall measurements [24, 26].
2. This method involves removing material from a multilayer structure using a beam of high-energy ions (i.e., sputtering) and a mass analysis of the species from flat center of the crater (for details see [16, 81]).
3. Photoluminescence (PL), electroluminescence, and photoreflectance spectroscopy have all proved useful in the qualification of certain multilayer structures [7, 83]. As is well known, the first two techniques involve the examination of the wavelength- or energy-selected emission of light from a structure when the structure has first been excited by light or an electron beam respectively. The latter technique involves changes of reflectivity at different energies as small electric fields are applied to the solid. All three provide information about optical transitions and we shall see the way in which thin layers have optical transitions modified by quantum-size effects including the shape of heterojunction interfaces (atomically abrupt changes of comparison, or changes over two or more atomic layers, with or without lateral steps in the interface plane).

   The structure in the PL spectra as a function of energy can be used to infer the position of various energy levels—in particular the bandgap of the different layers—while the linewidths of the PL features can be interpreted in terms of uniformity and absence of fluctuation. PL as a diagnostic technique has a number of advantages: it is nondestructive, fairly simple to implement, able to give a rapid turnaround of information to crystal growers, and capable of use in a wafer-mapping mode (i.e., checking out the uniformity of layers in a manufacturing environment). The disadvantages include complications that arise if one has (as is often the case) an active device structure with heavily doped contact layers on either side; such doped layers tend to reabsorb and redistribute the luminescent energy. The qualitative results produced are particularly useful for many structures of optical devices (lasers etc.). Changes to the PL spectra under the

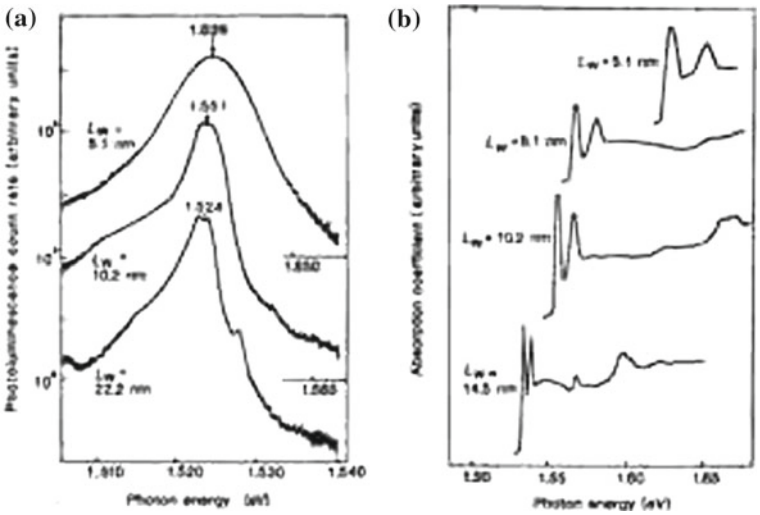

Fig. 2.5 **a** Photoplumenescence spectra for wells of different thickness W_L. **b** The photoluminescence excitation spectra from GaAs quantum wells (after [16])

influence of temperature changes, applied stress, magnetic fields, etc. all provide further insight into the thicknesses, compositions, and uniformity of multilayers. Photoluminescence excitation (PLE) spectroscopy involves the detection of light at a fixed energy (generally near a prominent band-edge feature, e.g. the lowest bandgap) while the excitation energy is monochromatic and is swept in energy. The amplitudes of features in the PLE spectra provide further information about the cross-section of the optical absorption processes involved in the relaxation of the excited electrons (excitons [82]). Typical PL and PLE data for a range of thin layers of GaAs between thicker AlGaAs layers, according to [16], is shown in Fig. 2.5.

4. STM yields surface topographies and work-function profiles on an atomic scale directly in real space. In terms of classical physics, a transfer process of an electron from one solid into another can be thought of as an electron transfer over a vacuum barrier. This process requires additional energy and because of this it has a small probability. On the other hand, according to quantum mechanics, a particle can penetrate a classically forbidden spatial region under a potential barrier. Thus, electron transfer between two solids can occur as a tunneling process through (under) vacuum barrier. The principle of STM, which is based on electron tunneling, is straightforward. It consists essentially of a scanning metal tip (one electrode of the tunnel junction) over the surface to be investigated—the second electrode. At present, the resolution of STM reaches 0.5 Å vertically and well below 2 Å laterally (see, e.g. [10]). On the other hand, STM is subject to some restrictions in application: only conductive samples can be investigated, and measurements usually have to be performed in UH vacuum. At the same

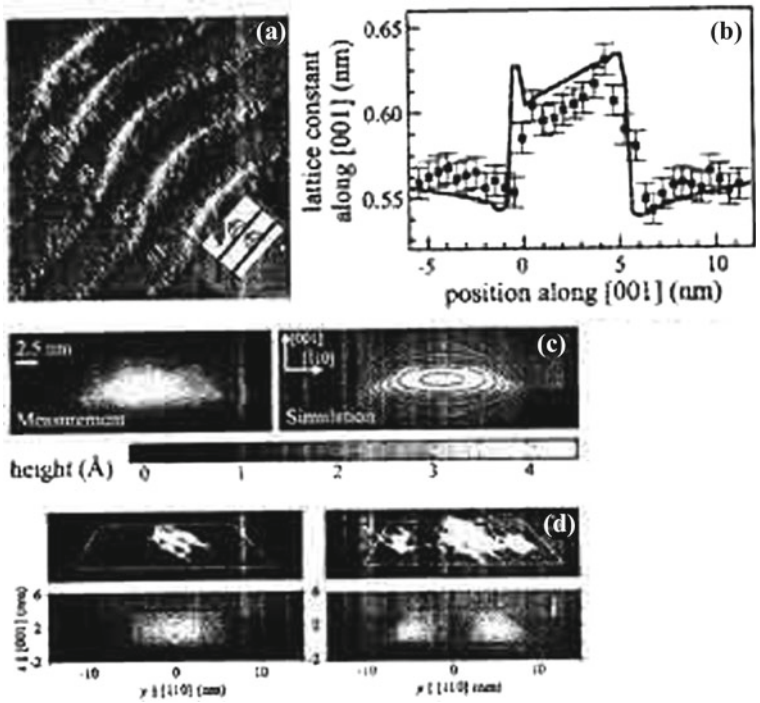

Fig. 2.6 Cross-sectional STM. **a** An image of a stack of InAs islands in GaAs. **b** The lattice parameter in the growth direction in an InAs island (the experimental data were obtained from cross-sectional STM; the solid line is from a simulation assuming an In content increasing from island base to island apex). **c** Comparison between measured and simulated height profiles for a similar sample. **d** The electronic wavefunction measured at two different tip biases, compared with simulation for the ground and the first excited states (after [9])

time, the tunnel current is sensitive to material composition and strain. Atomic resolution in both lateral and vertical directions makes STM an ideal tool for the investigation of growing surfaces at this scale, which can give insight into growth mechanisms. STM systems attached to a growth chamber allow measurements to be made without breaking the vacuum after growth [76]. It is remarkable that, apart from providing structural information, low-temperature STM has been used for wavefunction mapping of single electron states in nanostructures. Applied to the InAs dots (islands) the STM methods directly reveal s-, p-d-, and even f-type states as made visible by an asymmetry of the electronic structure (see Fig. 2.6), which can be attributed to a shape symmetry of the islands (see also [9, 83]).

5. An atomic force microscope (AFM) measures the force between the sample surface and a very fine tip. The force is measured either by recording the bending of a cantilever on which the tip is mounted—in contact mode—or by measuring the change in resonance frequency due to the force—the trapping mode. With a

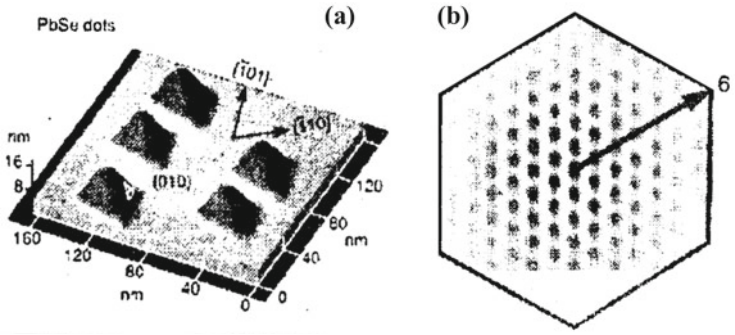

Fig. 2.7 PbSe islands with {001} facets. **a** AFM image of the top surface of a PbSe/PbEuTe island multilayer grown on BaF_2. **b** The autocarrelation function. Islands are arranged in a regular array up to the sixth-nearest neighbor (after [9])

typical resolution of several nanometers laterally and several Å vertically, AFM is ideally suited to characterize the shapes of nanostructures. With AFM, any surface can be investigated. Furthermore, most semiconductor materials oxidize under ambient conditions, so that, strictly speaking, the AFM images usually show the surface of this oxide. When obtaining quantitative data such as lateral sizes and heights of structures, this has to be kept in mind, as well as the fact that this image is actually a convolution of the sample's surface morphology with the shape of the microscope tip. Examples of the quantitative analysis of AFM images are shown in Fig. 2.7 [9]. There, the top surface of PbSe/PbEuTe multilayers is shown. From Fig. 2.7a, one can see that PbSe forms triangular pyramids with [001]-type side facets. The lateral ordering can also be analyzed. In Fig. 2.7b, a hexagonal in-plane arrangement of pyramids is evident (for details see [8, 9]).

6. Among the methods which allow one "to see" things at the nanometer scale, two types of electron microscopy play an important role. Transmission electron microscope (TEM) makes possible the visualization of thin slices of material with nanometer resolution [10]. This technique has subnanometer resolution, and, in principle, can resolve the electron densities of individual atoms (see, also [1, 74]). A TEM operates much like an optical microscope, but uses electrons instead of visible light, since the wavelength of electrons is much smaller than that of visible light. As we have already discussed, the resolution limitation of any microscope is based on the wavelength of the probe radiation. Since electrons are used instead of light, glass lenses are no longer suitable. Instead, a TEM uses magnetic lenses to deflect electrons. In a TEM, the electrons are collimated from the source and passed through the sample, and the resulting pattern of electron transmission and absorption is magnified onto a viewing screen. In scanning electron microscope (SEM), the electron beam is not projected through the whole sample area. Instead, it is raster-scanned across the surface, and the secondary electrons, or X-rays, emitted from the surface are recorded. This generates a low-

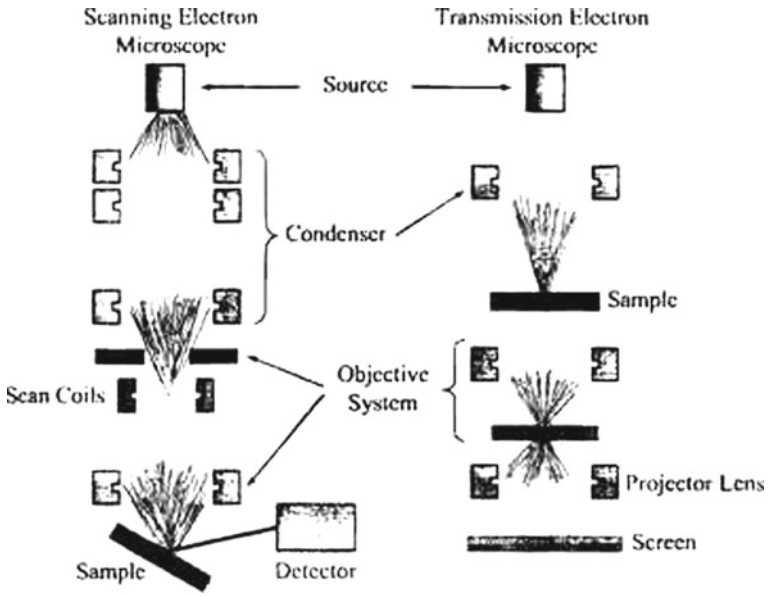

Fig. 2.8 Schematic diagrams of SEM and TEM

resolution image, but allows the direct mapping of surface features, and can even be used for elemental analysis. The scheme the both types of electron microscope are depicted in Fig. 2.8. Thus, the structural and chemical information provided by TEM (SEM) has made it the single most important analytical tool available (for details see [84, 85]).

One example of atomically resolved TEM, from which the position of unit cells, strain, and composition information were derived, is depicted in Fig. 2.9. Remarkably, these techniques make it possible to visualize a detailed map of the strain for an object of size a few tens of nanometers. From Fig. 2.9 it is seen clearly how the strain increases at the apex of the InGaAs island, while around the island the strain changes its sign.

Concluding this paragraph, we should note that powerful characterization techniques have been developed to study *nanosize* objects. The techniques give 3D images in real space and on atomic scale in all three dimensions. The methods are nondestructive (excluding TEM). They provide the means to perform structural and chemical analysis of materials used in *nanostructures*. Moreover, these techniques make it possible to observe and measure directly the electron distribution inside the nanostructures; that is, it is possible to observe the electron probability density (for details see [8–10, 86–88]).

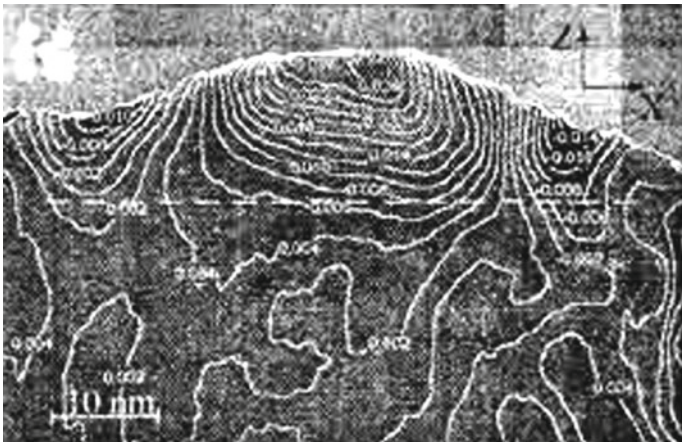

Fig. 2.9 Strain distribution obtained from the TEM images of InGaAS islands in GaAs by using the method of digital analysis of lattice images (after [9])

2.4 Nuclear Technology

The advances in epitaxial thin film homo and heterostructures. synthesis, which have been achieved through a variety of epitaxial techniques [5, 6], have led to a vast array of new solid-state structures with many fascinating properties (see, e.g. [1–4]). In view of this vast variety of activities and discoveries of *isotope* heterostructures, including isotope heterostructures, has been studied only in the last two decades [89–97]. In combination with the well-established neutron transmutation doping (NTD [12]) technique, isotope heterostructures appear to represent a family of solid-state structures, which offer new possibilities and numerous advantages over the traditional multilayer structures (see above). The formation of a doped isotope multilayer structure can be broken down into two independent steps: growth of the structure with isotopically pure or deliberately mixed layers and selective doping with the NTD process (see, also [96]). The formation of an isotope multilayer structure differs from the traditional methods only in sofar that isotopically pure and deliberately mixed sources must be used, and, most importantly, that no dopants are introduced during the growth process. Especially, it is very prospective for isotope-induced band gap opening in graphene (will be published). The absence of any dopants during the growth process automatically eliminates all dopant-induced effects including autodoping and dopant interdiffusion between adjacent layers [93]. In principle, all the established epitaxial techniques can be applied to the growth of isotope multilayer structures. The only requirement is the availability of semiconductor grade pure isotopes. The doping of isotope heterostructures is achieved with the NTD [12] techniques after the growth process has been completed. The NTD technique is isotope selective and therefore it can be used superlatively for the creation of the low-dimensional structure. The cross-section for thermal neutron capture and the

subsequent nuclear processes of practically every stable isotope of all elements have been measured, studied, and documented (see also [12] and references therein).

As we all know that breaking the crystal translational symmetry without strongly influencing its electronic band structure can be done by means of a modification in the mass of one or more atoms composing the crystal, without translational symmetry, the wave vector conservation requirements can be circumvented. Ideal models for most studies of elementary excitations are represented by isotopically pure crystals. A new field offering interesting physical studies is opened with the growth of isotopically tailor-made single crystals. The translational symmetry operations can be removed in part by artificial fabricating isotopic superlattice in which layers of two isotopically enriched materials alternate periodically. MBE of isotopically controlled germanium has enabled studies of low-dimensional phonons in isotope superlattice [91–94] and quantum dots [95].

In the remainder of this paragraph we describe the results of Raman measurements on novel kinds of heterostructures, a series of isotopic superlattices of germanium and silicon [92–96]. These samples represent an excellent model system to study the vibrionic properties of superlattices because the electronic structure should be affected only weakly by changes in the isotopic mass (see, e.g. [31, 56]).

Since these changes are the only difference between the superlattices constituents, Raman spectroscopy is the only nondestructive method to investigate their structural properties. Experimental data are compared with the results of planar force-constant model [91]. Let us consider the case of Ge, with its five isotopes (see also [65]). The readers will ask themselves if one should see five phonons (or more if they know that there are two atoms per primitive cell), corresponding to the five different masses, or only one corresponding to the average mass. We all know that the latter is true. The transition from the average mass vibrations to those localized at all possible pairs is an example of the Anderson localization phenomenon [98], which is observed in Raman experiments on LiH_xD_{1-x} system (for details see [61]). In a 3D crystal fluctuations in the parameters of the secular equation lead to localization (measured in units of frequency, i.e., $(\Delta M/M)\omega_0$) are larger than the bandwidth of the corresponding excitations [65, 66]. For optical phonons in Ge this bandwidth is $100\,cm^{-1}$ while $(\Delta M/M)\omega_0 \leqslant 0.04 \times 300 = 12\,cm^{-1}$ (see e.g. [98, 99]). Hence, no phonon localization (with lines corresponding to all pairs of masses) is expected, in agreement with the observation of only one line at $304\,cm^{-1}$ (at 77 K) for natural Ge (see Fig. 31 in [65]). For comparison we indicate that the bandwidth in the LiH_xD_{1-x} mixed crystal is more than $500\,cm^{-1}$, therefore the crystal and localized phonons are in coexistence (for details see [61]).

In *superlattice* composed, for example, of n layers of ^{70}Ge and m layers of ^{76}Ge repeated periodically, one would expect to find optical modes localized or nearly localized in each of two constituents. Schematics of Si isotope superlattice are depicted in Fig. 2.10. Koijma et al. [96] have grown three kinds of silicon isotope superlattices ($^{28}Si_n/^{30}Si_n$, with $n = 8$, 12 and 24) using the solid-source MBE technique. In this paper n denotes the thickness of each isotope layer in atomic monolayers, each 0.136 nm thick. The periodicity, i.e., the number of $^{28}Si/^{30}Si$ pair layers stacked vertically, are 80, 50 and 30 for $n = 8$, 12, and 24 samples

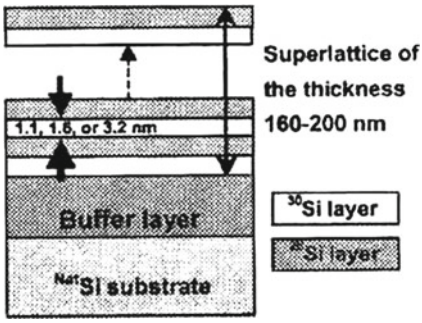

Fig. 2.10 Schematics of Si isotope superlattices. Thickness of each isotope layer are 1.1; 1.6; and 3.2 for $^{28}Si_8/^{30}Si_8$; $^{28}Si_{12}/^{30}Si_{12}$ and $^{28}Si_{24}/^{30}Si_{24}$ samples, respectively. Low index denotes the thickness of each isotope layer in atomic monolayers, each 0.136 nm thick (after [96])

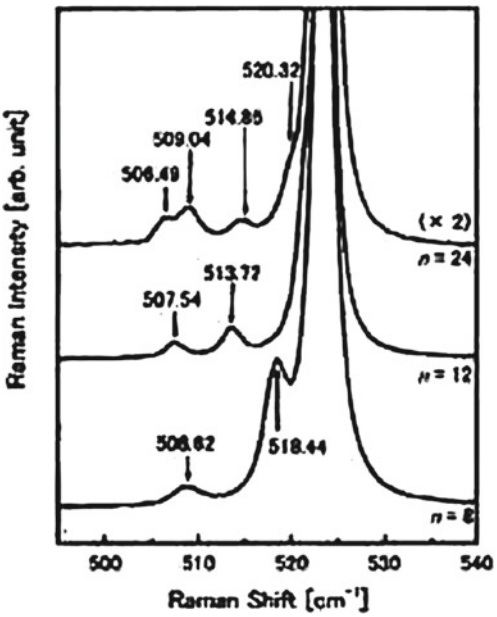

Fig. 2.11 Raman spectra of the $^{28}Si_n/^{30}Si_n$ samples with $n = 8$, 12 and 24 (after [96])

respectively. The resulting total thickness of the superlattice are 160–200 nm (see Fig. 2.10). The source for the ^{28}Si layer is actually ^{nat}Si which is composed of 92.2% ^{28}Si. The source for the ^{30}Si layer is a single Si crystal isotopically enriched to ^{30}Si($\sim$98.74% [97]). In MBE in individual effusion cells equipped with crucibles made of high purity tantalum. The crucible temperature is maintained at 1, 400°C for a growth rate of $\sim$0.01 nm/s. The base pressure of the vacuum is 5×10^{-10} torr and the pressure during growth is $\sim 10^{-9}$ Torr.

As shown above, the E versus k dispersion of phonons in the superlattice is zone-folded due to the new periodicity, na, introduced by the $(^{28}Si)_n - (^{30}Si)_n$ unit where a is the periodicity of the bulk Si. Because Raman spectroscopy, to first order, probes phonons situated at $k \sim 0$ in the dispersion relation, while only one longitudinal optical (LO) phonon peak is observed with bulk Si, multiple LO phonon peaks should appear for isotope superlattice due to the zone folding or phonon localization (see, e.g.

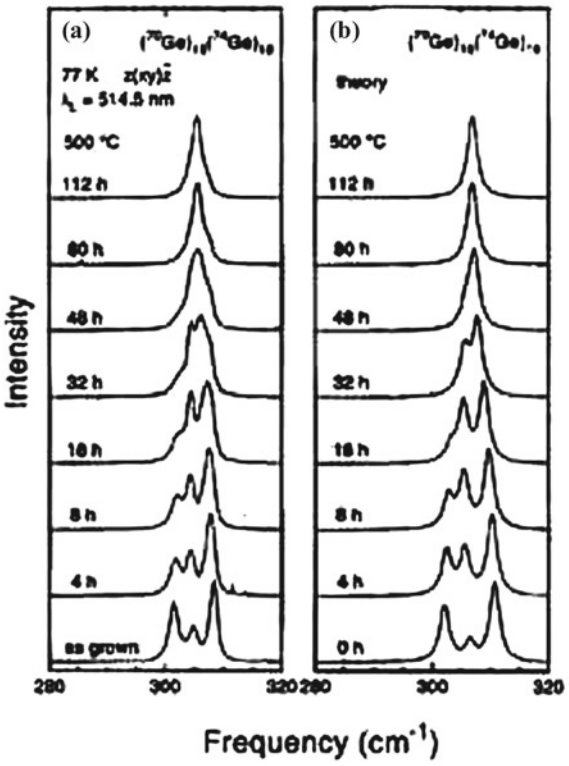

Fig. 2.12 **a** Experimental Raman spectra of a $(^{70}Ge)_{16}(^{74}Ge)_{16}$ superlattice for different annealing steps at 500°C. **b** Calculated Raman spectra for the same superlattice using the same parameters (after [93])

[101]). Figure 2.11 shows the Raman spectra of Si superlattice. As expected, many peaks are observed on the shoulders of the large ^{nat}Si substrate LO peak around 523.5 cm^{-1}. The wavenumbers of the identified peaks are indicated in Fig. 2.11 for comparison with theoretical predictions fulfilled in the planar bond-charge model for Si (see [99]). As was shown in [97] theoretical curves are not smooth due to anticrossings. In general, the agreement between the experimental and theoretical results is excellent, except for the one detail while $LO_1(^{28}Si)$ peaks in $n = 12$ and 24 samples are hidden in the large substrate peak, the $LO_1(^{28}Si)$ peak is observed experimentally for the $n = 8$ sample and its position deviates from the calculation (for details see Fig. 4 in [96]).

Raman spectra of a series of isotopic $^{70}(Ge)_n^{74}(Ge)_n$ *superlattice* with $2 \leq n \leq 32$ ($8 \leq n \leq 24$) was published in [92, 93]. Three modes could be observed (see Fig. 2.12) for the $^{70}(Ge)_{16}^{74}(Ge)_8$ "as-grown" superlattice as theoretically predicted [98]. We should underline the excellent agreement between results of papers [92, 93].

In conclusion we emphasize that isotopic superlattices represent an excellent model system for the investigation of confinement of optical phonons. Both frequencies and relative intensities of the measured spectra are in good agreement with calculations based on a planar bond–charge model and the bond–polarizability approach.

Chapter 3
Electron Excitations in Low-Dimensional Structures

3.1 Wave-Like Properties of Electrons

In classical physics we deal with two kinds of entities: particles, such as a small mass which obeys Newtoniat's equations, and waves as for example, electromagnetic waves which behave according to Maxwell's equations. Moreover, classical physical models assume the continuity of quantities and involve no restrictions concerning very small physical structures. The quantum theory shows, however, that values of some measurable variables of a system, can attain only certain discrete meanings. Therefore, in dealing with very small objects, like atoms, the above classification (particles and waves) is not enough to describe their behavior, and we have to turn to quantum mechanics, and to the dual concept of wave-particles. For instance, if light interacts with a material, it is better to think of it as being constituted by particles called photons instead of waves. On the other hand, electrons which have primary concept of particles, behave like waves, when they move inside a solid of nanometric dimensions.

In the third decade of the twentieth century, Davison and Germer showed that electrons impinged against and in fact diffracted, as if they were waves, and followed Bragg's low of diffraction [26]. The details of the electron's waves are described in [102]. The illustration in Fig. 3.1 clearly shows the *wave-particle dualism* of the electron by means of the accumulation of many single shots, corresponding to independent electrons, in an interferometry experiment performed by A. Tonomura (for details see [102]).

In 1924, de Broglie assumed that to every particle of momentum p, a wave of wavelength

$$\lambda = \frac{\hbar}{p}, \tag{3.1}$$

whereas usually $\hbar$ is a Planck's constant ($\hbar = \frac{h}{2\pi}$) and

V. G. Plekhanov, *Isotope Low-Dimensional Structures*, SpringerBriefs in Physics,
DOI: 10.1007/978-3-642-28613-1_3, © The Author(s) 2012

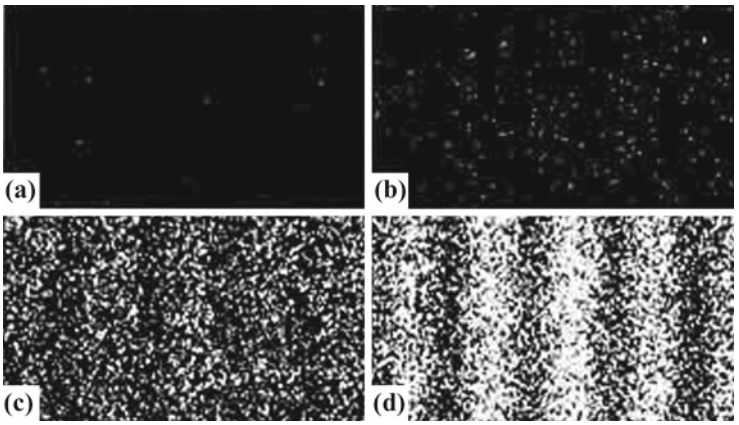

Fig. 3.1 Observing the wave-like properties of the electrons in the double slit experiment (after [102]). The pictures **a** ⟶ **c** have been taken at various times: pictures on the monitor after **a** 10 electrons, **b** 200 electrons, **c** 6,000 electrons, and **d** 140,000 electrons. Electrons were emitted at a rate of 10 per second. [after A. Tonomura, 2006, Double-slit experiment (http://www.hqrd.hitachi.co.jp/globaldoubleslit.cfm)]

$$p = \frac{\hbar}{\lambda} = \frac{h}{2\pi} \cdot \frac{2\pi}{\lambda} = \hbar k. \tag{3.2}$$

In (3.2) k is the so-called wave number. According to *quantum mechanics* the electron is described by successive quantum-mechanical states, which represent a certain probability that the particle may be located in a specific spatial region. These measures of probability can be calculated from the wave function Ψ that results from the solutions of a partial differential equation called the Schrödinger equation

$$\left[-\frac{\hbar^2}{2m}\nabla^2 + V(\overrightarrow{r}, t)\right]\Psi = i\hbar\frac{\partial\Psi}{\partial t}, \tag{3.3}$$

where ∇^2 is the operator $(\frac{\partial^2}{\partial x^2} + \frac{\partial^2}{\partial y^2} + \frac{\partial^2}{\partial z^2})$, and $V(\overrightarrow{r}, t)$ is the potential energy, which is generally a function of position and time. As is known, the function Ψ does not have a physical meaning, the product of Ψ by its conjugate (Ψ^*) is a real quantity, such that the indicated above probability dP of funding a particle in a small volume dV is given by

$$\mathrm{d}P = |\Psi|^2 \mathrm{d}V. \tag{3.4}$$

If the potential energy V is not time dependent, we can search for a solution to Eq. (3.3) of the form

$$\Psi(\overrightarrow{r}, \mathrm{t}) = \Psi(\overrightarrow{r})\mathrm{e}^{-i\omega t}. \tag{3.5}$$

Substituting Eq. (3.5) into (3.3) and writing $\mathrm{E} = \hbar\omega$, we can find the time-independent Schrödinger equation

$$\left[-\frac{\hbar^2}{2m}\nabla^2 + V(\overrightarrow{r})\right]\Psi(\overrightarrow{r}) = \mathrm{E}\Psi(\overrightarrow{r}) \tag{3.6}$$

for the time-independent wave function $\Psi(\overrightarrow{r})$. Schrödinger's equation can be solved exactly in a few cases (see, e.g. [15, 48, 49, 50]). Probably the simple stone is that of free particle, as for instance a free electron of energy E and mass m. In this case $\Psi(\overrightarrow{r}) = 0$ and the solution of Eq. (3.6) is easily found to be

$$\Psi = \mathrm{A}e^{i(\mathrm{kx}-\omega\mathrm{t})} + \mathrm{B}e^{i(-\mathrm{kx}-\omega\mathrm{t})} \tag{3.7}$$

where

$$k = \left(\frac{2m\mathrm{E}}{\hbar^2}\right). \tag{3.8}$$

Therefore, the free electron is described by a wave, which according to the de Broglie relation has momentum and energy given, respectively, by

$$p = \hbar k, \quad \mathrm{E} = \frac{p^2}{2m}. \tag{3.9}$$

In general, we will assume that the electron travels in one direction, for example, along the x-axis from left to right, and therefore the coefficient B in Eq. (3.7) is zero. The wave function for the free electron can simply be written as:

$$\Psi = \mathrm{A}e^{i(\mathrm{kx}-\omega\mathrm{t})}. \tag{3.10}$$

Another example in which Schrödinger's equation can be solved exactly is that of the hydrogen atom for which the potential is Coulombic, i.e., V varies with distance r between proton and electron in the form $1/r$. Solving Schrödinger's equation, one gets the well-known relation for the electron energies [48, 49, 50]:

$$\mathrm{E}_n = -\frac{m_r e^4}{2(4\pi\varepsilon_0)^2\hbar^2 n^2} = -\frac{13.6}{n^2}\,\mathrm{eV}, \quad n = 1, 2, 3, \ldots\ldots \tag{3.11}$$

In the last expression m_r is the reduced proton–electron mass ($m_r = \frac{M_p m}{M_p + m}$). In solid-state physics, the mathematical model of the hydrogen atom is often used, as for example, in the study of the effects of impurities and *excitons* in crystals [26]. Although the equation giving the values of the energy is similar to Eq. (3.11), the values of the *binding energy* E_n are much smaller since the dielectric constant of the medium has to substitute the value of the permittivity of vacuum ε_0. For instance, in the case of silicon, the value of the dielectric constant is about $12\varepsilon_0$ [103].

Another important relation that derives heuristically from the model described above is Heisenberg's uncertainty principle: in any experiment, the products of the uncertainties, of the particle momentum Δp_x and its coordinate Δx must be larger than $\hbar/2$, i.e.,

$$\Delta p_x \cdot \Delta x \geq \hbar/2. \tag{3.12}$$

There are of course corresponding relations for $\Delta p_y \cdot \Delta y$ and $\Delta p_z \cdot \Delta z$. It is important to remark that this indeterminacy principle is inherent to nature, and has nothing to do with errors in instruments that would measure p_x and x simultaneously. The second part of this principle is related to the accuracy in the measurement of the energy and the time interval Δt required for the measurement, establishing

$$\Delta \mathrm{E} \Delta t \geq \hbar/2. \tag{3.13}$$

So, *uncertainty principle* denotes that the location or the momentum of a particle, and its energy or its time of observation can only be determined imprecisely. This statement is very important as we are considering *nanoelectronic* applications, because the dimensions of such devices are so small that we can use the uncertainty principle to roughly estimate the relevant nanoelectronic effects, for example, the tunneling effect. In the following sections some important nanoelectronic structures will be discussed. Thereby it is inevitable to apply the wave model of matter to describe the behavior of the electrons involved. The upcoming example of the potential shows well that it is not possible to correctly determine the behavior of an electron in such configuration by using the classical-particle model.

In conclusion of this paragraph we should note that the interpretation above of $|\Psi|^2$ suggests the introduction of the term information. The information delivered by a measuring process is inversely proportional to the probability of localizing a particle in the observation space [102, 104]. Although this relation to information theory is interesting, the concept was not generally adopted by physicists.

3.2 Dimensionality and Density of States

As we know from solid-state physics, most physical properties significantly depend on the *density of states* (DOS) function S. The DOS function, at a given value E of energy, is defined such that $S(E)\Delta \mathrm{E}$ is equal to the number of states (i.e. solution of Schrödinger equation) in the interval energy ΔE around E (see, e.g. [3]). We also know that if the dimensions $L_i (i = x, y, z)$ are macroscopic and if proper boundary conditions are chosen, the energy levels can be treated as quasi-continuous [26]. On the other hand, in the case where any dimensions L_i gets small enough, the DOS function becomes discontinuous. Let us next obtain the DOS function for several low-dimensional solids (see, also [3, 74]).

We also know that every electron state is defined by the set of numbers (k_x, k_y, k_z). According to the Pauli exclusion principle there will be two electrons (spin up and

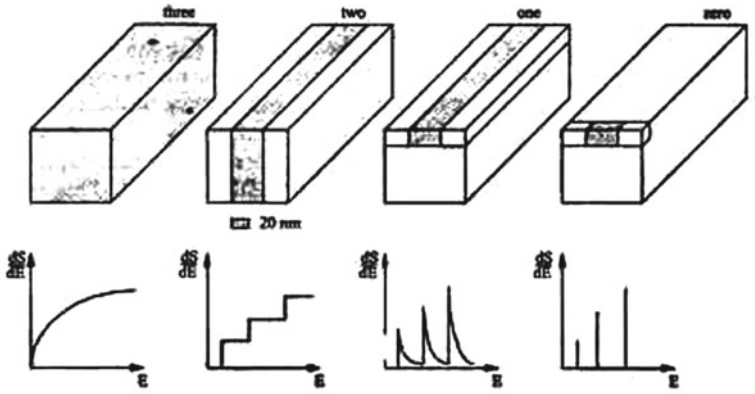

Fig. 3.2 Normal structures with different dimensions: normal solid-state body, quantum well, quantum wire, quantum dot. Additionally their DOS are illustrated

spin down) for each occupied state. Since the electron energy is proportional to k^2, the occupied points in k-space, expressed by the set of all combinations of values of k_x, k_y, k_z will be located inside a sphere of radius $k = k_{\max}$. On the other hand, the difference between two consecutive values of each k_i component ($i = x, y, z$) is $2\pi/L$. Therefore, each allowed value of $\overrightarrow{k}$ (k_x, k_y, k_z) should occupy a volume in k-space given by

$$\left(\frac{2\pi}{L}\right)^3 = \frac{(2\pi)^3}{V}, \tag{3.14}$$

where V is the volume of the crystal. Thus, the number of electron states with values lying between k and $k + \mathrm{d}k$ should be

$$2\frac{4\pi k^2 \mathrm{d}k}{(2\pi)^3 V} = \frac{V k^2 \mathrm{d}k}{\pi^2}, \tag{3.15}$$

where the factor 2 takes into account the spin. Since the $E = E(\overrightarrow{k})$ relation is given by Eq. (3.8), we have finally for the DOS function in energy the expression

$$\frac{\mathrm{d}S(E)}{\mathrm{d}E} = \frac{V}{2\pi^2}\left(\frac{2m^*}{\hbar^2}\right)^{3/2}\sqrt{E}. \tag{3.16}$$

From the last relation, we see that $\frac{\mathrm{d}S(E)}{\mathrm{d}E}$ increases as the square root of energy (see, Fig. 3.2).

The behavior of electrons when their motion is restricted along one direction in the wells of infinite height corresponds to a well-known problem in quantum mechanics, the so-called particle in a box of infinite wells [30].

In two-dimensional (2D) nanostructures carrier motion for both electrons and holes is not allowed in the direction perpendicular to the well, usually taken as the z-direction because of the potential wells. However, in the other two spatial directions (x, y) parallel to the crystal interfaces, the motion is not restricted, i.e. the electrons behave as free electrons. It is well-known from quantum mechanics that, in the case of infinite potentials barriers, the wave functions and energy levels of the bound electrons are given by

$$\Psi_n(\mathrm{z}) = \left(\frac{2}{\mathrm{a}}\right)^{1/2} \sin\left(\frac{\pi n z}{a}\right), \tag{3.17}$$

$$\mathrm{E}_n = \frac{\hbar^2 \pi^2}{2m^* \mathrm{a}^2} n^2, \qquad n = 1, 2, 3, \ldots \tag{3.18}$$

Here, m^* is the *effective mass* of the electrons in the well material for the motion along z-direction and a is the width of the well. From the last relation (3.18) we can derive several important consequences:

1. In general, *quantum size effects* will be more easily observable in quantum structures of very small size a, and for materials for which the electron effective mass is as small as possible. In this case, GaAs nanostructures are very convenient since $m^* \sim 0.067\, m_0$ [1, 14], where m_0 is the free electron mass. This is equivalent to saying that in materials for which the electron mobility or the free electron path are large (see above), quantum effects are easier to observe.
2. Quantum size effects, which require energy transitions of electrons between levels, are better observed at low temperatures, since the mean thermal energy of carriers is of the order of kT.

As was indicated above, the motion of electrons in the quantum well (QW) is confined only in one direction, z, but in the (x, y) planes the electrons behave as in a 3D solid. Therefore, the electron wave function is separable as the product of Ψ_x, Ψ_y and Ψ_z (see, also [3]) i.e.,

$$\Psi = \Psi_x \cdot \Psi_y \cdot \Psi_z \tag{3.19}$$

where, Ψ_x and Ψ_y satisfy the Schrödinger equation for a free electron, i.e., traveling wave, while Ψ_z is given by the Schrödinger equation with a square well potential $V(z)$ and therefore can be expressed in Eq. (3.17). The expression for the total energy of electrons in the potential well, can then be written as

$$E(k_x, k_y, n) = \frac{\hbar^2}{2m^*}(k_x^2 + k_y^2) + \mathrm{E}_n = \frac{\hbar^2}{2m^*}(k_x^2 + k_y^2) + \frac{\hbar^2 \pi^2}{2m^* \mathrm{a}^2} n^2, \quad n = 1, 2, 3, \ldots \tag{3.20}$$

where the quasi-continuous values of k_x, k_y are determined by the periodic boundary conditions as in the case of free electron in the bulk. Using the same algebra, we get for the DOS function in 2D case:

$$\frac{\mathrm{d}S(\mathrm{E})}{\mathrm{dE}} = \frac{2m^*}{\pi^2\hbar^2}. \tag{3.21}$$

Note that in the 2D case, the DOS function is a constant, independent of energy and exhibits a staircase-shaped energy dependence (see, also Fig. 3.4) in which all the steps are of the same height, but located at energies E_n given by (3.18). It can be appreciated that interval energy between 0 and E_1 is not allowed. For E such that $\mathrm{E}_1 < \mathrm{E} < \mathrm{E}_2$ the electrons will be located in the subband corresponding to $n = 1$ and the value will be $\frac{m^*}{\pi^2\hbar^2}$. For the energy interval between E_2 and E_3, the electrons can be located either in the $n = 1$ or in the $n = 2$ subbands, and consequently the DOS function would be twice the above value, i.e., $\frac{2m^*}{\pi^2\hbar^2}$ ($\frac{4m^*}{\pi^2\hbar^2}$; $\frac{4m^*}{\pi^2\hbar^2}$ etc., see Fig. 3.2). Such picture is a directly observed by *optical absorption* measurements [105]. When an electron is allowed only 1D motion (along. say, the x-direction), the energy is given by

$$E = \frac{\hbar^2 k_x^2}{2m^*} \tag{3.22}$$

A procedure analogous to that used above then yields for the DOS the expression

$$\frac{\mathrm{d}S(\mathrm{E})}{\mathrm{dE}} = \frac{1}{\pi}\left(\frac{2m^*}{\hbar^2}\right)\frac{1}{\sqrt{\mathrm{E}}}. \tag{3.23}$$

Equation (3.23) shows that the *DOS function* of a 1D electron gas (1D) has a square-root singularity at the origin. This result will have important consequences in the physical properties of quantum wires (QWRs).

Quantum dots (QDs) are often nanocrystals with all three dimensions in the nanometer range (L_x, L_y, L_z). In this case, there is no continuous DOS function, since there is quantization in three spatial directions. To consider the energy spectrum of a zero-dimensional system, we have to study the Schrödinger equation (3.6) with a confining potential that is a function of all three directions. The simplest case is the quantum box in the form of a parallelepiped with impenetrable wells. The corresponding potential, $V(x, y, z)$ is

$$V(x, y, z) = \left\{\begin{array}{l} 0, \text{ inside of the box,} \\ +\infty, \text{ outside of the box} \end{array}\right\}, \tag{3.24}$$

where the box is restricted by the conditions $0 \le x \le L_x, 0 \le y \le L_y, 0 \le z \le L_z$. Using the results of the above analysis discussed previously (see also [3]), one can write down the solutions of the Schrödinger equation for a box:

$$\mathrm{E}_{n_1,n_2,n_3} = \frac{\hbar^2\pi^2}{2m^*}\left(\frac{n_1^2}{L_x^2} + \frac{n_2^2}{L_y^2} + \frac{n_z^2}{L_z^2}\right), \quad n_1, n_2, n_3 = 1, 2, 3, \ldots\ldots\ldots \tag{3.25}$$

$$\Psi_{n_1,n_2,n_3}(x,y,z) = \sqrt{\frac{8}{L_x L_y L_z}} \sin\left(\frac{\pi x n_1}{L_x}\right) \sin\left(\frac{\pi y n_2}{L_y}\right) \sin\left(\frac{\pi z n_3}{L_z}\right). \quad (3.26)$$

Of fundamental importance is the fact that E_{n_1,n_2,n_3} is the total electron energy, in contrast to the previous cases, where the solution for the bound states in a QW and QWR gave us only the energy spectrum associated with the transverse confinement (see Eqs. (3.20) and (3.22)). Another unique feature is the presence of three discrete quantum numbers n_1, n_2, n_3 resulting straightforwardly from the existence of three directions of quantization. Thus, we obtain 3-fold discrete energy levels and wave functions localized in all three directions of the quantum box. In a QD of a parallelepipeds shape we have three quantum numbers n_1, n_2, n_3, that substitute for the three components of the wavevector $\vec{k} : k_x, k_y, k_z$. The discrete spectrum in a quantum box and the lack of free propagation of a particle in any direction are the main features distinguishing QDs from QWs and QWRs. As is well known, these features are typical for atomic systems as well [48–50].

Since in the case of QDs the electrons are totally confined, the energy spectrum is totally discrete and the DOS function is formed by a set of peaks (see, Fig. 3.2) in theory with no width and with infinite height. In practice, the peaks should have a finite width, as a consequence, for instance, of the interaction of electrons with lattice phonons and impurities.

3.3 Electron in Quantum Dot

If electron motion is quantized in all three possible directions, we obtain a new physical object, a *macroatom*. Questions concerning the usefulness of such objects for applications naturally arise from the point of view of their electronic applications. A fundamental question is the following: what is the current through a macroatom? A valid answer is that there exists the possibility of passing an electric current through an artificial atom due to tunneling of electrons through quantum levels of the macroatom (see, e.g. [106, 107]). The field of single electron tunneling (SET) comprises phenomena where the tunneling of a microscopic charge, usually carried by an electron or a Cooper pair, leads to microscopically observable effects (see, also [109, 110]). The basic principles governing single charge tunneling through QD are briefly outlined in this paragraph.

For the description of our task, let us imagine a *semiconductor* of nanometric size in the three spatial dimensions, for example a QD (see Fig. 3.2). Below we will show that even change of one elementary charge (electron) in such small systems has a measurable effect in the electrical and transport properties of the dot [107]. This phenomenon is known as Coulomb blockade, which we will discuss in the simplest possible terms (see, also [103]). Let us imagine a semiconductor dot structure, connected to electron reservoirs (e.g. drain and source) of each side by potential barriers or tunnel junctions (see, Fig. 3.3a). In order to allow the transport of electrons to or

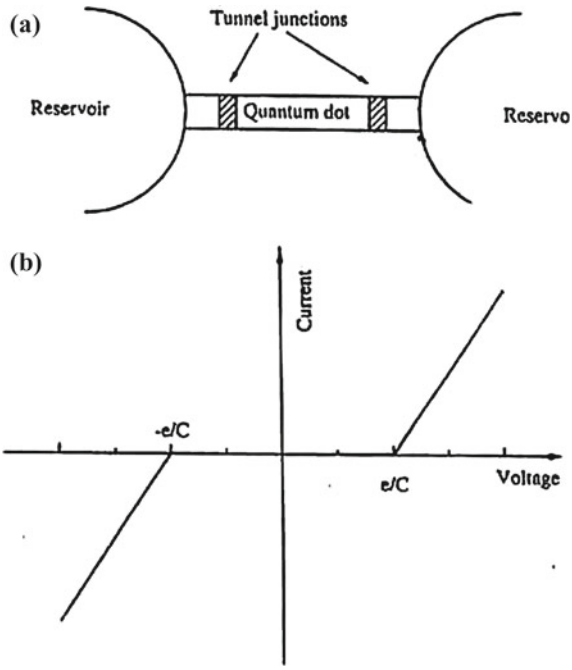

Fig. 3.3 **a** Scheme of a quantum system to observe Coulumb blockade effects; **b** I–V characteristics in a QD showing the Coulomb blockade effect

from reservoirs, the barriers will have to be sufficiently thin, so that the electrons can cross them by the tunnel effect. Further, suppose that we wish to change the number N of electrons in the dot by adding just one electron, which will have to tunnel for instance from the left reservoir into the dot. For this to happen, we will to provide the potential energy eV to the electron by means of a voltage source. If the charge in the QD is Q and its capacitance C, the potential energy is $Q^2/2C$. Therefore an energy of at least $e^2/2C$ will have to be provided to the electron, which means that for the electron to enter the dot, the voltage will have to be raised to at least $e^2/2C$. Since the electron can either enter the dot or leave (this process is equivalent to a hole entering the dot), we see that electrons cannot tunnel if

$$|V| < e/2C. \tag{3.27}$$

Therefore, there this is a voltage range, between $-e/2C$ and $e/2C$, represented in Fig. 3.3b, in which current cannot go through the dot, hence the name of Coulomb blockade given to this phenomenon (see, also [109] and references therein). Evidently, if the above process is continued and we keep adding more electrons, we will have the situation represented in Fig. 3.4, in which we will observe discontinuities in the current through the QD whenever the voltage acquires the values expressed by:

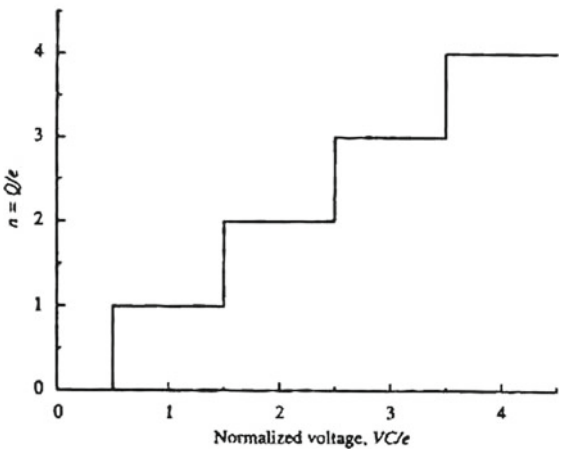

Fig. 3.4 Charging of a QD capacitor as a function of voltage, in normalized coordinates

$$V = \left(\frac{1}{2C}\right)(2n+1)\,\mathrm{e}, \qquad n = 0, 1, 2, 3, \ldots \tag{3.28}$$

Observe that in Fig. 3.4 we have made use of normalized coordinates, both in horizontal and vertical axes, to better appreciate the effect of the quantification in current and voltage.

It is also interesting to observe from the above equations that as the size of the QD is reduced, and therefore C gets smaller, the value of the energy necessary to change the number of electrons in the dot increases. In this case, it will be easier to observe the *Coulomb* blockade, since the changes in voltage and electric energy has to be much larger than the thermal energy kT at the working temperature, in order to observe measurable Coulomb blockade effects. Therefore, we should have for the capacitance:

$$C \ll \frac{\mathrm{e}^2}{kT}. \tag{3.29}$$

For this condition to be fulfilled, either the capacitance of the dot should be very small (values less than 10^{-16} F are very difficult to get) or we should work at very low temperatures, usually smaller than 1 K.

Another condition to observe SET is that the number of electrons in the dot should not fluctuate in equilibrium. Let us assume that the time taken for an electron to be transferred in or out of dot is of the order of $R_T C$, where R_T is the equivalent resistance of the tunnel barrier and C the capacitance of the dot. Fluctuations in the number of electrons in the dot induce changes in potential energy of the order of e^2/C. Therefore we should have, according to the uncertainty principle

$$\Delta E \cdot \Delta t = \frac{\mathrm{e}^2}{C} R_T C > h \tag{3.30}$$

and consequently for Coulomb blockade effects to be clearly observed we should have

$$R_T \gg \frac{h}{e^2} = 25.8\,\mathrm{k}\Omega. \tag{3.31'}$$

In single electron transport experiments, usually the current is measured, which is proportional to the conductance. In terms of the conductance, the above condition can be written as (for details, see, also [103, 107])

$$G \ll \frac{e^2}{h}. \tag{3.32}$$

In reality, electrical methods applied to QDs to realize useful devices are not the only method possible. The control of the electric current through the dots can also be realized by means of light, sound, etc. (see, e.g. [3, 4]). Consider here optical control of the dots and optoelectronic functions of 0D devices. The main peculiarities of the optical properties of QDs arise due to electron and hole quantization (see, also [111, 112]). In QDs fabricated from semiconductors with different E_g, the carrier energies have the form

$$E_e^{QD} = E_g^{QD} + \epsilon_n\,(n_1, n_2, n_3), \quad E_h^{QD} = -\epsilon_p(n_1', n_2', n_3'). \tag{3.33}$$

In this expression E_g^{QD} is the fundamental bandgap of the material of the QDs. Very often E_g^{QD} is less than the bandgap E_g of the surrounding material into which the dots are embedded, ϵ_n and ϵ_p depend on sets of three discrete quantum numbers for electrons and hole, respectively. The model dependences of E_g (3.24) can be used for estimation of the energy levels. Owing to these discrete energy spectra, QDs interact primarily with photons of discrete energies:

$$\hbar\omega = \frac{2\pi\hbar c}{\lambda} = E_g^{QD} + \epsilon_n(n_1, n_2, n_3) + \epsilon_p(n_1', n_2', n_3'). \tag{3.34}$$

In the last formula c is the velocity of light and λ is the wavelength of the light. The different combinations of quantum numbers (n_1, n_2, n_3) and (n_1', n_2', n_3') give a series of optical spectral lines, for which interaction between the dots and light is efficient. Importantly, the fact that $E_g^{QD} < E_g$ implies that the light interacting with the dots is not absorbed by the surrounding material (for details see [14, 113]).

The optical control of the electric current flowing through a QD can be explained with the help of a device that can be called a single-quantum-dot photodiode [112, 113]. In Fig. 3.5, we present the experimental results obtained [114] from excitation of the ground exciton state ($n_1 = n_2 = n_3 = n_1' = n_2' = n_3'$) of a single self-assembled $In_{0.5}Ga_{0.5}As$ QD embedded into a 360 nm-thick intrinsic GaAs layer. Since E_g(InGaAs) $< E_g$ (GaAs) the only optically part is the single $In_{0.5}Ga_{0.5}As$ QD. In [114] the experiments were carried out at 4.2 K. In Fig. 3.5, the photocurrent is plotted as a function of the electric bias for various wavelengths of illuminating

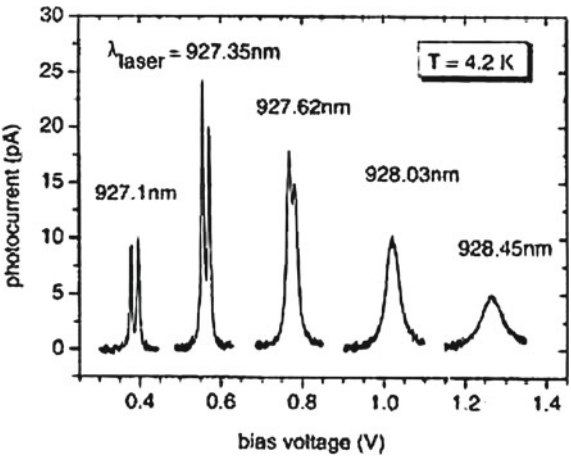

Fig. 3.5 Photocurrent resonance for various excitation wavelengths bias voltage. At low bias the fine structure splitting is fully resolved, at higher bias the linewidth is increased due to fast tunneling (after [114])

light. The wavelengths are indicated on the photocurrent curves. One can see that photocurrent–voltage dependences have, in fact, a pronounced resonant character. This is explained [114] by the fact that the quantized electron and hole energies are shorted under an applied electric field, as expected from the so-called Stark effect observable for atoms and molecules. When these energies are such that wavelength given by Eq. (3.34) corresponds to the illuminating light, the light excites electrons and holes inside the QW, which produces the measured photocurrent. As the applied bias increases, the energies are shifted to smaller values and the resonance wavelength increases. In Fig. 3.5, spectra for excitation of the same ground exciton state of the dot for different biases are shown. The observed photocurrent spectra are very narrow because a single dot is involved [14]. Spectral broadening becomes visible at high biases when the electron and hole energy levels decay as a result of the increased rate of tunneling from the dot (for details see [114]).

In conclusion we should underline that a very interesting challenge of future *nanoelectronics* is the control of switching device by just one electron (see, also below).

3.4 Excitons in Nanostructures

When a *semiconductor* (*insulator*) of direct bandgap E_g is shone with near—bandgap light, electron–hole pairs are created. If the electron and the hole were non-interacting only photon energies $\hbar\omega > E_g$ would be absorbed and E_g would be the absorption edge. The coulombic electron–hole interaction greatly modifies this picture. The electron–hole attraction gives rise to bound states of the relative motion of the exciton [115, 116]. The appearance of intense, narrow absorption lines below the fundamental absorption edge is the manifestation of these bound states.

In the case of confined systems for electrons and holes, such as QWs, QWRs and QDs, the excitonic effects are much more important than in bulk solids. In effect, as will be shown below, the binding energy of the electron–hole systems forming excitons is much higher in quantum confined systems than in the case of solids, and, therefore, the excitonic transitions can be observed even at temperatures close to room temperature, as close to the bulk case for which low temperatures are needed. This makes the role played by excitons in many optoelectronic devices of nanoscale very important (see, also [1–4, 15, 74, 114–119]). It represents the Coulombic binding between the conduction electron and the isotropic part of the Γ_8 hole. To the 0th approximation in Q, L, M the exciton states formed between the Γ_6 electron and the Γ_8 hole [120] are 4-fold degenerate and can be calculated like the exciton states in idealized bulk material (see, e.g. [115, 116]).

3.4.1 Excitons in Quantum Wells

In diamond—like *semiconductors* the topmost valence band is 4-fold degenerate at the zone center of the *Brillouin zone* (Γ_8 symmetry) (see e.g. [103]). In the spherical approximation the valence Hamiltonian can be written [118–120]

$$H_{\mathrm{v}}(\overrightarrow{k}) = \frac{\hbar^2 \overrightarrow{k^2}}{2m_{\mathrm{h}}} 1 + \frac{\hbar^2}{2m_{\mathrm{l}}} \left(\overrightarrow{k} \cdot \overrightarrow{J} \right)^2, \tag{3.35}$$

where 1 is the 4×4 identity matrix and $\overrightarrow{J}$ a spin 3/2 matrix. The effective masses related to the heavy (h) and light (l) hole masses are:

$$\frac{1}{m_{\mathrm{h}}} = \frac{1}{8m_{\mathrm{hh}}} - \frac{9}{8m_{\mathrm{lh}}}; \quad \frac{1}{m_{\mathrm{l}}} = -\frac{1}{2m_{\mathrm{hh}}} + \frac{1}{2\mathrm{M_{LH}}}. \tag{3.36}$$

1. a. To obtain Eq. (3.35) we have used the fact that for $\overrightarrow{k} \parallel \overrightarrow{J}$ heavy hole states correspond to $m_j = \pm 3/2$ and light hole states to $m_j = \pm 1/2$.

The relative motion of the *exciton* is thus described by Hamiltonian which is also a 4×4 matrix:

$$H_{\mathrm{exc}} = \left[\frac{p^2}{2m_c^*} - \frac{\mathrm{e}^2}{\mathrm{kr}} \right] 1 - H_{\mathrm{v}} \left(\frac{p}{\hbar} \right). \tag{3.37}$$

Baldereschi and Lipari [121] have shown that H_{exc} can be rewritten as

$$H_{\mathrm{exc}} = P(\overrightarrow{r}, \overrightarrow{p}) 1 + \begin{bmatrix} \mathrm{Q} & \mathrm{L} & \mathrm{M} & 0 \\ L^* & -\mathrm{Q} & 0 & \mathrm{M} \\ M^* & 0 & -\mathrm{Q} & -\mathrm{L} \\ 0 & \mathrm{M}^* & -\mathrm{L}^* & \mathrm{Q} \end{bmatrix} \tag{3.38}$$

where P, Q, L, M are functions of $\overrightarrow{r}$ and $\overrightarrow{p}$ which have S-symmetry (P) and D-symmetry (Q, L, M) respectively. The important point is that Q, L, M only involve valence band parameters, whereas P also involves m_c^* and the Coulombic term $-e^2/k\mathrm{r}$. In fact:

$$\mathrm{P}(\overrightarrow{r}, \overrightarrow{p}) = \frac{p^2}{2\mu_0} - \frac{\mathrm{e}^2}{k\mathrm{r}}, \tag{3.39}$$

where:

$$\frac{1}{\mu_0} = \frac{1}{m_c^*} + \frac{\gamma_1}{m_0}. \tag{3.40}$$

Here, γ_1 is one of the Luttinger parameters [118] describing the Γ_8 hole kinematics. The diagonal term $P(\overrightarrow{r}, \overrightarrow{p})$ is thus much larger than the others. It represents the Coulombic binding between the conduction electron and the isotropic part of the Γ_8 hole (see also [120]). The zeroth approximation in Q, L, M the exciton states formed between the Γ_6 electron and the Γ_8 hole are 4-fold degenerate and can be calculated like the exciton states in idealized bulk materials (see, e.g. [115, 116, 120]) except that the reduced mass of the exciton involves neither the heavy hole nor the light hole masses but an average of the two. As shown by Baldereschi and Lipari [121], the corrections to the 0th approximation are very small under most circumstances (see, also [122]).

To calculate exciton states in QW heterostructures, one should add the barrier potentials for the electrons and holes to Eq. (3.38) which have the next expression

$$V_{\mathrm{barr}}(z_\mathrm{e}, z_\mathrm{h}) = V_\mathrm{e} Y\left(z_\mathrm{e}^2 - \frac{L^2}{4}\right) + V_\mathrm{h} Y\left(z_\mathrm{h}^2 - \frac{L^2}{4}\right), \tag{3.41}$$

where L is the QW thickness and V_e, V_h the barrier heights for the electrons and holes. Once again we have neglected some band structure effects, e.g. the effective mass and dielectric mismatches between the host materials (see also [117]). For the L values where the size quantization is important, we expect the z_e, z_h motion to be forced by the QW effects. We thus need to keep the exact hole masses in order evaluate the hole confinement energies correctly. This precludes the use of Baldareschi and Lipari's type of approach which is based on a suitable averaging of heavy and light hole masses. Till date, time there does not exist any fully satisfactory treatment of the exciton binding in quantum nanostructures (see, also [123]). Miller et al. [124] and Greene and Bajaj [125, 126] have approximated the exciton Hamiltonian (see also [120]) by

$$H_{\mathrm{ex}} = (P + V_{\mathrm{barr}})1 + \begin{bmatrix} \mathrm{Q} & & & 0 \\ & -\mathrm{Q} & & \\ & & \mathrm{Q} & \\ 0 & & & \mathrm{Q} \end{bmatrix} \tag{3.42}$$

Miller et al. took [124] V_e, V_h to be infinite, whereas Greene and Bajaj [117] accounted for the finite barrier effects; both groups were specifically interested in

GaAs-$Ga_{1-x}Al_xAs$ QWs. The advantage of including Q in H_{ex} is that a correct evaluation of the size quantization of the holes can be obtained. The drawback of this approximation is the inclusion of terms (brought by Q) for the in-plane exciton motion which are, in principle, as small as the last over terms L, M (although the latter are off diagonal). If we remember that the L, M terms actually give rise to strong anticrossings between the hole subbbands [127, 128, 129], there is some possibility that they can significantly contribute to the excitonic binding itself (see, also [117]).

As the *exciton* Hamiltonian Eq. 3.42 is a diagonal matrix, the excitons fall into two categories; the heavy hole (P+Q) and the light hole (P−Q) excitons. The heavy hole exciton Hamiltonian corresponds to $m_j = \pm 3/2$ and is written as

$$H_{ex}^{hh} = \frac{p_{z_e}^2}{2m_c^*} + \frac{p_{z_h}^2}{2m_{hh}^*} - \frac{e^2}{k|\overrightarrow{r_e} - \overrightarrow{r_h}|} + V_e Y\left(z_e^2 - \frac{L^2}{4}\right) + V_h Y\left(z_h^2 - \frac{L^2}{4}\right) + \frac{p_\perp^2}{2\mu_{hh}}, \tag{3.43}$$

where m_{hh} and μ_{hh} are defined by

$$\frac{1}{m_{hh}} = \frac{1}{m_0}(\gamma_1 - 2\gamma_2) \quad \text{and} \quad \frac{1}{\mu_{hh}} = \frac{1}{m_c^*} + \frac{1}{m_0}(\gamma_1 + 2\gamma_2). \tag{3.44}$$

The light hole exciton Hamiltonian corresponds to $m_j = \pm 1/2$ and is written as:

$$H_{ex}^{hh} = \frac{p_{z_e}^2}{2m_c^*} + \frac{p_{z_h}^2}{2m_{lh}^*} - \frac{e^2}{k|\overrightarrow{r_e} - \overrightarrow{r_h}|} + V_e Y\left(z_e^2 - \frac{L^2}{4}\right) + V_h Y\left(z_h^2 - \frac{L^2}{4}\right) + \frac{p_\perp^2}{2\mu_{lh}}, \tag{3.45}$$

where m_{hh} and μ_{lh} are given by the expression:

$$\frac{1}{m_{lh}} = \frac{1}{m_0}(\gamma_1 + 2\gamma_2) \quad \text{and} \quad \frac{1}{\mu_{lh}} = \frac{1}{m_c^*} + \frac{1}{m_0}(\gamma_1 - 2\gamma_2), \tag{3.46}$$

where γ_1 and γ_2 are well-known Luttinger parameters [118].

Thus, the heavy hole and light hole excitons again resemble those obtained in idealized QW structures. However, μ_{lh} is not necessarily smaller than μ_{hh}. In fact in GaAs the opposite is true: $\mu_{lh} = 0.051\,m_0$ and $\mu_{hh} = 0.04\,m_0$ whereas $m_{lh} = 0.08 m_0$ and $m_{hh} = 0.45\,m_0$ (see e.g. [3]). The inclusion of the Q term in H_{ex} inverts the parts played by the heavy and light masses along and perpendicular to the z axis. The heavy hole exciton is indeed heavy along z but light in the layer plane and vice versa. Thus in GaAs-$Ga_{1-x}Al_xAs$ QW, the curves which represent the binding energies versus the GaAs slab thickness of the two kinds of excitons should cross. For large wells the light and heavy hole confinement (governed by m_{lh} and m_{hh},

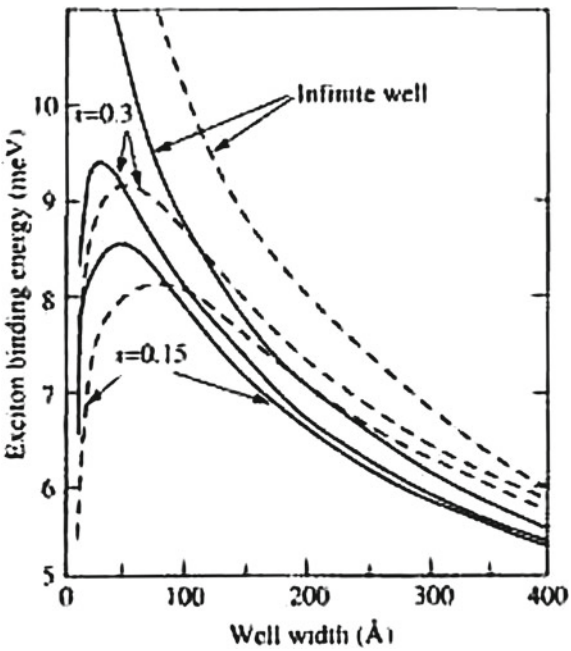

Fig. 3.6 Variation of the binding energy of the ground state E_{1s} of the heavy-hole exciton (*solid lines*) and the light-hole (*dashed lines*) as a function of the GaAs QW size (L) for aluminium concentration $x = 0.15$ and 0.3 and for infinite potential wells (after [117])

respectively) are almost complete and the light hole exciton is more tightly bound because its effective bulk Rydberg is larger than that of the heavy holes. On the other hand, for narrow GaAs wells, the light holes are less confined than the heavy holes. The Coulombic interaction between the electron and the hole in the light hole exciton is thus weaker than the one in the heavy hole exciton. Consequently, the light hole exciton is less bound than the heavy hole exciton. Figure 3.6 shows Bajaj [117] results concerning the ground bound exciton states in GaAs-$Ga_{1-x}Al_xAs$ QWs for two aluminum mole fractions $x = 0.15$ and $x = 0.3$. In these curves, the Dingle's rule [130] which states that the conduction band shares (85%) of the total bandgap difference between GaAs and $Ga_{1-x}Al_xAs$ has been used. Otherwise, the overall shapes of these curves look familiar: the exciton binding energies admit a maximum value versus the GaAs well thickness, whose location and amplitude depend on V_e, V_h, and μ_{hh} and μ_{lh}.

To summarize, the *Coulombic* bound states in heterostructures are qualitatively well understood [3]. The effect of off-diagonal terms in the exciton Hamiltonian, however, is an issue for quantitative understanding. We should remember that the 2D can only be approached hypothetically in infinitely QW. Figure 3.7 illustrates the results of calculations of the exciton biding energy as a function of the width of an infinitely deep CdTe QW [3]. As is well known the magnitude of the bulk exciton binding energy for CdTe is 10.1 meV (see, e.g. [120]). The negative values on the graph of Fig. 3.7 illustrate that it is indeed a bound state. From Fig. 3.7 it can be seen that 2D exciton binding energy is equal for meaning of bulk *exciton binding energy*.

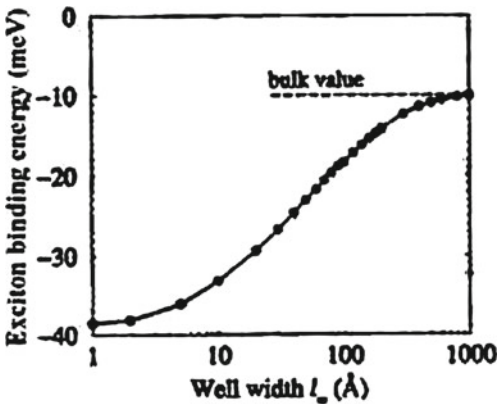

Fig. 3.7 Exciton binding energy in an infinitely deep CdTe QW (after [3])

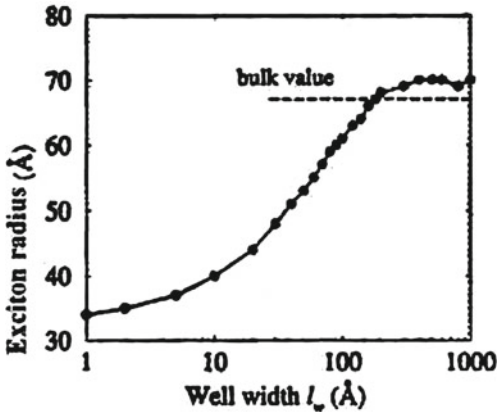

Fig. 3.8 Bohr radius of 2D exciton in an infinitely deep CdTe QW (after [3])

Figure 3.8 displays the corresponding Bohr radii r_{ex} for the energies of Fig. 3.7. Remembering that the the Bohr radius in bulk, $r_{ex}(3D) = 67\,\text{Å}$, then the 2D limit, i.e.,

$$\text{Lim}\, r_{ex}(2D) = \frac{r_{ex}(3D)}{2} \tag{3.47}$$

$$l_w \longrightarrow 0$$

is satisfied. The 3D limit is obeyed, although the data on the graph show a slight scatter around the bulk radii of 67 Å. According to [3], the source of this discrepancy is numerical accuracy. At the larger well widths, the wave function needs to be known at many points in order to calculate the binding energy to very high tolerance (according [3] thus leading to long computational times).

To conclude this paragraph we should note that the *Coulombic interaction* produces an excitonic series at every subband [74]. But normally only 1S exciton is visible for each transition. In very good QWs it is, however, sometimes possible to

distinguish the 2S exciton [131]. The relative positions offer a very good guide to the actual exciton binding energy. In practice, the most important effect of the Coulomb interaction on QW band structure is the appearance of strong, sharp spectral resonances just below the band edge for the first electron-heavy-hole and electron-light-hole transition (for details see [131]).

3.4.2 Excitons in Quantum Wires

1D semiconductor structures have received interest in recent years, and promising advances have been obtained in quantum-wire fabrication and in application, e.g., photodetectors, photodiodes, and laser devices [131–135]. In analogy to the in-plane dispersion discussed above, in a QWR it is possible to decouple the motion along the length of the wire. Taking the axis of the wire along x (see, also Fig. 3.2) the total potential $V(x, y, z)$ can always be written as the sum of a 2D confinement potential plus the potential along the wire, i.e.,

$$V(x, y, z) = V(x) + V(y, z). \tag{3.48}$$

The eigenfunction can then be written as a product of two components:

$$\Psi(x, y, z) = \Psi(x)\Psi(y, z). \tag{3.49}$$

Substituting both (Eqs. (3.48) and (3.49)) into general 3D Schrödinger equation for constant effective mass, then

$$-\frac{\hbar^2}{2m^*}\left(\frac{\partial^2}{\partial x^2}+\frac{\partial^2}{\partial y^2}+\frac{\partial^2}{\partial z^2}\right)\Psi(x)\Psi(y,z)+[V(x)+V(y,z)]\Psi(x)\Psi(y,z). \tag{3.50}$$

Writing the energy as a sum of terms associated with two components of the motion, we get

$$-\frac{\hbar^2}{2\mathrm{m}^*}\left(\Psi(y,z)\frac{\partial^2\Psi(x)}{\partial x^2}\right)+\Psi(x)\frac{\partial^2\Psi(y,z)}{\partial y^2}+\Psi\left(x0\frac{\partial^2\Psi(y,z)}{\partial z^2}\right)$$
$$\times\,\Psi(y,z)V(x)\Psi(x)+\Psi(x)V(y,z)\Psi(y,z)=(\mathrm{E}_x+\mathrm{E}_{y,z})\Psi(x)\Psi(y,z). \tag{3.51}$$

Now we can write

$$-\frac{\hbar^2}{2m^*}\left(\Psi(y,z)\frac{\partial^2\Psi(x)}{\partial x^2}\right)+\Psi(y,z)V(x)=\Psi(y,z)\mathrm{E}_x\Psi(x) \tag{3.52}$$

$$-\frac{\hbar^2}{2m^*}\left[\Psi(x)\frac{\partial^2\Psi(y,z)}{\partial y^2}+\Psi(x)\frac{\partial^2\Psi(y,z)}{\partial z^2}\right]+\Psi(x)V(y,z)\Psi(y,z)$$
$$=\Psi(x)\mathrm{E}_{y,z}\Psi(y,z). \tag{3.53}$$

In the above, $\Psi(y,z)$ is not acted upon by any operator in the first equation, and similarly for $\Psi(x)$ in the second equation, and thus they can be divided out. In addition, the potential component along axis of the wire $V(x)=0$, giving the final decoupled equations of motion as follows:

$$-\frac{\hbar^2}{2m^*}\frac{\partial^2\Psi(x)}{\partial x^2}=\mathrm{E}_x\Psi(x) \tag{3.54}$$

and

$$-\frac{\hbar^2}{2m^*}\left[\frac{\partial^2\Psi(y,z)}{\partial y^2}+\frac{\partial^2\Psi(y,z)}{\partial z^2}\right]+V(y,z)\Psi(y,z)=\mathrm{E}_{y,z}\Psi(y,z). \tag{3.55}$$

Equation (3.54) is satisfied by a plane wave of the form $\exp(\mathrm{ik}_x x)$, thus giving the standard dispersion relation:

$$\mathrm{E}_x=\frac{\hbar^2\mathrm{k}^2}{2m^*}. \tag{3.56}$$

The second of the last equations of motion, Eq. (3.55), is merely the Schrödinger equation for the 2D confinement potential characterizing a QWR.

Further, we consider the cylindrical QWR and we use the polar coordinate. With definition of the modulus r and angle θ as in ordinary case, the Cartesian coordinates then follow as:

$$y=r\sin\theta \quad \text{and} \quad z=r\cos\theta. \tag{3.57}$$

and

$$r=\sqrt{\mathrm{y}^2+\mathrm{z}^2}. \tag{3.58}$$

The wave function $\Psi(y,z)$ can clearly be written in terms of the new variables r and θ; however, the circular symmetry of the wave functions should not have a dependence on the angle θ. Thus, the wave function can actually be written as $\Psi(r)$, and the Schrödinger equation therefore becomes:

$$-\frac{\hbar^2}{2m^*}\left(\frac{\partial^2}{\partial y^2}+\frac{\partial^2}{\partial z^2}\right)\Psi(r)+V(r)\Psi(r)=\mathrm{E}_r\Psi(r), \tag{3.59}$$

where the index on E_r just indicates that this eigenvalue is associated with the confined cross-sectional motion, as opposed to the unconfined motion along the axis of the wire. In addition, the circular symmetry of the potential which defines the wire can be written as $V(r)$. Now:

$$\left(\frac{\partial}{(\partial y)}\right)\Psi(r) = \left(\frac{\partial}{(\partial r)}\right)\Psi(r)\cdot\left(\frac{(\partial r)}{(\partial y)}\right). \tag{3.60}$$

Differentiating both sides of Eq. (3.58) with respect to y, gives:

$$\frac{\partial r}{\partial y} = \frac{1}{2}(y^2+z^2)^{-\frac{1}{2}}\cdot 2y = \frac{y}{r}. \tag{3.61}$$

Hence:

$$\frac{\partial}{\partial y}\Psi(r) = \frac{\partial}{\partial r}\Psi(r)\cdot\frac{y}{r}. \tag{3.62}$$

The second derivative is then:

$$\frac{\partial}{\partial y}\frac{\partial}{\partial y}\Psi(r) = \frac{\partial}{\partial y}\left[\frac{\partial}{\partial r}\Psi(r)\cdot\frac{y}{r}\right]. \tag{3.63}$$

and thus:

$$\frac{\partial^2}{\partial y^2}\Psi(r) = \frac{y^2}{r^2}\frac{\partial^2}{\partial r^2}\Psi(r) + \frac{\partial}{\partial r}\left(\frac{1}{r} - \frac{y}{r^2}\frac{\partial r}{\partial y}\right) \tag{3.64}$$

Finally:

$$\frac{\partial^2}{\partial y^2}\Psi(r) = \frac{1}{r}\frac{\partial}{\partial r}\Psi(r) - \frac{y^2}{r^3}\frac{\partial}{\partial r}\Psi(r) + \frac{y^2}{r^2}\frac{\partial^2}{\partial r^2}\Psi(r) \tag{3.65}$$

and similarly for z, hence:

$$\left(\frac{\partial^2}{\partial y^2}+\frac{\partial^2}{\partial z^2}\right)\Psi(r) = \frac{2}{r}\frac{\partial}{\partial r}\Psi(r) - \frac{(y^2+z^2)}{r^3}\frac{\partial}{\partial r}\Psi(r) + \frac{(y^2+z^2)}{r^2}\frac{\partial^2}{\partial r^2}\Psi(r). \tag{3.66}$$

Recalling that $y^2+z^2=r^2$, then

$$\left(\frac{\partial^2}{\partial y^2}+\frac{\partial^2}{\partial z^2}\right)\Psi(r) = \frac{1}{r}\frac{\partial}{\partial r}\Psi(r) + \frac{\partial^2}{\partial r^2}\Psi(r). \tag{3.67}$$

Substituting into Eq. (3.59) gives the final form for the Schrödinger equation as follows:

$$-\frac{\hbar^2}{2m^*}\left[\frac{1}{r}\frac{\partial}{\partial r}+\frac{\partial^2}{\partial r^2}\right]\Psi(r) + V(r)\Psi(r) = \mathrm{E}_r\Psi(r). \tag{3.68}$$

In this case, reliance has been made on the specific form of the kinetic energy operator, and hence this Schrödinger equation is only valid for a constant effective mass. The numerical solution of Eq. (3.68) is shown in Fig. 3.9 [3]. This figure displays the result of calculations of the electron confinement energy versus the wire radius, for GaAs wire surrounded by $Ga_{0.8}Al_{0.2}As$, for constant effective mass. As expected, the confinement energy decreases with increasing radius and the odd-

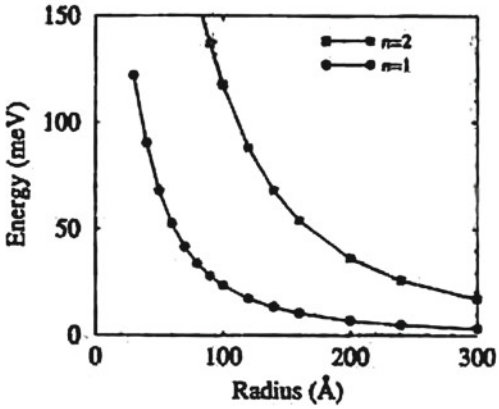

Fig. 3.9 The confinement energy in a finite barrier circular cross-section QWR (after [3])

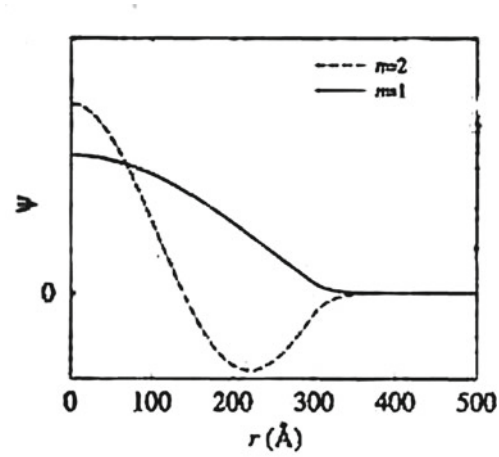

Fig. 3.10 The radial component of the wave function $\Psi(r)$ for the lowest two eigenstates in a finite-barrier QWR with radius 300 Å of circular cross-section (after [3])

parity eigenstate is of higher energy than for even. This latter point is highlighted in Fig. 3.10, which plots the radial motion Ψ(r) for the 300 Å radius wire. The even—($n = 1$) and odd—($n = 2$) parity nature of the eigenstates can clearly be seen (for details see [135] and references therein).

3.4.3 Excitons in Quantum Dots

It is perhaps easier to deal with a finite barrier QD with spherical rather than cuboid symmetry. The approach is rather similar to that derived earlier for the circular cross-section QWR. Given the spherical symmetry of the potential, then the wave function would also be expected to have spherical symmetry, hence the Schrödinger equation

for a constant effective mass could be written (see e.g. [14, 74]) as

$$-\frac{\hbar^2}{2m^*}\left(\frac{\partial^2}{\partial x^2}+\frac{\partial^2}{\partial y^2}+\frac{\partial^2}{\partial z^2}\right)\Psi(r)+V(r)\Psi(r)=\mathrm{E}_r\Psi(r), \tag{3.69}$$

where the index on E_r has been added to indicate that this energy is associated with the confinement along the radius. In this case:

$$r=\sqrt{x^2+y^2+z^2}. \tag{3.70}$$

The transition can be made from Cartesian (x, y, z) to spherical polar coordinates, in effect just r, in the same way above. Using Eq. (3.66), each of the three Cartesian axes gives an equation of the following form:

$$\frac{\partial^2}{\partial x^2}\Psi(r)=\frac{1}{r}\frac{\partial}{\partial r}\Psi(r)-\frac{x^2}{r^3}\frac{\partial}{\partial r}\Psi(r)+\frac{x^2}{r^2}\frac{\partial^2}{\partial r^2}\Psi(r). \tag{3.71}$$

Therefore, the complete $\nabla^2\Psi(r)$ is given by:

$$\begin{aligned}\left(\frac{\partial^2}{\partial x^2}+\frac{\partial^2}{\partial y^2}+\frac{\partial^2}{\partial z^2}\right)\Psi(r)=&\frac{3}{r}\frac{\partial}{\partial r}\Psi(r)-\frac{(x^2+y^2+z^2)}{r^3}\frac{\partial}{\partial r}\Psi(r)\\&+\frac{(x^2+y^2+z^2)}{r^2}\frac{\partial^2}{\partial r^2}\Psi(r).\end{aligned} \tag{3.72}$$

and

$$\left(\frac{\partial^2}{\partial x^2}+\frac{\partial^2}{\partial y^2}+\frac{\partial^2}{\partial z^2}\right)\Psi(r)=\frac{2}{r}\frac{\partial}{\partial r}\Psi(r)+\frac{\partial^2}{\partial r^2}\Psi(r). \tag{3.73}$$

Substituting into the Schrödinger equation then:

$$-\frac{\hbar^2}{2m^*}\left(\frac{2}{r}\frac{\partial}{\partial r}+\frac{\partial^2}{\partial r^2}\right)\Psi(r)+V(r)\Psi(r)=\mathrm{E}_r\Psi(r). \tag{3.74}$$

Such spherical symmetric Schrödinger equations have been investigated before (see e.g. [48, 49, 50]). The last equation as in the previous case, is numerically solved and Fig. 3.11 shows the results of calculations of the three lowest energy levels of a spherical GaAs QD surrounded by a finite barrier composed of $Ga_{0.8}Al_{0.2}As$, with a sharp boundary. In fact, the formalism above, as that of the circular *cross-section* QWR, is applicable for any radial potential profile $V(r)$, e.g. it is also valid for diffused interfaces [3]. Again, the behavior of the energies as a function of the spatial dimension, as shown in Fig. 3.11, is as expected in confined systems, namely the confinement energy decreases as the size of the system increases. Figure 3.12 displays the corresponding radial components of the wave functions. It can be seen

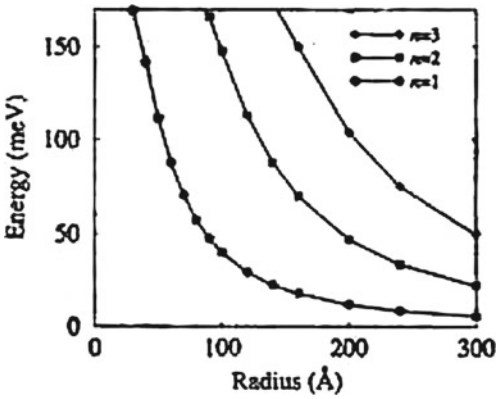

Fig. 3.11 The confinement energy in a spherical GaAs QD surrounded by a $Ga_{0.8}Al_{0.2}As$ barrier (after [3])

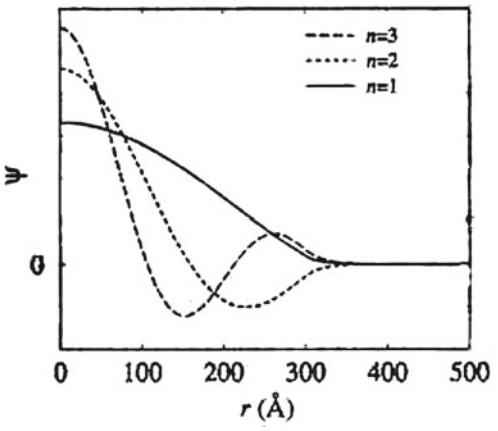

Fig. 3.12 The wave functions of the three lowest energy states in the 300 Å spherical QD (after [3])

that they all have a maximum at the center of the potential and that as the principal quantum number n increases, then the number of nodes increases.

3.5 Biexcitons in Quantum Dots

In 1958, Moskalenko [136] and Lampert [137] suggested that in crystals besides *excitons*, more complex electronic quasi-particles might exist, made up of three or four carriers. The latter, consisting of two electrons and two holes is well known as *biexcitons* or *excitonic molecules* [138]. As the density of excitons is increased, biexcitons are formed by increasing the light intensity. Biexcitons can be generated either through ordinary excitation of the crystal or by two-photon absorption each photon having an energy

$$h\nu = \mathrm{E}_x - \frac{\mathrm{E}_{\mathrm{B_{xx}}}}{2}, \tag{3.75}$$

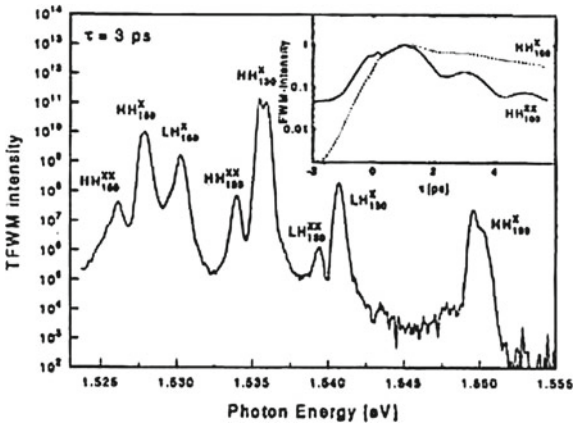

Fig. 3.13 Spectrally resolved four-wave mixing at $\tau = 3$ ps showing the heavy hole and light hole biexcitons. Insert shows the four-wave mixing intensity of the heavy hole exciton and biexciton as a function of delay (after [140])

where $E_{B_{xx}}$ is the biexciton binding energy and E_x is the exciton energy

$$E_x = E_g - E_{B_x} + \frac{\hbar^2 k^2}{2m_x}. \tag{3.76}$$

In the last relation E_g is the bandgap energy, E_{B_x} is the *exciton binding energy*, and $\frac{\hbar^2 k^2}{2m_x}$ is the kinetic energy with which an exciton moves through the crystal (see, also [139]).

Compared to the bulk material, an increased stability of biexcitons due to the 2D carrier confinement is observed for typical III–V structures like GaAs/AlGaAs QWs [124, 140] (see Fig. 3.13) or for wide bandgap II–VI materials like CdZnSe/ZnSe [141]. As a consequence of the enhanced biexciton binding energy, a variety of optical properties, like e.g., the photoluminescence (PL) spectrum, the optical gain or the four-wave mixing signal especially in wide bandgap II–VI QWs are strongly influenced by biexcitons (see [141] and references therein).

Below, we briefly review some results obtained from *optical spectroscopy* on epitaxially grown single SQDs based on II–VI and II–N compounds. As indicated above, the biexciton (XX) or X_2 is a four-particle state. In its lowest energy state configuration, two electrons and two holes with antiparallel spins occupy the first quantized state of the conduction and the valence band in the SQDs, respectively (see, e.g. [13]). We should add that the QDs in the material systems described here are quite small with diameters in the order of 10 nm and heights of a few nm. The biexciton state is therefore a singlet state with a total spin of $J = 0$. Thus, the exciton state X represents the final state for the biexciton recombination (see, also [144]). In II–VI semiconductors, as in III–V materials with a zincblende crystal lattice, Coulomb interaction leads to positive biexciton binding energies (see Eq. (3.76)), i.e., the energetic distance between XX (X_2) and X smaller than the energy difference between the first exciton state and the ground state. A typical optical fingeprint for the X_2 is therefore an additional PL line at the low energy side of the exciton emission

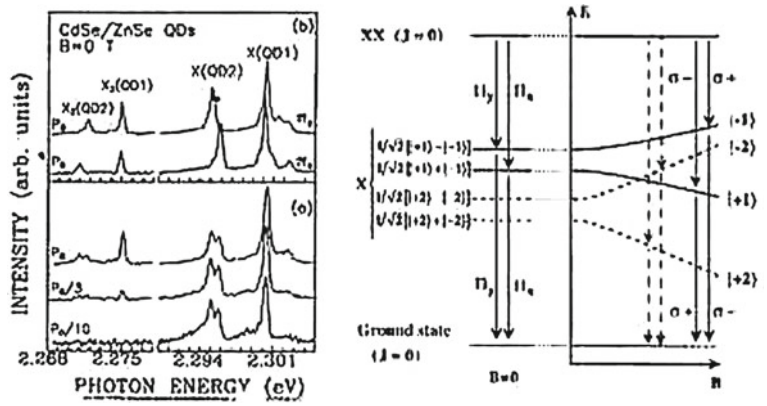

Fig. 3.14 *Left side* Excitonic (X) and biexcitonic (X_2) emission from two individual CdSe/ZnSe SQDs for different excitation powers. The PL spectra shown in the lower panel are unpolarized, the data presented in the upper panel represent linearly polarized PL spectra (π_x and π_y, respectively). *Right side* Energy level scheme for the biexciton-exciton cascade in a QD (after [141])

X that exhibits a strong (quadratic) dependence on the excitation power [139]. This behavior is clearly visible in the left panel of Fig. 3.14. At low excitation density, the PL spectrum of CdSe/ZnSe SQDs consists of emission peaks stemming from exciton recombination of two individual QDs. With rising excitation density additional lines emerge, red shifted by about 24 meV with respect to the excitonic emission X, and rapidly increasing in intensity, which can be attributed to biexciton emission X_2. The biexciton binding energy is obviously much larger than in III–As based QDs where typical values of a few meV ($\sim$2 meV [140]) have been determined (see also [139–143]). When having a closer look at the PL spectra presented in Fig. 3.14, some more information can be extracted. One should have in mind that in QDs, the light hole level is shifted to higher energies due to strain and confinement and thus, excitons are formed between electrons and heavy holes. The ground state of a heavy hole exciton in an SQD is a spin quadruplet, which can be by the z-component (= component, according [141] in growth direction) of the total exciton spin J_z. If the z-component of the electron spin, $s_z = \pm 1/2$, and the z-component of the total angular momentum of the heavy hole $j_z = \pm 3/2$, are antiparallel, in such case, we get $J_z = s_z + j_z = \pm 2$ (the dark exciton states [142]).

In II–VI QDs the energy difference Δ_0 between bright and dark exciton states that is given by the isotropic electron–hole interaction energy, amounts to about 1 meV and more which is nearly an order of magnitude larger than in InAs/GaAs QDs [14]. As can be seen in Fig. 3.14, the exciton fine structure is reflected both in the exciton and in the biexciton recombination: SQD1 does not show a significant splitting of the exciton PL signal, while SQD2 exhibits a doublet with an energy separation of almost 1 meV indicating a reduced QD symmetry. Exactly the same behavior is observed in the corresponding biexciton lines. Moreover, the high energy component of the X emission in SQD2 (π_x polarized) corresponds to the low energy

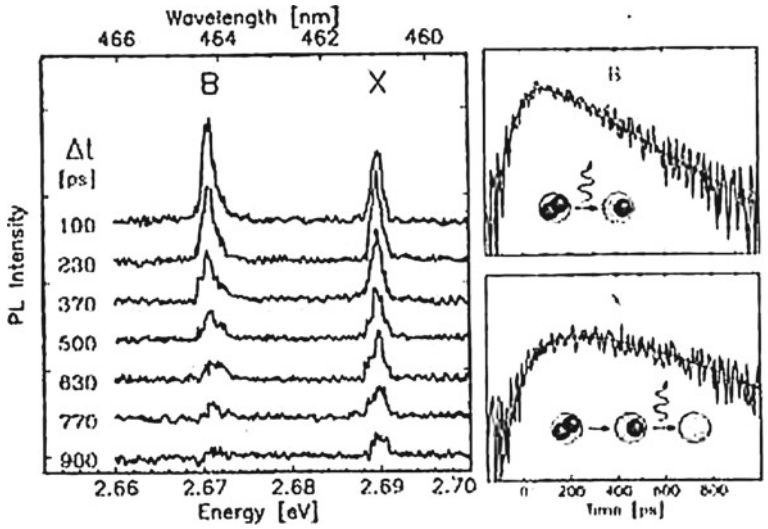

Fig. 3.15 *Left panel* Transient PL spectra from a single CdSe/ZnSe QD showing the single exciton X and the biexciton transition (here denoted by $B = X_2$). *Right panel* Decay curves for the exciton and the biexciton PL signal (for details see text) (after [141])

component of the X_2 emission and vice versa, in agreement with energy level scheme (see Fig. 3.14). All these effects are easily accessible in wide bandgap II–VI QDs because the characteristic energy splitting are significantly enhanced with respect to III–As semiconductor QDs. We may expect a more significant value of the exchange splitting for exciton and biexciton states in QD of isotope-mixed crystals (see, also [31, 97]). Thanks to the large biexciton binding energy, II–VI QDs were the first, where the biexciton-exciton cascade could be traced directly in the time domain on SQD level [144]. Figure 3.15 depicts transient PL spectra (left) of both emission lines and the time-dependent intensity of the exciton and the biexciton signal (right panel). The biexciton emission shows a monoexponential decay with a time constant of 310 ps. The exciton reveals a more complex behavior: the onset of the exciton line its delayed, resulting in "plateau–like" characteristics of the exciton decay curve. The excitation density according to authors of this experiment was set to a value where an average number of two electron–hole pairs per excitation pulse in the SQD was generated. Model calculations taking into account the biexciton state, the bright and the dark exciton states and the "empty" QD (corresponding to a QD population with 2, 1 and 0 excitons, respectively), confirm that the exciton state is fed by the biexciton recombination causing the delayed onset and the "plateau–like" characteristics of the exciton emission dynamics (for details see [14] and references therein).

3.6 Electron–Phonon Interaction in Low-Dimensional Structures

One of the central themes of this chapter is how reducing the size *semiconductor* structures down to *mesoscopic* and smaller scales brings the quantum wave nature of electrons into play, resulting in electronic and optical properties which are markedly different from those of bulk structures. Many references [4, 74, 113] describe how these properties can be exploited in device applications. But one of the key challenges facing physicists and engineers is how to make devices operate at room temperature. The main obstacle to achieving this goal is the unavoidable presence of phonons, the quantum vibration of atoms (ions) making up a solid, and their ability to scatter electrons. As is well known, the room temperature mobility of 2D (1D, 0D) electron gas is limited by phonon scattering and phonons provide the principal channel of energy exchange between confined electrons and their surroundings. Over the last three decades this topic has been the focus of intensive experimental and theoretical investigation, the progress of which has been charted specifically through two series of International Conferences: Phonon Scattering in Condensed Matter and Hot Carriers in Semiconductors (see e.g. [145, 146, 147]). Although most of the basic concepts of electron–phonon interaction are the same as for 2D carrier–phonon interactions [79–88], the additional carrier confinement gives rise to some interesting differences. The most notable of these is the so-called phonon bottleneck [149, 150, 151, 152]. Reducing the dimensionality of the carrier system has the effect of reducing the phase space for carrier scattering. Corresponding to each new direction of carrier confinement a form factor arises in the electron–phonon scattering rate. This imposes a restriction on the magnitude of the momentum component in that given direction of a phonon that can be emitted or absorbed. To illustrate this effect, we consider the simple picture of an infinite rectangular confinement potential of width W. The maximum phonon wavevector component in the confinement direction is given by $q_{\max} \sim \pi / W$. Additionally, the confinement breaks up the carrier energy spectrum into a set of discrete levels (see, Fig. 3.2) $\mathrm{E}_n = \pi^2 \hbar^2 / 2m^* W^2$. We can see that, for interlevel transitions, as W is reduced the energy $\hbar\omega = \mathrm{E}_{\mathrm{N}'} - \mathrm{E}_{\mathrm{N}}$ of the emitted phonon increases as W^{-2}, while the momentum cut off increases more slowly, as W^{-1}. Since, for acoustic phonons, $\mathrm{sq} = \omega$, it becomes increasingly difficult for a phonon to be emitted or absorbed as W gets smaller. For optic phonons the momentum cut off does not present a problem, but the narrow energy dispersion means that the carrier level spacing must lie very close to the optic phonon energy for emission or absorption to take place This could have very serious consequences for carrier relaxation in QDs (for detail see below Fig. 3.17). However, in QWRs, the continuous carrier energy spectrum along the wire direction lifts the restriction a little (for details, see, also [164, 165]).

As we have indicated above, theoretical investigations [151] have found that in heterostructures. The electron–phonon scattering rate with correct phonon mode solutions taken into account does not differ significantly from the rate assuming bulk phonon modes (see, however [152]). For example, the electron–phonon scattering rate for AlAs-GaAs-AlAs QW will be somewhere in between the rates for bulk

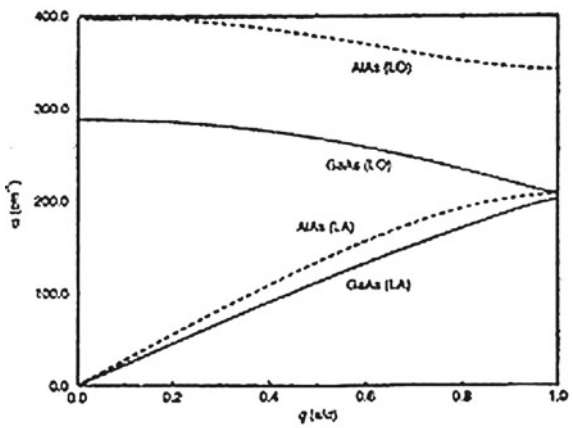

Fig. 3.16 Longitudinal [001] acoustic (*LA*) and optical (LO) phonon dispersion curves for GaAs (*solid line*) and AlAs (*dotted line*)

GaAs and AlAs phonons, approaching the rate for bulk GaAs (AlAs) phonons as the well width increases (decreases) [166]. Only in free-standing structures, when the confined electrons and phonons are both of lower dimension, are the rates expected to be qualitatively different from those assuming bulk phonons [167, 168]. In the following we shall restrict ourselves to QWs and wires embedded in a substrate and make the simplifying approximation of bulk phonons (see also [147]). The qualitative differences in the electron–phonon rates between low-dimensional and bulk semiconductors are then a consequence of the reduced dimensionality of the electron only.

At 100 K, the dominant phonon energy $3k_{\mathrm{B}}T \simeq 26\,\mathrm{meV} = 210\,\mathrm{cm}^{-1}$, that mostly acoustic phonons will be present (see Fig. 3.16). Due to this reason for the first we should consider the lower temperature range where the effect of optical phonons on electron–phonon rate can be neglected. As is well known (see, e.g. [147]), acoustic phonons give rise to a perturbing potential in two different ways. In the first, small changes in the relative positions of the atoms perturb the electrostatic potential experienced by the electrons, resulting in a change in the electron energy. In the second way, changes in the relative position of oppositely charged ions Ga and As produce an electric polarization and hence long-range electric field which again affects the electron energy. The perturbing potentials known respectively as the deformation and piezoelastic potentials (see, e.g. [100, 169]), have the following form [170]:

$$V^{\mathrm{DP}}_{\vec{q}}(\vec{r}) \approx \mathrm{C}^{\mathrm{DP}} q^{1/2} e^{-\vec{q}\,\vec{r}}\,, \tag{3.77}$$

$$V^{\mathrm{PE}}_{\vec{q}}(\vec{r}) \approx \mathrm{C}^{\mathrm{PE}} q^{1/2} e^{-\vec{q}\,\vec{r}} \tag{3.78}$$

Here C^{DP} and C^{PE} are the coupling strength constants and $\vec{q}$ is the phonon wavevector. In this relations we have neglected the screening due to reduce the electron–phonon interaction strength (see, also [171]). Below, we have also neglected

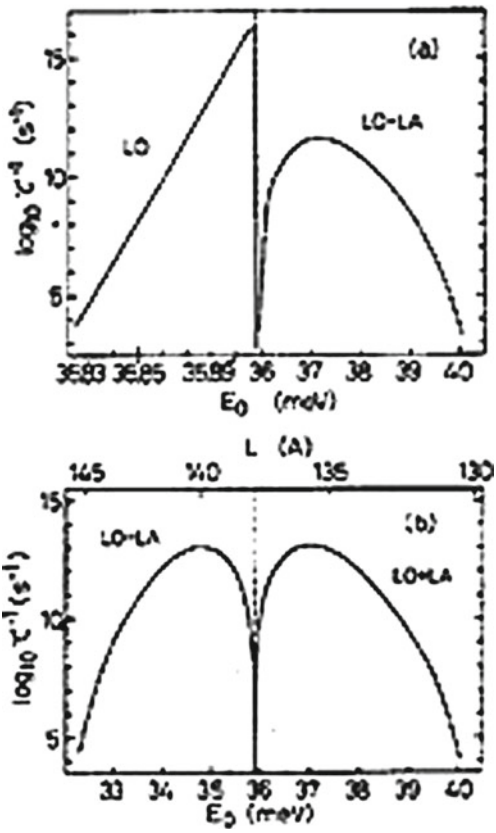

Fig. 3.17 Calculated electron relaxation rate $1/\tau$ for E_0 in the vicinity of $\hbar\omega_{LO}$. **a** T = 0 K; **b** T = 300 K. The LO peak is not shown in **b**, since it is nearly the same as in **a**, in this logarithmic scale. In **a**, the scale in abscissa is different above and below $\hbar\omega_{LO}$, which is indicated by the vertical dashed line. Dot diameter L corresponding to E_0 is shown cross the upper part (after [156])

the dependence on longitudinal/transverse mode type and have approximated the atomic lattice as an elastically isotropic continuum (see, however [164]). For the considered temperature range, the dominant phonon wavelength is much larger than the interatomic spacing, justifying our use of the continuum approximation which replaces the discrete atomic lattice vector with continuous position vector $\overrightarrow{r}$. For the perturbing potentials (3.77) and (3.78) and electron states in the case of a QW with thickness d and infinite well plane dimensions

$$\Psi_{\overrightarrow{k}}(\overrightarrow{r}) = Ce^{i(k_x x + k_y y)}\sin(\pi z/d) \tag{3.79}$$

and for QWR with width w, thickness d and infnite length along the x-direction, we have

$$\Psi_{\overrightarrow{k}}(\overrightarrow{r}) = Ce^{ik_x x}\sin(\pi y/w)\sin(\pi z/d). \tag{3.80}$$

The QW matrix elements are

$$|\langle\Psi_{k'}|\widehat{V}(q)|\Psi_k\rangle|^2 \sim (|C^{\mathrm{DP}}|^2 q + |C^{\mathrm{PE}}|^2 q^{-1}) q_{\mathrm{z}}^{-2} \left[(2\pi d)^2 - q_{\mathrm{z}}^2\right]^{-2} \sin^2(q_{\mathrm{z}} d/2)\delta_{k'_x, k_{x\pm qx}}, \delta_{k'_{y,}} \delta_{k_{y\pm q_y}} \quad (3.81)$$

and the QWR matrix elements are

$$|\langle\Psi_{k'}|\widehat{V}(q)|\Psi_k\rangle|^2 \sim (|C^{\mathrm{DP}}|^2 q + |C^{\mathrm{PE}}|^2 q^{-1}) q_{\mathrm{y}}^{-2} \left[(2\pi w)^2 - q_{\mathrm{y}}^2\right]^{-2} \sin^2(q_{\mathrm{y}} w/2) q_{\mathrm{z}}^{-2} \left[(2\pi d)^2 - q_{\mathrm{z}}^2\right]^{-2} \times \sin^2(q_{\mathrm{z}} d/2)\delta_{k', k_{\pm q}} \quad (3.82)$$

where C is a normalization constant, m^* is the effective electron mass, for wire we usually have $w > d$, and k and k' are the electron wavevectors before and after scattering, respectively. In addition to energy being conserved during a scattering event, we can see that the momentum components parallel to the QW plane and wire length are also conserved. On the other hand, the momentum components normal to the well plane and wire length are not conserved. Furthemore, the matrix elements are suppressed for normal momentum components exceeding the inverse well and wire thickness. Let us restrict ourselves to the case where the electrons and phonons are in thermal equilibrium at a common temperature T (hot electrons see [147]). Taking into account the relation between Fermi energy and areal electron density, $\mathrm{E_F} = n\pi\hbar^2/m^*$, we find that an AlAs/GaAs QW with n 5×10^{11} cm^{-2} has Fermi energy in units of temperature, $\mathrm{E_F}k_{\mathrm{B}} \simeq 200\,\mathrm{K}$, here $m* = 0.067\,\mathrm{m_0}$ for GaAs [172]. A split-gate AlAs/GaAs quantum wire with a Fermi wavector of the order $k_{\mathrm{F}} \approx \pi/w = 6\times10^9\,\mathrm{cm}^{-1}$ for width $w = 500\,\text{Å}$ has a Fermi energy $\mathrm{E_F}/k_{\mathrm{B}} \simeq 30\,\mathrm{K}$. Such numbers are represantive of those for actual structures and therefore we typically find for QWs that electron scattering is approximately elastic in the acoustic phonon dominated temperature regime, while for QWRs temperatures must be somewhat lower to have approximately elastic scattering (for details see [166]).We should add that the electron–phonon interaction due to optical modes has been reviewed in [164].

Below, we will briefly consider carrier–phonon interactions in QDs. The discussion will focus on carrier relaxation processes [156, 172] and, in particular, the predicted phonon bottleneck effects [160, 162]. In higher-dimensional, e.g. QWs [147, 164], the dominant relaxation process is longitudinal-optical (LO) phonon emission via Frölich interaction, with subpicoseconnd relaxation time. In a QD, however, this process is forbidden due to the very discrete nature of the levels, unless the separation level equals the LO phonon energy $\hbar\omega_{\mathrm{LO}}$. Inoshita and Sakaki [156] considered five (LO, LA, LO ± LA and 2LA) kinds of phonons for description of electron relaxation in a QD. According to the results of [156] a first-order contribution (LO and LA emission) was given supply by a golden rule as

$$1/\tau = \frac{2\pi}{\hbar} \sum_{\vec{q}} |M_{\vec{q}}^{\mathrm{if}}|^2 \quad |N_q + 1|\delta\left(\mathrm{E}_0 - \hbar\omega_q\right), \quad (3.83)$$

where N_q is the Bose distribution function $\frac{1}{\left(e^{\hbar\omega_q k_B T}-1\right)}$. The matrix element $M^{if}_{\vec{q}}$ can be written as

$$M^{if}_{\vec{q}} = a_{\vec{q}} \langle i | e^{i \vec{q} \vec{r}} | f \rangle \tag{3.84}$$

with

$$a_{\vec{q}} = D\sqrt{\hbar q/2\rho c\Omega} \quad \text{(LA mode)} \tag{3.85}$$

$$a_{\vec{q}} = g_f/q\sqrt{\Omega} \quad \text{(LO mode)}. \tag{3.85'}$$

Here, Ω is the system volume, the deformation potential (DP) $D = 6.8\,\text{eV}$, density $\rho = 5.36\ \text{g/cm}^3$, and the sound velocity $c = 5.15 \times 10^5$ cm/s (see, e.g. [172, 174]). The Fröhlich coupling constant $g_f = [2\pi e^2 \hbar\omega_{LO}\left(\frac{1}{\varepsilon_\infty}-\frac{1}{\varepsilon_0}\right)]$ with $\hbar\omega_{LO} = 35.9\,\text{meV}$, $\varepsilon_\infty = 10.9$ and $\varepsilon_0 = 12.9$ (GaAs QD). The mode indices to $M^{if}_{\vec{q}}$, N_q and ω_q are suppressed to avoid unnecessary complication. By converting the summation into an integral, Eq. (3.83) can be reduced to an analytic form (see, also [173]). Figure 3.17a shows the relaxation rate $1/\tau$ at $T = 0$ calculated in [156] as a function of $E_0 \simeq \hbar\omega_{LO} = 35.9\,\text{meV}$. The LO (one-phonon) contribution has a sharp peak immediately below $\hbar\omega_{LO}$. This peak decreases exponentially on the low-energy side, while it drops more steeply (but continuously) in the high energy side and vanishes for $E_0 \geqslant \hbar\omega_{LO}$. Although the peak value exceeds 10^{15}s^{-1}, a slight detunning of E_0 from peak dramatically reduces $1/\tau$. (For instance, $1/\tau$ is only $10^8\ \text{s}^{-1}$ for detunning $\Delta E_0 = -0.05\,\text{meV}$). This indicates that taking advantage of the LO process requires extremely precise tunning of E_0 to $\hbar\omega_{LO}$, for more precise than it possible with current microfabrication technology. The inclusion of the second-order LO + LA process significantly alters the situation. It gives rise to a rather broad peak on the high-energy side of $\hbar\omega_{LO}$ with a peak value exceeding $\simeq 10^{11}\ \text{s}^{-1}$. This peak value (corresponding to $\tau = 10\,\text{ps}$), of course, is much smaller than that of the one-phonon peak, but it is still large enough for our purpose of having efficient light emission. Figure 3.17b shows $1/\tau$ at $T = 300\,\text{K}$. Now it is seen that the LO–LA process, which is absent at $T = 0\,\text{K}$, gives rise to another broad peak on the low-energy side of $\hbar\omega_{LO}$. The peak structure is nearly the mirror image of the LO + LA peak with respect to $\hbar\omega_{LO}$. By comparing Figs. 3.17a, b, it is seen that the LO + LA peak is enhanced by a factor of 10^2 by the temperature increase. This reflects the enhanced Bose functions of LA phonons. In Fig. 3.17b, dot diameter L is shown across the top.

To summarize the results of [156] it should be noted that for interval spacing $E_0 > 0.2\,\text{meV}$ (or dot diameter $L > 2{,}000\,\text{Å}$), multiphonon processes are generally found to provide the dominant relaxation path, with exception of the narrow energy range $\hbar\omega_{LO} - 0.3\,\text{meV} < E_0 < \hbar\omega_{LO}$. This range is so narrow that it would be hopelessly difficult to tune the interval spacing to this energy. An alternative and more realistic way to achieve rapid relaxation is the use of the LO ± LA processes, which are in a wider range of E_0 near $\hbar\omega_{LO}$. In this paper [156] was shown that the relaxation time $< 1\,\text{ns}$ can be achieved for E_0 within the window $|E_0 - \hbar\omega_{LO}| < 3\,\text{meV}$ (at 300 K). This suggest that efficient PL and lasing from a QD will be possible if a dot can be

designed to have a nearly harmonic (equal-spaced) level structure, where the level spacings fall into the above indicated window (see, also [160, 162]).

3.7 Exciton–Phonon Interaction in Low-Dimensional Structures

In this present paragraph we aim to give an introduction rather than a comprehensive review of all properties of *2D*, *1D*, *and 0D excitons* and *exciton-phonon interactions* (see for example [15, 123, 151, 152 159, 175, 176]). The exciton envelope function in a state of QW with wavevector $\overrightarrow{k}$ can be written as [15]:

$$\Psi_k\left(\overrightarrow{r_e}, \overrightarrow{r_h}\right) = \exp\left(i\,\overrightarrow{k}\,\overrightarrow{R_\parallel}\right) F(\rho)\,\varphi_e(z_e)\,\varphi_h(z_h), \tag{3.86}$$

where $\overrightarrow{r_e}$, $\overrightarrow{r_h}$ are the electron and hole positions, $\overrightarrow{R_\parallel}$ is the position of the exciton center of mass, $\rho = \left(\overrightarrow{r_e} - \overrightarrow{r_h}\right)_\parallel$ where $\parallel$ indicates the vector component in the QW plane, F(ρ) is a function describing the relative electron–hole motion [115], z is the growth direction of the structure, and $\varphi_e(z_e)$ and $\varphi_h(z_h)$ are the electron and hole wave functions for the first size-quantized level. In the simple variational approach (see also [15, 16])

$$F(\rho) = \sqrt{\frac{2}{\pi a_B^2}} \exp\left(-\frac{\rho}{a_B}\right) \tag{3.87}$$

In the last relation a_0 is the *Bohr exciton radius*. In 10 nm GaAs/$Al_{0.4}Ga_{0.6}As$ QWs, a_B has a value of 12 nm and increases to 15 nm in 20 nm QWs [177]. Below, Eqs. (3.86) and (3.87) are used in analysis of the exciton–phonon interaction. In reality the 2D exciton spectrum is much more complicated than suggested by these expression and includes excited exciton states (see [15, 123, 175]).

The main experimental method used to study 2D excitons is optical spectroscopy, in particular, PL and photoluminescence excitation (PLE) techniques. Optical transitions involving exciton states in QWs are governed by selection rules [15]. For example, the requirement that momentum is conserved in interactions between photons and excitons leads to the important conclusion that only excitons with $k \simeq 0$ are optically active. The result of this is that an optical spectrum usually consists of narrow lines at the energies corresponding to the minima of the exciton bands. We should indicate the absence of polariton effects in single QWs. The polariton effects, which are commonly seen in 3D exciton spectra (see, e.g. [82, 115, 178]), are due to the strong exciton–photon interaction and are important when the wavelength of the coupled exciton-photon interaction (polariton [18]) is bigger than the thickness of the medium in which the polariton is propagating. In the 2D case the thickness of a QW is so small that polariton effects may be neglected.

Typical exciton PL and PLE data for a range of thin layers of GaAs between thicker AlGaAs layers is shown in Fig. 3.18. An increase in phonon density induces

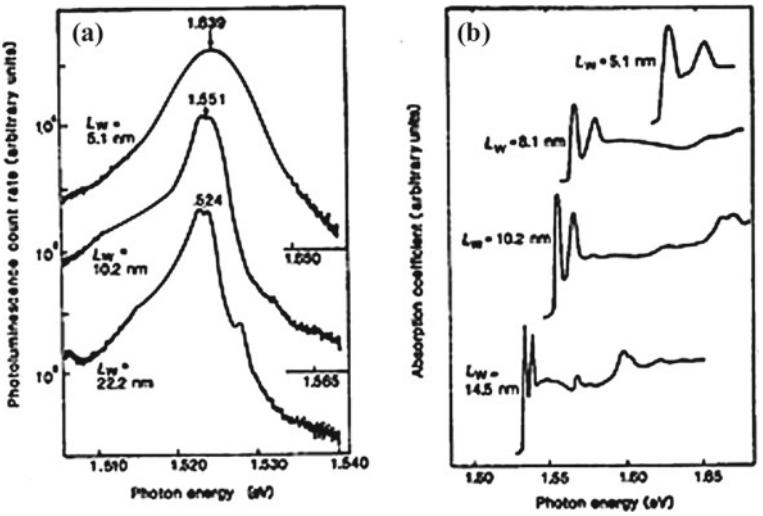

Fig. 3.18 **a** PL spectra for wells of different thickness and **b** the PLE spectra from GaAs QWs (after [16])

an increase in the population of excited exciton states and can also lead to quenching of the PL in narrow QWs [16]. Phonons also affect the transport properties of excitons, particularly at elevated temperatures when the exciton-phonon scattering rate becomes greater than the scattering rate due to impurities and defects [115]. The basic approach used in analyzing the 2D exciton-phonon interaction is similar to that used for electrons and holes [147]. The main differences arise from the next facts:

(1) excitons are Bose particles so that Bose–Einstein or frequently Boltzman statistics are used to describe their equilibrium distribution;
(2) since their density is usually low ($n_{ex} < 10^{10}$ cm^{-2}) therefore it does not take into account exciton–exciton interaction;
(3) excitons have a finite lifetime;
(4) exciton interaction with optical phonons results in both scattering and in their dissociation into uncoupled electron–hole pairs.

The two mechanisms responsible for the *exciton–phonon interaction* are those responsible for acoustic phonon interaction with free carriers: DP and piezoelectric (PE) coupling. However, the Hamiltonian for exciton-phonon interaction with both electrons and holes, and for excitons in GaAs, this increases the matrix element for DP coupling but decreases it to PE coupling in comparison with the corresponding values for free carriers. Below, we limit the discussion to a basic treatment of the exciton–phonon DP coupling and refer the reader to the references [15, 176–178] for further details of the interaction. The probability of exciton-phonon transitions taking place within a volume V is given by Fermi's golden rule (see also [82]):

$$W_{\overrightarrow{k}\rightarrow\overrightarrow{k'}} = \frac{2\pi}{\hbar}\sum_{\overrightarrow{q},j}|M^{\overrightarrow{q},j}_{\overrightarrow{k}\longrightarrow\overrightarrow{k'}}|^2|N_{\overrightarrow{q},j}+\frac{1\pm 1}{2}| \times \delta\left(\mathrm{E}_{\overrightarrow{k'}}-\mathrm{E}_{\overrightarrow{k}}\pm\hbar\omega\left(\overrightarrow{q},j\right)\right), \tag{3.88}$$

where $\mathrm{M}^{\overrightarrow{q},j}_{\overrightarrow{k}\longrightarrow\overrightarrow{k'}}$ is the matrix element of the $\overrightarrow{k}\longrightarrow\overrightarrow{k'}$ transition involving emission (+) or absorption (−) of an acoustic phonon with polarization j = LA, TA wavevector $\overrightarrow{q}$, and frequency $\omega\left(\overrightarrow{q},j\right)=s_j\overrightarrow{q}$, s_j is the sound velocity, and $N_{\overrightarrow{q},j}$ are the phonon occupation numbers which, in equilibrium, are given by the Bose–Einstein distribution:

$$N_{\overrightarrow{q},j}=\left[\exp\left(\frac{\hbar\omega}{k_{\mathrm{B}}T_0}\right)-1\right]^{-1}, \tag{3.89}$$

where T_0 is the lattice temperature. The DP interaction Hamiltonian for creation (annihilation) of an acoustic phonon of wavevector $\overrightarrow{q}$ and mode j can be written as

$$H^{\mathrm{DP}}_{\text{ex-ph}}=H^{\mathrm{DP}}_{\text{e-ph}}+H^{\mathrm{DP}}_{\text{h}-\text{ph}}=\sqrt{\frac{\hbar}{2\rho_0\Omega s_{jq}}}iq[\Xi_{\mathrm{e}}\exp\left(\pm i\overrightarrow{q}\,\overrightarrow{r_{\mathrm{e}}}\right)+\Xi_{\mathrm{h}}\exp\left(\pm i\overrightarrow{q}\,\overrightarrow{r_{\mathrm{h}}}\right)], \tag{3.90}$$

where Ξ_{e}, Ξ_{h} are the electron and hole DP constants, ρ_0 is the material density, Ω is the volume, and we note that DP Hamiltonian for holes is anisotropic

$$H^{\mathrm{DP}}_{\text{h-ph}}=\left(a+\frac{b}{2}\right)(u_{xx}+u_{yy})+(a-b)u_{zz}, \tag{3.91}$$

where a and b are constants and the diagonal components of the deformation tensor are:

$$u_{\alpha\alpha}=\sqrt{\frac{\hbar}{2\rho_0\Omega s_{jq}}}i\overrightarrow{e_\alpha}\left(\overrightarrow{q},j\right)q_\alpha\exp\left(\pm\overrightarrow{q}\,\overrightarrow{r_{\mathrm{h}}}\right), \tag{3.92}$$

where $\overrightarrow{e}^{\left(\overrightarrow{q},j\right)}$ is the polarization unit vector. The matrix element can be calculated using the exciton wave functions given in (3.86)

$$M^{\overrightarrow{q},j}_{\overrightarrow{k}\longrightarrow\overrightarrow{k'}}=\langle\Psi_{\overrightarrow{k}}|H_{\mathrm{ex}-\mathrm{ph}}|\Psi_{\overrightarrow{k'}}\rangle \tag{3.93}$$

and substituting into (3.88) we obtain the expression for the transition probability

$$W_{\overrightarrow{k}\rightarrow\overrightarrow{k'}}=\frac{\Xi^2\left(\overrightarrow{q}\right)}{\hbar\rho_0 S_0 s_j^2}\left(N_{s_j,q}+\frac{1\pm 1}{2}\right)\frac{q^2}{q_z}\theta\left(q-q_\parallel\right), \tag{3.94}$$

here energy and momentum conservation require

$$q = \frac{\hbar}{2m^*}|k^2 - k'^2|; \quad q_\parallel = |\overrightarrow{k} - \overrightarrow{k'}|; q_z = \sqrt{q^2 - q_\parallel^2} \tag{3.95}$$

and S_0 is the simple area. $\theta\,(x)$ is the Heaviside step-function

$$\theta\,(\mathrm{x}) = \begin{pmatrix} 1 & \mathrm{x} \geqslant 0 \\ 0 & \mathrm{x} < 0 \end{pmatrix}. \tag{3.96}$$

If we use the approximation the *QW barriers* are infinitely high, the form factors have the form

$$z_\mathrm{e}\,(q_z) = z_\mathrm{h}\,(q_\mathrm{h}) = \frac{\sin\,(q_z w/2)}{(q_z w/2)\,[1-(q_z w/2\pi)^2\,]}, \tag{3.97}$$

where as before w is the QW width (for details, see [177, 178]).

In polar semiconductors like GaAs, excitons are coupled to optic phonons [172, 174] through the Fröhlich interaction [115, 116] and the resulting matrix elements are approximately greater than those for acoustic phonons. However, because of their high energy ($\hbar\omega_\mathrm{LO} = 33.9\,\mathrm{meV}$, see above), the role of optic phonons in exciton dynamics is relatively unimportant at low temperatures, since the exciton binding energy $\mathrm{E_B} \ll \hbar\omega_\mathrm{LO}$ (for GaAs [172]), very few excitons exist at high temperatures ($k_\mathrm{B}T \gtrsim \hbar\omega_\mathrm{LO}$) where the optic phonon population is much greater. But there is an interval of intermediate temperatures ($100\,\mathrm{K} < T < 200\,\mathrm{K}$) in which excitons can still be observed in GaAs QWs and the population of optic phonons is sufficient to influence their dynamics [177, 178].

The influence of optic phonons on the *luminescence* linewidths of GaAs QWs was studied by Lee et al. [178] both experimentally and theoretically. Because the optical phonon energy, $\hbar\omega_\mathrm{LO}$, is larger than the binding energy of an exciton $\mathrm{E_B}(L)$, after collision of an exciton with an optical phonon, the exciton either ionized or the optical phonon energy is transferred into kinetic energy of the center of mass with elevation of the exciton to an excited state. In the former case, for the phonon absorption, these authors obtained for the transition rate:

$$W_+(0) = \left(\frac{(32\mathrm{e}^2\omega_0\beta^4 m_\mathrm{e} N_q)}{(\pi\hbar^2 L^2)}\right)\left[\frac{1}{\varepsilon_\infty} - \frac{1}{\varepsilon_0}\right]\int_0^{\mathrm{K_{max}}} \mathrm{d}k_\mathrm{h} k_\mathrm{h} \int_0^{2\pi} \mathrm{d}\theta\, I\,(k, q)$$
$$\times\left[\left(4k_\mathrm{h}^2 + \beta^2\right)^{-3/2} - \left(4k_0^2 + \beta^2\right)^{-3/2}\right]^2 \tag{3.98}$$

with

$$K_0 = \left[\frac{2m_\mathrm{e}}{\hbar^2}\right]^{1/2}\left[-\mathrm{E_{ex}} + \hbar\omega_\mathrm{LO} - \frac{\hbar^2 k_\mathrm{h}^2}{2m_\mathrm{h}}\right]^{1/2}, \tag{3.99}$$

$$K_\mathrm{max} = \left[\frac{2m_\mathrm{e}}{\hbar^2}\right]^{1/2}[-\mathrm{E_{ex}} + \hbar\omega_\mathrm{LO}]^{1/2}, \tag{3.100}$$

$$q^2 = k_\mathrm{h} + k_0 + 2k_0 K_\mathrm{h} \cos\theta, \tag{3.101}$$

where N_q is optical phonon population, ε_∞ (ε_0) is the high-frequency (static) dielectric constant, k_h is the wavevector for the free hole, and $\mathrm{I}(k, q)$ has been defined in following relation

$$I(k,q) = \frac{\pi}{2q^2(k^2+q)^2}\left[\frac{\left(2k^2+3q^2\right)\pi}{k} - \frac{k^4\left(1-e^{-2\pi q/k}\right)}{q\left(k^2+q^2\right)}\right]. \tag{3.102}$$

In the latter case, the *exciton* is in an excited state and the center of mass moving after the phonon energy has been absorbed. Their calculations show that heavy hole excitons the contribution to the PL width from optical phonons becomes equal to that from acoustic phonons at $T = 200\,\mathrm{K}$. For light hole excitons this happens at even higher temperature. The effect of optic phonons on the exciton diffusion was analyzed by Hillmer et al. [179] who showed that it was greatest in wide QWs. Thus in 15 nm QWs the exciton mobility from optic phonon scattering becomes equal to that from acoustic phonon scattering at $T \approx 150\,\mathrm{K}$, while in 4 nm QWs this does not happen until $T \approx 200\,\mathrm{K}$. So quantum confinement produces a relative decrease in optic phonon scattering, or, in other words, acoustic phonons are more dominant in exciton scattering in QWs than in bulk material.

Optic phonons can, however, play an important role in the relaxation of hot excitons at all temperatures. Peaks are often seen in excitation spectra of exciton luminescence of photon energies equal to $E(k=0) + n\,\hbar\omega_\mathrm{LO}$ [82], where $E(k=0)$ is the energy at the bottom of the exciton band and n is an integer. This indicates the formation of hot excitons with kinetic energy much larger than $\mathrm{E_B}$ (up to 10 times [82]) which relax rapidly by emitting LO phonons and this relaxation process essentially determines the lifetime of hot excitons [180]. The creation of hot excitons and their relaxation by LO phonon emission in confined structure was first demonstrated in II–VI QWs (see, e.g. [180] and references therein), but has not been seen in GaAs QWs (see, also [181, 182]).

The QD structure has been developed and investigated in the last 2 decades [111–113]. There is great interest in this development because there is the goal of fabricating useful and reasonable include emission under low-threshold and under high-temperature operation compared to that of a QW heterostructure laser (see, also [183, 184, 186, 187]). Below we briefly consider three effects in QDs:

(1) As was shown above, the phonon bottleneck is an extremely debated issue in QDs research. The relaxation between the discrete states of QDs as well as between different exciton states in QD [189] will be slower than in QW, because the coupling of phonons is expected to be less efficient in a QD;
(2) Exciton relaxation in QDs, which is crucial for high speed devices performance [157];
(3) Nitride material systems which include AlN, GaN, InN and their alloys are widely used as light-emitting diodes (LEDs), laser diodes (LDs) and high-electron-mobility transistors (see e.g. [190, 191]).

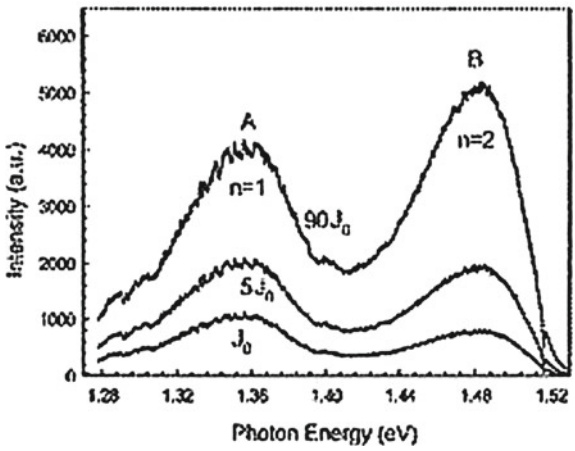

Fig. 3.19 PL spectrum of InAs/GaInP with varying excitation energy (after [189])

Sakaki et al. [156] have reported the exciton dynamics (see, however [48, 49, 50]) in InAs/GaInP self-assembled QDs, grown by MBE technique, where the electron and hole are confined strongly. Due to the large band-gap in the barrier layer, the thermal escape of carriers from QDS to the wetting layer and to the matrix is prevented, which allows this sample to PL at room temperature. The PL spectra for the studied sample in paper [189] are shown in Fig. 3.19. The excitation energy is 1.590 eV (780 nm) and the temperature is 5 K. At the maximum intensity of $90J_0$, where $J_0 = 10\,\mathrm{nJ/cm^2}$, the two peaks, labeled A and B, are at 1.362 and 1.484 eV, respectively. At a low intensity of J_0 to $5J_0$, the peak A is larger than B, however as the intensity becomes stronger, the peak B dominates the entire spectra. This shows that when relatively few carriers are excited with an excitation intensity of J_0, these carriers are in the discrete energy level (A). As the intensity of excitation beam is increased, the carries are distributed over two exciton levels. From here on, the authors of [189] have referred to the A peak, which is the lowest exciton level, as $n = 1$, and the B peak as $n = 2$ or the second-lowest exciton state. The time-resolved PL of the $n = 1$ and 2 exciton levels show a difference in their temporal evolution. Specifically, the rise time for the $n = 1$ data is ∼500 ps, slower than that of $n = 2$. According to the results of [189] there is a physical phenomenon that affects the relaxation probability that occurs between the exciton levels $n = 1$ and 2. The temperature dependence (5–200 K) of the time progression is shown that there is involvement of phonons that affect the relaxation process. The obtained results allowed by authors of [189] concluded that there is the phonon bottleneck in InAs/GaInP QDs between $n = 1$ and 2 exciton states.

Heitz et al. have reported the optical studies of relaxation process in *self-organized* InAs/GaAs QDs, which were grown by the *MBE* method (see, also [192]). The results of PLE obtained in [157] are depicted in Fig. 3.20. The solid line in Fig. 3.20a presents the excitation spectrum detected at the maximum (1.11 eV) of the QD luminescence revealing excitation via absorption in the InAs WL and the GaAs barrier. Figure 3.20b

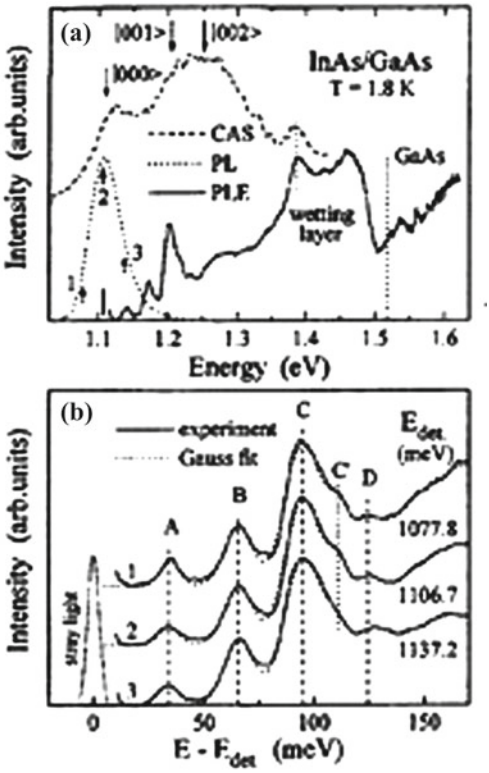

Fig. 3.20 **a** Luminescence (excited at 1.959 eV), CAS (calorimetrically absorption spectrum) and PLE (detected at the luminescence maximum) spectra of the QD structure; **b** excitation spectra of different parts of the QD luminescence [indicated by *arrows* in **a**] given with respect to the detection energy (after [157])

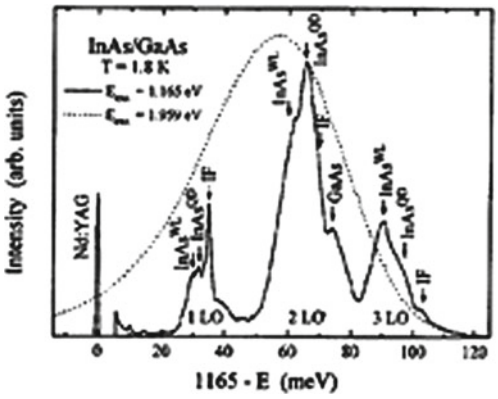

Fig. 3.21 Luminescence spectra of the QD structure excited selectively at 1.165 eV (*solid line*) and via the GaAs barrier (*dotted line*) (after [157])

compares PLE spectra recorded for different QD luminescence energies (indicated by arrows in Fig. 3.20a) displayed with respect to the detection energy.

The shape of the excitation spectra is almost independent of the detection energy showing only slight variations in the relative intensities of lines A–D. The ladder

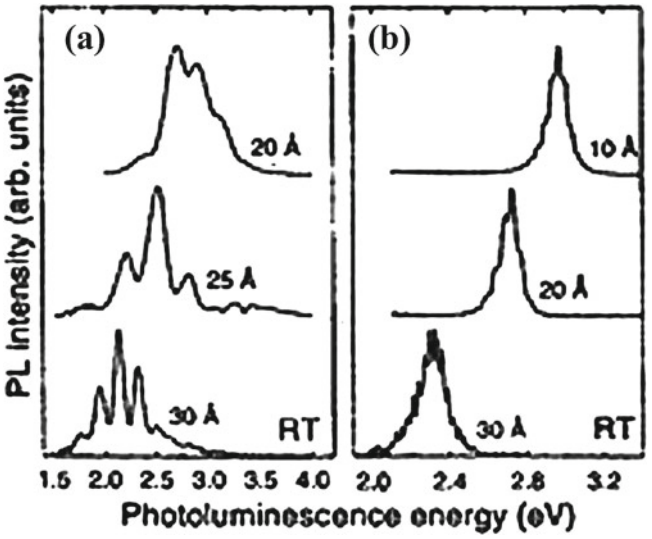

Fig. 3.22 Room temperature PL spectra of: **a** GaN QDs in AlN matrix grown on Si (111) substrate, and **b** $Ga_{0.8}In_{0.2}N$ QDs in GaN matrix grown on sapphire substrate (the 2D equivalent thickness of the QD layer corresponding to each sample is indicated) (after [190])

A–D not being equidistant is attributed to the finite experimental resolution of only 6 meV in the PLE measurement. Figure 3.21 shows a better-resolved luminescence spectrum excited selectively at the high energy onset of the QD luminescence using a Nd:YAG laser (solid line) decomposes into three bands in the energy range of 1, 2, and 3LO phonon replica, respectively. Four different phonon modes with energies of 29.6 meV ($InAs_{WL}$), 31.9 (InA_{QD}), 35.0 (IP) and 36.6 meV (GaAs) account for the fine structure that is not resolved in PLE spectra. In strained nanostructures, the InAs LO phonon energy of 29.9 meV is altered by both strain and phonon confinement [145]. Both effects, according to [157] almost perfectly compensate for each other. Thus, the phonon mode with an energy of 29.6 meV is attributed to InAs WL ($InAs_{WL}$). For the 3D InAs QDs, the energy shift due to phonon confinement can be neglected. They calculated QD LO phonon energy 32.1 meV that is in excellent agreement with $InAs_{QD}$ mode energy of 31.9 meV determined from Fig. 3.21. The mode interface (IF) with an energy of 35.0 meV is tentatively assigned to an interface phonon in the QD structure. The obtained results in [157] allow the authors to conclude that scattering of LO phonons from different regions of the QD structure due to the extended QD wave functions, together with acoustical phonon broadening, circumvents the phonon bottleneck [160, 162] effect, thus allowing exciton relaxation and carrier capture necessary for device performance.

The room temperature PL spectra corresponding to GaN and GaInN QDs of different sizes are displayed in Fig. 3.22. As can be seen, the PL energy is red shifted when the QD size increases. The important point to note is that for each kind of QDs, the PL is in the visible spectrum range. This could be quite surprising

for GaN material for which the band-gap corresponds to ultra-violet luminescence. In fact, the very large built-in electrical field in GaN/AlN structures strongly decreases the transition energy. For GaN QDs in AlN matrix a 5.5 MV/cm electrical field has been experimental determined [190]. This very high value of the internal electrical field leads to transition energies in GaN QDs comparable with those in GaInN QDs, although the GaInN band-gap (2.7 eV for 20% In-content) is much lower than the GaN one (3.4 eV). This is a proof of the major influence of the electrical field on the optical transitions in group III-nitride materials. The comparison with QW equivalent structures indicates that QDs have higher luminescence efficiency. Moreover, the wavelength emission of QDs can be tuned from blue to orange simply by varying QD size. These results open a new route for the fabrication of efficient visible high-emitting devices.

Chapter 4
Applications of Low-Dimensional Structures

The knowledge gained in the previous discussion makes it possible to consider and analyze a variety of different *nanostructure* devices. In this chapter as a first step we consider electronic and optical devices. Some of these mimic well-known microelectronic devices but with small dimensional scales. This approach of applications to devices with shorter response times and higher operational frequencies that operate at lower working currents, dissipate less power, and exhibit other useful properties and enhanced characteristics. Such examples include, in the first step, the field effect transistors considered below. On the other hand, new generations of the devices are based on new physical principles, which cannot be realized in microscale devices. Among these novel devices are the resonant-tunneling devices described in the following section, and single-electron-transistor as well as optoelectronic devices (light-emitting diodes and lasers).

4.1 Resonant Tunneling Diodes

As shown above electrons in *heterojunctions* and in *QWs* can respond with very high mobility to applied electric fields parallel to the interfaces (see, also [74]). In this paragraph, the response to an electrical field perpendicular to the potential barriers at the interfaces will be considered. Under certain circumstances, electrons can tunnel through these potential barriers, constituting the so-called perpendicular transport (see, also [164, 165]). Tunneling currents through heterostructures can show zones of *negative differential resistance* (*NDR*) (see, Fig. 4.1), which arise when the current level decreases for increasing voltage (see, also [4]). The operation of NDR QW electronic devices is based on the so-called resonant tunnel effect (RTE), which takes place when the current travels through a structure formed by two thin barriers with a QW between them. The I–V characteristics of RTE devices are depicted in Fig. 4.1. This figure also shows the representation of the conduction band of a double heterojunction with a QW between the junctions. The thickness of the QW

V. G. Plekhanov, *Isotope Low-Dimensional Structures*, SpringerBriefs in Physics,
DOI: 10.1007/978-3-642-28613-1_4, © The Author(s) 2012

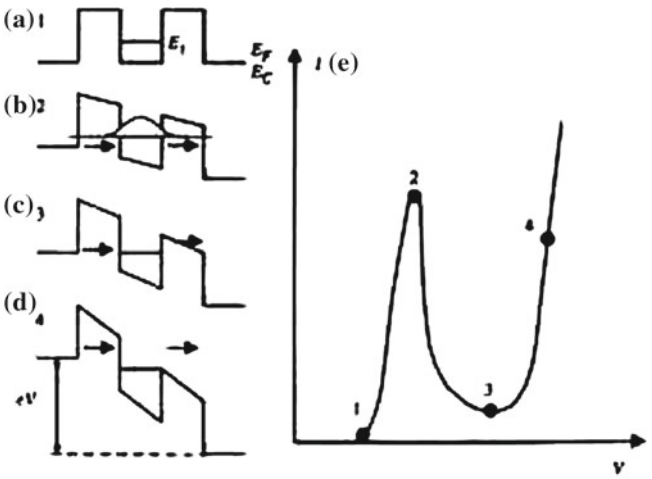

Fig. 4.1 Schematic representation of the conduction band of a resonant tunnel diode: **a** with no voltage, **b–d** for increasing applied voltage, **c** current–voltage characteristic

is supposed to be small enough (5–10 nm) as to have only one allowed energy level E_1 (resonant level). The well region is made from lightly doped GaAs surrounded by higher gap AlGaAs (see, e.g. [1, 106]). The outer layers are made from heavily doped n-type GaAs (n^+ GaAs) to facilitate the electrical contacts. The Fermi level of the n^+ GaAs is represented within the conduction band, since it can be considered a degenerated semiconductor [120].

Let us suppose that an external voltage, V, is applied, starting from 0 V. It can be expected that some electrons tunnel from the n^+ GaAs conduction band through the potential barrier, thus resulting in increasing current for increasing voltage (region 1–2 in the I–V curve of Fig. 4.1c). When the voltage increases, the electron energy in n^+ GaAs increases until the value $2E_1/e$ is reached, for which the energy of the electrons located in the neighborhood of the Fermi level coincides with that of level E_1 of the electrons in the well (see, Fig. 4.1b). In this case, resonance occurs and the coefficient of quantum transmission through the barriers rises very sharply. In effect, when the resonant condition is reached, the electron wave corresponding to the electrons in the well is coherently (see, e.g. Fig. 10.18 in [74]) reflected between two barriers. In this case, the electron wave incident from the left excites the resonant level of the electron in the well, thus increasing the transmission coefficient (and thus the current through the potential barrier (region 2 in Fig. 4.1c). If the voltage further increased (region 2–3), the resonant energy level of the well is located below the cathode lead Fermi level and the current decreases, thus leading to the so-called negative differential resistance (NDR) region (region 2–3 of Fig. 4.1). Finally, for even higher applied voltage, Fig. 4.1d, the current again rises due to the thermo-ionic emission over the barrier (region 4). RTD used in microwave applications are based on this effect. A figure of merit used for RTD is the peak-to-valley current ratio of their I–V characteristic, given by the ratio between the maximum current (point 2)

and the minimum current in the valley (point 3). Although the normal values of the figure of merit are about five for AlGaAs–GaAs structures at room temperature, values up to ten can be reached in devices fabricated from strained InAs layers, surrounded by AlAs barriers and operating at liquid nitrogen temperature [4]. If RTD are simulated by a negative resistance in parallel with a diode capacitance C and a series resistance R_S, as is the case of normal diodes, it is relatively easy to demonstrate that the maximum operation frequency increases as C decreases. The resonant tunnel diode is fabricated from relatively low-doped semiconductors, which results in wide depletion regions between the barriers and the collector region, and accordingly, small equivalent capacity. For this reason, *RTDs* can operate at frequencies up to several THz, much higher than those corresponding earlier tunnel diodes which just reach about 100 GHz, with response time under 10^{-13}s. Small values of the NDR, i.e., an abrupt fall after the maximum on the I–V curve result in high cut-off frequencies of operation. In fact, RTDs are the only purely electronic devices that can operate up to frequencies close to 1 THz, the highest of any electron transit time device (see, also [193]).

4.2 Field Effect Transistors

The previously analyzed diodes are the simplest electronic devices, for which the current is controlled by the diode bias and vice versa. A useful function can be performed mainly due to nonlinearity of current-voltage dependences. In contrast, in three-terminal devices known as transistors there exist the possibility of controlling the current through two electrodes by varying the voltage or the current through the third electrode. Below, we briefly describe the *field effect transistors* (*FETs*) on the base of the nanowires. Nanowire FETs can be configurated by depositing the nanomaterial onto an insulating substrate surface, and making source and drain on the nanowire ends. Figure 4.2 illustrates this approach. There, we show a schematic diagram of a Si-nanowire FET with the nanowire, the metal source and drain electrodes on the surface of the SiO_2/Si substrate (see, also [103]). This approach may serve as the basis for hybrid electronic systems consisting of nanoscale building blocks integrated with more complex planar silicon circuitry [4]. We should note that an extremely small FET may be built on the basis of carbon nanotube [194]. In conclusion, we have noted that the nanowire devices discussed here have great potential for applications in nano and optoelectronics.

4.3 Single-Electron-Transistor

The so-called single electronics [106–110] that appeared in the late 1980s, is at present a tremendously expanded research field covering future digital and analog circuits, metrological standards, sensors, and quantum information processing and

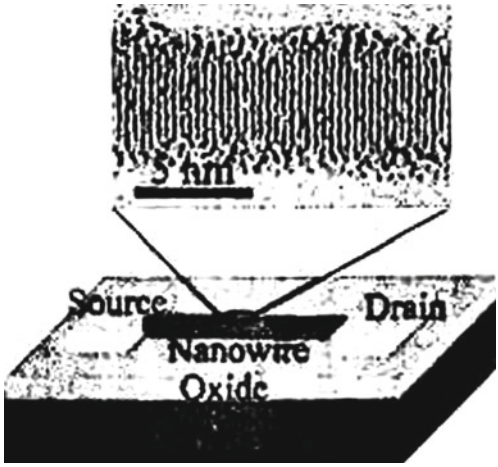

Fig. 4.2 A schematic diagram of a Si-FET with nanowire, the metal source, and drain electrodes on the surface of a SiO_2/Si substrate (after [103])

transfer [4]. The basic device, called a *single electron device* (*SED*), literally enables the control of electrons on the level of an elementary charge (see, also [103, 193]). There are rich varieties of SEDs (see, e.g. [195–197]), but the operation principle of all SEDs is basically the same. SEDs rely on a phenomenon that occurs when electrons are to enter a tiny conducting material. When the tiny conducting material, or metallic "island", is extremely small, the electrostatic potential of the island significantly increases even when only one electron enters it. For example, for a nanometer scale island having a capacitance C of, say, 1 aF (10^{-18} F), the increase in the voltage, which is e/C with $e = 1.6 \times 10^{-19}$ C, reaches 160 mV. This is much larger than the thermale noise voltage at room temperature, 25.9 mV. Coulomb repulsion prevents additional electrons from entering the island unless the island potential is intentional lowered by an external bias. If the island potential is lowered gradually, the other electrons can enter the island one by one with negligibly small power dissipation (for details see [196] and references therein).

The *single-electron transistor* works as follows. The electron transfer is determined by two factors: the Coulomb charging of the dot and the quantized energy levels in the dot (see above). If the drain is biased with respect to the source, an electric current occurs in the regime of single-electron transfer. By applying the voltage to the gate and changing the QD parameters, one can change the conditions of electron tunneling and affect the source-drain current. Examples of modulation of the conductance in single-electron transistors by the gate voltage are presented in Figs. 4.3, 4.4. The devices have almost the same geometry. Their dimensions are large enough to have a number of quantized levels. In Fig. 4.4 each peak in the conductance corresponds to transfer of one electron, when an energy level enters into resonance with the electron states in the contacts. Although the conductance versus gate-voltage dependences are different, i.e., not reproducible, the peak spacing is the same for both devices. It is determined by the change in the gate voltage required to change the charging energy of the *QDs* by one electron. Figure 4.4 shows clearly that

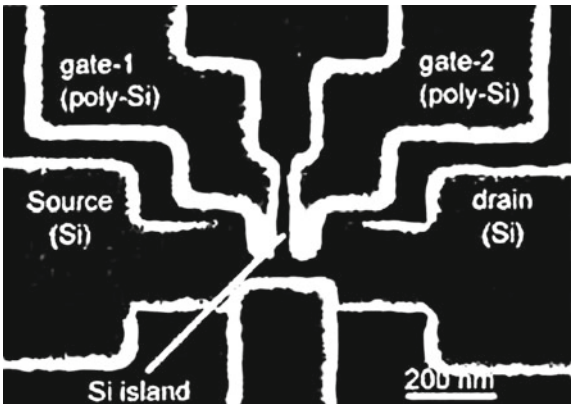

Fig. 4.3 A scanning electron microscope image of a single electron transistor (after [197])

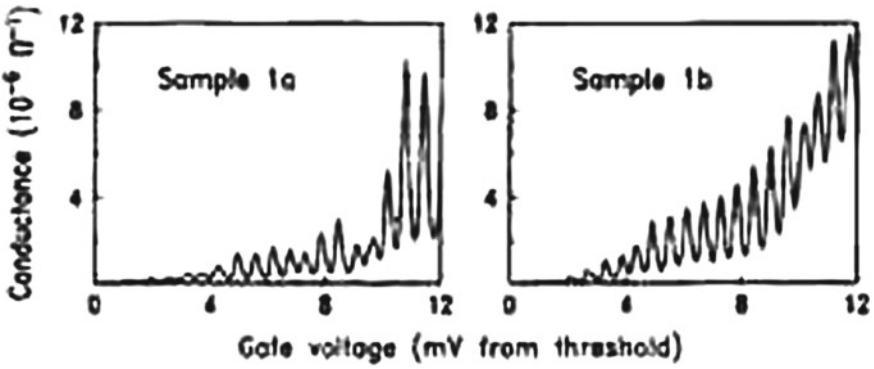

Fig. 4.4 Conductance as a function of V_g for two samples with the same geometry (after [195])

the electric current is modulated significantly by the gate voltage. Thus, for transistors with single-electron transport, strong control of very small electric current may be possible.

4.4 Light-Emitting Diodes and Lasers

So far we have studied electronic *nanoscale* devices, i.e., a class of devices that exploits electrical properties of nanostructures and operates with electric input and output signals. Another class is composed of optoelectronic devices, which are based on both electrical and optical properties of materials and work with optical and electric signals. In this paragraph we will analyze two very important classes of optoelectronic devices: light-emitting diodes and lasers (diodes as well as *photodetectors*).

As will be shown below, the energy of the electric current flowing through these diodes is transformed into light energy. These optoelectronic devices have a huge number of applications and deserve consideration in detail (see, also [183–188]).

Although stimulated emission [16] from the injection laser diode is very important (see, below), practically, sub-threshold operation of the diode—when only spontaneous light is emitted—is in many cases advantageous and has a number of applications. Diodes operating with spontaneous light emission are called light-emitting diodes [186]. The important characteristic of the *light-emitting diode* is the spectral distribution of emission The spectrum of emission is determined, primarily, by the electron/hole distributions. Thus, the ambient temperature T, defines both spectral maximum and the spectral width of emission. The peak value of the spectral distribution can be estimated as [1,74]

$$\hbar\omega = \mathrm{E}_g + \frac{k_\mathrm{B}T}{2}. \tag{4.1}$$

The full width at half maximum of the distribution is $\Delta\omega \approx 2k_\mathrm{B}T/\hbar$ and is independent of ω. In terms of the wavelength, λ, we obtain

$$\Delta\lambda = \lambda_m^2/(2\pi c)\,\Delta\omega$$

or

$$\Delta\lambda = 1.45\lambda^2 k_\mathrm{B}T, \tag{4.2}$$

where λ_m corresponds to the maximum of the spectral distribution, $\Delta\lambda$ and λ_m are expressed in micrometers, and $k_\mathrm{B}T$ is expressed in eV. Figure 4.5 shows the spectral density as a function of the wavelength for light-emitting diodes based on various materials. For these different materials, the spectral linewidth increases in proportion to λ^2, in accordance with Eq. (4.2). From Fig. 4.5, one can see that light-emitting diodes cover a wide spectral region from the infrared—about 8 μm for INGaAsP alloys—to the near ultraviolet −0.4 μm for GaN. Light-emitting diodes are, indeed very universal light sources [14].

Semiconductor lasers incorporating low-dimensional heterostructures, QWs and QDs, are attracting considerable interest their potential for improved performance over QW lasers (see, e.g. [186–188]). This prediction is based, in the single-particle picture, on the sharper density of states resulting from the confinement of the charge carriers in two or three directions. Among other advantages, the ideal QD and QWr lasers would exhibit higher and narrower gain spectrum, low threshold currents, better stability with temperature, lower diffusion of carriers to the device surfaces, and a narrower emission line than double heterostructure or *QW* lasers (see, also [199]). The observation of lasing from excitons in optically excited V-groove GaAs/AlGaAs *QWr* laser structures was described in detail [200]. The observable emission is attributed to the recombinations of excitons associated with the lowest energy electron- and hole-subbbands of the QWr. Moreover, these authors show that the emission energy remains nearly constant within the inhomogeneously broadened photoluminescence

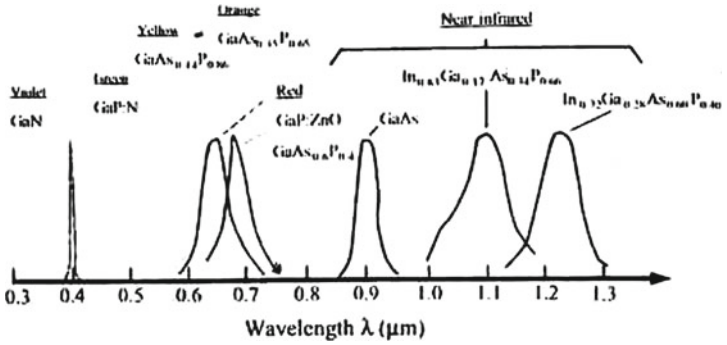

Fig. 4.5 The spectra of light-emitting semiconductor diodes with different bandgaps (after [201])

line of the QWrs for both continuous wave (cW) and pulsed optical excitation over a wide range of power densities. These results corroborate the important role played by electron-hole Coulomb correlations [133] in the optical emission from quasi-1D QWrs in the density regime of the Mott transition.

Optical emissions of the QWr laser structure are displayed in Fig. 4.6 for different values of the optical power density below, at and above the threshold for lasing in the QWr. Upon increasing the pump power, these authors observe a nearly constant energy of the peak at 1.581 eV that corresponds to the optical transition e_1–h_1 associated with the ground electron-hole-subband of the QWrs. A significant spectral narrowing is also found as the power density is increased and crosses the lasing threshold. This evidences the existence of amplified spontaneous emission within this inhomogeneously broadened PL line in this density regime. The observable emission intensity varies linearly at low excitation power over three orders of magnitude (from 0.1 to 100 mW) [200]). Above the lasing threshold (at 350 mW) the intensity variation is again linear (see, Fig. 4.6b), indicating that the modal gain is saturated. In Fig. 4.6c, a high-resolution emission spectrum obtained above threshold features well-resolved Fabry-Perot modes that correspond to different longitudinal optical modes within the inhomogeneuous line of the QWr-PL. Detailed investigations of PL and PLE spectra (see, Fig. 4.7) of the QWr allowed the indicated authors to conclude that the lasing emission originates from the recombination of excitons as it is the case for the QWr-peak of the cw-PL spectrum (for details see [200]).

In QDs, as indicated above, carriers are confined in the three directions in a very small region of space, producing quantum effects in the electronic properties. As we can see from Fig. 3.6, the electronic joint density of states for QD shows sharp peaks corresponding to transitions between discrete energy levels of electrons and holes. Outside these levels the DOS vanishes. In many ways, the electronic structure of a QD resembles that of a single atom [111]. Lasers based on *QDs* could have properties similar to those of conventional ion gas lasers, with the advantage that the electronic structure of a QD can be engineered by changing the base material, size, and shape. In the next we assume that the QDs are small enough so that the

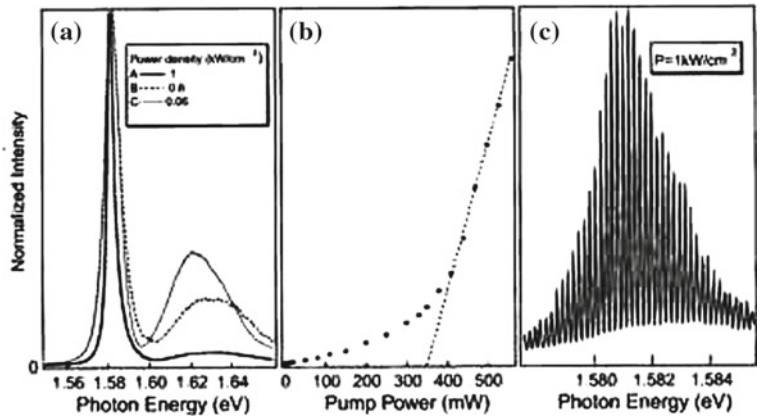

Fig. 4.6 **a** Photoluminescence spectra at 10 K of the QWr laser sample above, below and near the lasing threshold in TE-polarization. **b** Dependence on input excitation power of the PL output power;arrows indicate the excitation powers used for the optical spectra depicted in (**a**). **c** High resolution emission spectrum above the lasing threshold showing the Fabri–Perrot modes of the optical cavity (after [200])

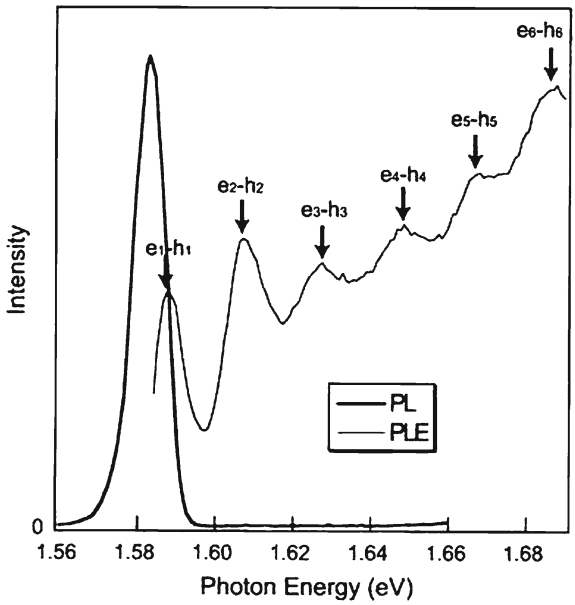

Fig. 4.7 Linearly-polarized PLE spectrum and the corresponding PL spectrum of an etched QWr laser sample at 10 K. The polarization of the excitation is parallel to the wire axis. The different optical transition e_n–h_n are marked by arrows (after [200])

separation between the first two electron energy levels for both electrons and holes is much larger than the thermal energy KT. Then for an undoped system, injected electrons and holes will occupy only the lowest level. Therefore, all injected electrons will contribute to the lasing transitions from the E_{1e} to the E_{1hh} levels, reducing the threshold current with respect to other systems with lower confinement. The evolution

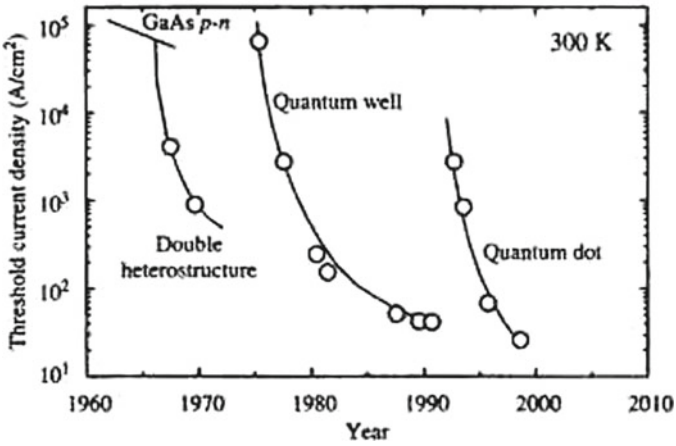

Fig. 4.8 Evolution of threshold current density for lasers based on different confinement structures (after [200])

of the threshold current density obtained along the years for various laser structures is shown in Fig. 4.8. The lowest threshold currents have already been reached for QD lasers [200]. As long as the thermal energy is lower than the separation between the fist and second levels, the emission band in an ideal QD laser is very sharp and does not depend on temperature (see, also [187, 188]. Therefore, QD lasers should have a better stability with temperature without the need for cooling. We should add that QDs have the narrowest spectrum and the highest gain (for details see also [1, 74, 187, 188]).

4.5 Isotope-Based Quantum Computers

The development of efficient quantum algorithms for classically hard problems has generated interest in the construction of a quantum computer. A *quantum computer* uses superpositions of all possible input states. By exploiting this quantum parallelism, certain algorithms allow one to factorize [202] large integers with astounding speed, and rapidly search through large databases [203], and efficiently simulate quantum systems [204]. In the nearer term such devices could facilitate secure communication and distributed computing. In any physical system, bit errors will occur during the computation. In *quantum computing* this is particularly catastrophic, because the errors cause decoherence [205, 206] and can destroy the delicate superposition that needs to be preserved throughout the computation. With the discovery of quantum error correction [207–209] and fualt-tolerant computing, in which these errors are continuously corrected without destroying the quantum information, the construction of a real computer has became a distinct possibility (see also [210]). The

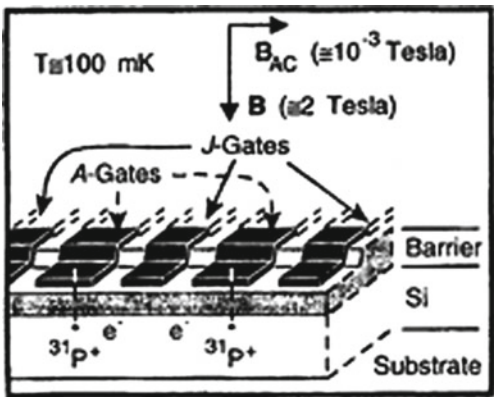

Fig. 4.9 Illustration of two cells in a one-dimensional array containing ^{31}P donors and electrons in a Si host, separated by a barrier from metal gates on the surface. "A gates" control the resonance frequency of the nuclear spin qubits; "J gates" control the electron-mediated coupling between adjacent nuclear spins. The ledge over which the gates cross localizes the gate electric field in the vicinity of the donors (after [212, 213])

tasks that lies ahead to create an actual quantum computer are formidable: Preskill [211] has estimated that a quantum computer operating on 10^6 qubits with a 10^{-6} probability of error in each operation would exceed the capabilities of contemporary conventional computers on the *prime factorization problem*. To make use of error-correcting codes, logical operations and measurement must be able to proceed in parallel on qubits throughout the computer.

Phosphorous donors in *silicon* present a unique opportunity for solid-state quantum computation [212, 213]. Electrons spins on isolated Si:P donors have very long decoherence times of ∼60 ms in isotopically purified ^{28}Si at 7 K [214]. By contrast, electron spin dephasing times in GaAs (for example) are orders-of-magnitude shorter due to spin–orbit interaction; and the background nuclear spins of the III–V host lattice cannot be eliminated by isotope selection. Finally, the Si:P donor is a self-confined, perfectly uniform single-electron quantum dot with a non-degenerate ground state. A strong Coulomb potential breaks the six-valley degeneracy of the silicon conduction band near donor site, yielding a substantial energy gap of ∼15 meV to the lowest excited [215] as needed for quantum computation. As we all know, the Si:^{31}P system was exhaustively studied more than 40 years ago in the first electron-nuclear double-resonance experiments. At sufficiently low ^{31}P concentrations at temperature $T = 1.5$ K, the electron spin relaxation time is thousands of seconds and the ^{31}P nuclear spin relaxation time exceeds 10 h. It is likely that at millikelvin temperatures the phonon limited ^{31}P relaxation time is of the order of 10^{18} seconds [216], making, as we said above, this system ideal for quantum computation.

Kane's original proposal [212, 213] envisions encoding quantum information onto the nuclear spin 1/2 states of ^{31}P qubits in a spinless $I = 0^{28}$Si lattice. The Kane architecture employs an array of top-gates (see Fig. 4.9). to manipulate the ground state wavefunctions of the spin-polarized electrons at each donor site in a high magnetic field $B \sim 2$ T, at very low temperature ($T \simeq 100$ mK). "A -gates" above each donor turn single-qubit NMR rotations via the contact hyperfine interaction; and "J-gates" between them induce an indirect two-qubit nuclear exchange interaction

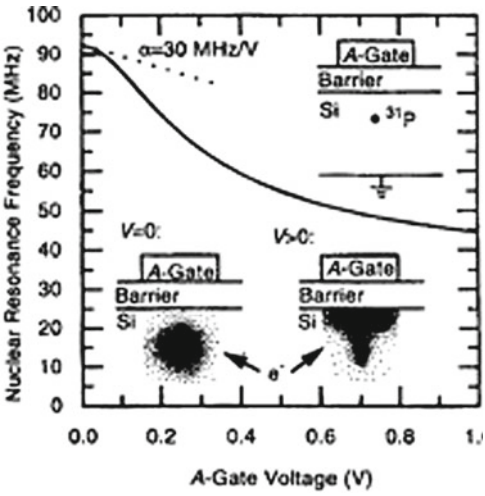

Fig. 4.10 An electric field applied to an A gate pulls the electron wavefunction away from the donor and towards the barrier, reducing the hyperfine interaction and the resonance frequency of the nucleus. The donor nucleus-electron system is a voltage-controlled oscillator with a tuning parameter α of the order 30 MHz (after [212, 213])

via overlap of the spin-polarized electron wavefunctions. In other words, spin—1/2 ^{31}P donor nuclei are qubits, while donor electrons together with external A—gates provide single-qubit (using external magnetic field) and two-qubit operations (using hyperfine and electron exchange interactions). Specifically, the single. donor nuclear spin splitting is given by [212, 213]

$$\hbar\omega_A = 2g_n\mu_n B + 2A + \frac{2A^2}{\mu_B B}, \tag{4.3}$$

where g_n is the nuclear spin g-factor (= 1.13 for ^{31}P [212, 213]), μ_n is the nuclear magneton, A is the strength of the hyperfine coupling between the ^{31}P nucleus and the donor electron spin, and B is the applied magnetic field. It is clear that by changing A one can effectively change the nuclear spin splitting, thus allowing resonant manipulations of individual nuclear spins (Fig. 4.10). If the donor electrons of two nearby donors are allowed to overlap, the interaction part of the spin Hamiltonian for the two electrons and the two nuclei include electron-nuclear hyperfine coupling and electron-electron exchange coupling (see also [212, 213]).

$$H = H_{Zeeman} + H_{int} = H_{Zeeman} + A_1\vec{S_1}\cdot\vec{I_1} + A_2\vec{S_2}\cdot\vec{I_2} + J\vec{S_1}\vec{S_2}, \tag{4.4}$$

where $\vec{S_1}$ and $\vec{S_2}$ represent the two electron spins, $\vec{I_1}$ and $\vec{I_2}$ are the two nuclear spins, A_1 and A_2 represent the hyperfine coupling strength at the two donor sites, and J is the exchange coupling strength between the two donor electrons, which is determined by the overlap of the donor electron wavefunctions. The lowest order p *erturbation calculation* (assuming $A_1 = A_2 = A$ and J is much smaller than the electron Zeeman splitting) results in an effective exchange coupling between the two

nuclei and the coupling strength is (see [212, 213])

$$J_{nn} = \frac{4\mathrm{A}^2\mathrm{J}}{\mu_B \mathrm{B}\,(\mu_B \mathrm{B} - 2\mathrm{J})}. \tag{4.5}$$

Now the two donor electrons essentially shuttle different nuclear spin qubits and are controlled by external gate voltages. The final measurement is done by first transferring nuclear spin information into electron spins using hyperfine interaction, then converting electron spin information into charge states such as charge locations [217]. A significant advantage of silicon is that its most abundant isotope ^{28}Si is spinless, thus providing a "quiet" environment for the donor nuclear spin qubits. In addition, Si has also smaller intrinsic spin–orbit coupling than other popular semiconductors such as GaAs. In general, nuclear spins have very long coherence times because they do not strongly couple with their environment, and are thus good candidates for qubits (see, also [217–220]).

Although the nuclear spin offers unlimited decoherence times for quantum information processing, the technical problems of dealing with nuclear spins through the electrons are exceedingly difficult. A modified version of the Kane architecture was soon proposed using the spin of the donor electron as the qubit [221–224]. In the first scheme [221], A-gates would modulate the electron g-factor by polarizing its ground state into Ge-rich regions of a SiGe heterostructure for selective *ESR rotations*, while two-qubit electron exchange is induced through wavefunction overlap. In the studies of Shlimak et al. [222–224] was used the new technology for growth of SIGE heterostructures. Recent achievement in Si/Ge technology allows one to obtain high quality heterojunctions with a mobility of about $(1\text{–}5)\times 10^5$ cm^2 V^{-1}s^{-1} [225]. Using Si/Ge heterostructures has several advantages concerning semiconductor-based nuclear spin quantum computers (S–NSQCs). First, the concentration of nuclear spins in Ge and Si crystals is much lower, because only one isotope (^{73}Ge and ^{29}Si [31]) has a nuclear spin, and the natural abundance of this isotope is small (see, also [56]). Second, the variation of isotopic composition for Ge and Si will lead to the creation of a material with a controlled concentration of nuclear spin, and even without nuclear spins. Utilization of isotopically engineered Ge and Si elements in the growth of the active Si/Ge layers could help realize an almost zero nuclear spin layer that is coplanar with the 2DEG. Then, one might deliberately vary the isotopic composition to produce layers, wires, and dots that could serve as nuclear spin qubits with a controlled number of nuclear spins (see also [226]).

The key point of a novel technology is the growth of the central Si and barrier $Si_{0.85}Ge_{0.15}$ layers from different isotopes: the $Si_{0.85}Ge_{0.15}$ layers from isotope ^{28}Si and ^{72}Ge and the central Si layer from isotope ^{28}Si with ^{30}Si spots introduced by means of the nano-litography (see Fig. 4.11) (see also [227]). The formation of quasi-1D Si wires will be achieved in a subsequent operation by the etching of Si layer between wires and the filling of the resulting gaps by the $Si_{0.85}Ge_{0.15}$ barrier composed from isotopes ^{28}Si and ^{72}Ge. Because different isotopes of Si and Ge are chemically identical, this technology guarantees the high quality of the grown struc-

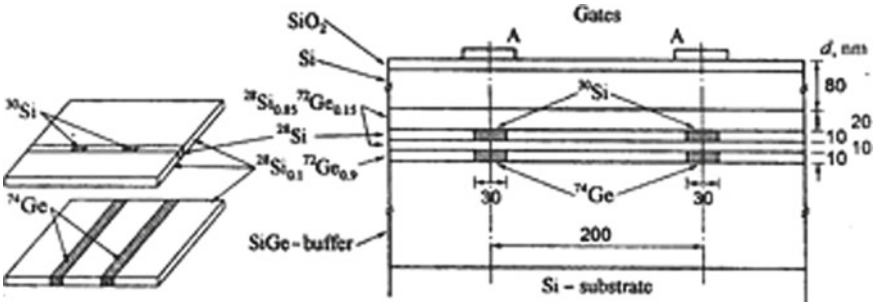

Fig. 4.11 Schematics of the proposed device. After NTD, ^{31}P donors appear only inside the ^{30}Si-spots and underlying ^{74}Ge strips will be heavily doped with ^{75}As donors. All sizes are shown in nm (after [222–224])

tures [222–224]. After preparation, these structures will be irradiated with a neutron flux in a nuclear reactor by the fast annealing of radiation damage.

As was shown by Di Vincenzo [228] *two-bit gates* applied to a pair of electron or nuclear spins are universal for the verification of all principles of quantum computation. Because direct overlap of wavefunctions for electrons localized on P donors is negligible for distant pairs, the authors of [222–224] proposed another principle of coupling based on the placement of qubits at fixed positions in a quasi-1D Si nanowire and using the indirect interaction of ^{31}P nuclear spins with spins of electrons localized in the nanowire which they called as "1D-electrons". This interaction depends on the amplitude of the wavefunction of the "1D - electron" estimated at the position of the given donor nucleus $\Psi_n(\mathrm{r_i})$ and can be controlled by the change in the number of "1D-electrons" N in the wire. At $N = 0$, the interqubit coupling is totally suppressed, each ^{31}P nuclear spin interacts only with its own donor electron. This situation is analogous to that suggested in the Kane proposal [217, 218] and therefore all single-qubit operations and estimates of the decoherence time are valid also in the model by Shlimak et al. [222–224].

Below we briefly analyze the schematics of the device architecture which satisfies the scalability requirements of the *quantum computer* suggested in [222–224]. Figure 4.12 shows the schematics of the device architecture which allows one to vary l (length of *quantum wire*) and N. The device consists of a ^{28}Si nanowire with an array of ^{30}Si spots. Each spot is supplied by the overlying A-gate, the underlying Source-drain-channel and the lateral N-gate. After NTD, P donors will appear in most of the spots (which transforms these spots into qubits) and not appear in other spots (non-qubits). In Fig. 4.12 it is assumed that spots 3 and 4 are non-qubits (0-spots) and one needs to provide coupling between qubits 2 and 5. For this purpose, it is necessary to connect the gates N_2, N_3, N_4 and N_5. The negative voltage applied between other N-gates and the wire contact L will lead to pressing-out "1D-electrons" from all corresponding areas and formation of the nanowire with $l = 800$ nm between the sites 2 and 5 only (shown in grey in Fig. 4.12). The coupling between qubits 2 and 5 will be realized via injection in the wire of the necessary number of electrons N,

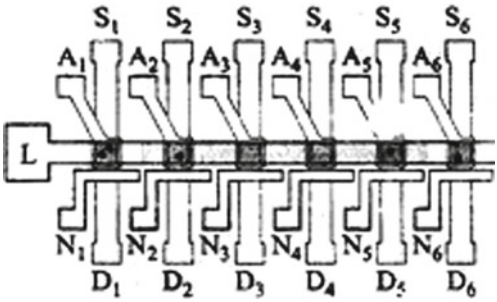

Fig. 4.12 Schematics of a ^{28}Si nanowire L with an array of ^{30}Si spots (qubits and non-qubits after NTD). Each spot is supplied by overlying A-gate, underlying source-drain-channel and lateral N-gate. This device architecture allows to realize an indirect coupling between any distant qubits (for details see text) (after [222–224])

Table 4.1 Important times for various two-level systems in quantum mechanics that might be used as qubits, including prospective qubits ranging from nuclear physics, through atomic, electronic, and photonic systems, to electron and nuclear spins

Quantum system	t_{switch}, s	t_Φ, s	Ratio
Mössbauer nucleus	10^{-19}	10^{-10}	10^9
Electrons: GaAs	10^{-13}	10^{-10}	10^3
Electrons: Au	10^{-14}	10^{-8}	10^6
Trapped ions: In	10^{14}	10^{-1}	10^{13}
Optical microcavity	10^{-14}	10^{-5}	10^9
Electron spin	10^{-7}	10^{-3}	10^4
Electron quantum dot	10^{-6}	10^{-3}	10^3
Nuclear spin	10^{-3}	10^4	10^7

The time t_{switch} is the minimum time required to execute one quantum gate; it is estimated as $\hbar/\Delta E$, where ΔE is the typical energy splitting in the two level system; the duration of a π tipping pulse cannot be shorter than this uncertainty time for each system. The phase coherence time as seen experimentally, t_Φ, is the upper bound on the length of time over which a complete quantum computation can be executed accurately. The ratio of these two times gives the largest number of steps permitted in a quantum computation using these quantum bits (after [228])

using the positive voltage applied to the gates N_2–N_5. According to [222–224], the maximal coupling will be realized at $N = 7$, while at $N = 0$, the coupling will be totally suppressed.

Concluding this part we present Table 4.1 giving the important times for various two-level systems in quantum mechanics that might be used as quantum bits according to [229] (see also [205, 206]).

References

1. M.J. Kelly, *Low-Dimensional Semiconductors* (Clarendon Press, Oxford, 1995)
2. J.H. Davis, *The Physics of Low-Dimensional Semiconductors* (Cambridge University Press, Cambridge, 1998)
3. P. Harrison, *Quantum Wells, Wires and Dots* (Wiley, New York, 2001)
4. K. Goser, P. Glösekötter, J. Dienstuhl, *Nanoelectronics and Nanosystems* (Springer, Berlin, 2004)
5. A. Cho (ed.), *Molecular Beam Epitaxy* (Springer, Berlin, 1997)
6. G.B. Stringfellow, *Organometallic Vapor–Phase Epitaxy: Theory and Practice*, 2nd edn. (Academic, London, 1999)
7. A. Rastelli, S. Kiravittaya, O.G, Schmidt, in *Nanoscience and Technology*, ed. by P. Mihler. Growth and Control of Optically Active Quantum Dots (Springer, Berlin, 2009)
8. V.A. Shchukin, D. Bimberg, Spontaneous ordering of nanostructures on crystal surfaces. Rev. Mod. Phys. **71**(4), 1125–1171 (1999)
9. J. Strangl, V. Holy, G. Bauer, Structural properties of self-organized semiconductor nanostructures. Rev. Mod. Phys. **76**, 725–783 (2004)
10. C.J. Chen, *Introduction to Scanning Tunneling Microscopy* (Oxford University Press, New York, 1993)
11. L. Esaki, R. Tsu, Supelattice and negative differential conductivity in semiconductors. IBM J. Res. Develop. **14**, 61 (1970)
12. V.G. Plekhanov, *Applications of the Isotopic Effect in Solids* (Springer, Berlin, 2004)
13. V.G. Plekhanov, *Isotope–based quantum information*, ArXiv: quant - ph 0909.0820 (2009)
14. P. Michler (ed.), *Single Semiconductor Quantum Dots* (Springer, Berlin, 2009)
15. G. Bastard, *Wave Mechanics Applied to Semiconductor Heterostructures* (Halsted Press, New York, 1988)
16. C. Weisbuch, B. Vinter, *Quantum Semiconductor Structures* (Academic, San Diego, 1991)
17. D. Pines, *Elementary Excitations in Solids* (W.A. Benjamin Inc., New York, 1963)
18. S.I. Pekar, *Crystaloptics and Addition Waves* (Naukova Dumka, Kiev, 1982). (in Russian)
19. G.P. Srivastava, *The Physics of Phonons* (Hilger, Bristol, 1990)
20. V.G. Plekhanov, *Isotope-mixed Crystals*: *Fundamentals and Applications* (e-books, Bentham, 2011, ISBN : 978-1 60805-091-8)
21. V.G. Plekhanov, *Manifestation and Origin of the Isotope Effect*, ArXiv:phys/ 0907.2024 (2009)
22. V.G. PLekhanov, *Giant Isotope Effect in Solids* (Stefan–University Press, La Jola, 2004)
23. J. Callaway, *Energy Band Structure* (Academic, New York, 1964)
24. R.M. Martin, *Electronic Structure–Basic Theory and Practical Methods* (Cambridge University Press, Cambridge, 2004)
25. J.M. Ziman, *Electrons and Phonons* (Oxford University Press, London, 1963)

DOI: 10.1007/978-3-642-28613-1, © The Author(s) 2012

26. N.W. Aschcroft, N.D. Mermin, *Solid State Physics* (Holt Reinhart and Winston, New York, 1975)
27. M.L. Cohen, J. Chelikowsky, *Electronic Properties and Optical Properties of Semiconductors*, 2nd edn. Springer Series Solid State Sci., vol 75 (Springer, Berlin, 1989)
28. M. Born, J.R. Oppenheimer, Zur Quanttheorie der Moleculen. Ann. Phys. **389**(20), 457–484 (1927)
29. J.C. Slater, *Electronic Structure of Molecules*, vol 1 (McCraw–Hill Company Inc., New York, 1963)
30. J.L. Birman, in *Handbuch für Physik*, vol 25/26, Space Group Symmetry (Springer, Berlin, 1974)
31. V.G. Plekhanov, Elementary excitations in isotope–mixed crystals. Phys. Rep. **410**(1–3), 1–235 (2005)
32. T. Collins et al., Phys. Rev. Lett. **65**, 891 (1990)
33. V.G. Plekhanov, Uspekhi Fiz. Nauk (Moscow) **167**, 577 (1997). (in Russian)
34. K. Chandahari et al., Solid State Commun. **100**, 777 (1996)
35. L.F. Lastras-Martinez et al., Phys. Rev. **B61**, 12946 (2000)
36. D. Karaiskaja et al., Solid State Commun. **123**, 87 (2002)
37. F.I. Kreingol'd, Fizika Tverdogo Tela **20**, 3138 (1978). (in Russian)
38. F.J. Manjon et al., Solid State Commun. **128**, 35 (2003)
39. T.A. Meyer et al., Solid State Commun. **126**, 119 (2003)
40. N. Garro et al., Phys. Rev. **B54**, 4732 (1996)
41. N. Garro et al., Solid State Commun. **98**, 27 (1996)
42. F.I. Kreingol'd, B.S. Kulinkin, Fizika Tverdogo Tela **28**, 3164 (1986). (in Russian)
43. J.M. Zhang et al., Phys. Rev. **B57**, 9716 (1998)
44. F.I. Kreingol'd (1976) Pis'ma v ZETPH **23**: 679, Fizika Tverdogo Tela **27**: 2839 (in Russian)
45. V.F. Agekyan et al., Fizika Tverdogo Tela **31**, 101 (1989) (in Russian)
46. C. Parks et al., Phys. Rev. **B49**, 14244 (1994)
47. E.E. Haller, J. Appl. Phys. **77**, 2857 (1995)
48. P.A.M. Dirac, *The Principles of Quantum Mechanics* (Oxford University Press, Oxford, 1958)
49. R.P. Feynman, R.P. Leighton, M. Sands, *The Feynman Lecture in Physics*, vol 3 (Addison–Wesley, Reading, 1965)
50. L.D. Landau, E.M. Lifshitz, *Quantum Mechanics (Nonrelativistic Theory)* (Pergamon Press, New York, 1977)
51. R. Loudon, The Raman effect in crystals. Adv. Phys. **13**(2), 423–488 (1964)
52. R.A. Cowley, Anharmonicity. J. Phys. (Paris) **26**(3), 659–664 (1965)
53. R.A. Cowley, Anharmonic crystals. Rep. Prog. Phys. **31**(2), 123–166 (1968)
54. M.A. Eliashevich, Mechanics of the vibrations of molecules. Uspekhi Fiz. Naul **48**(4), 482–544 (1946). (in Russian)
55. D.A. Long, *Raman Spectroscopy* (McGraw–Hill, UK, 1977)
56. M. Cardona, M.L.W. Thewalt, Isotope effect on optical spectra of semiconductor. Rev. Mod. Phys. **77**, 1173–1224 (2005). Oct
57. V.F. Agekyan, A.M. Asnin, V.M. Kryukov et al., Isotope effect in germanium. Fiz. Tverd. Tela **31**(12), 101–104 (1989). (in Russian)
58. H.D. Fuchs, P. Etchegoin, M. Cardona et al., Vibrational band modes in germanium: Isotopic disorder–induced Raman scattering. Phys. Rev. Lett. **70**, 1715–1718 (1993)
59. V.G. Plekhanov, in *Semiconductors and Semimetals Isotope,*, ed. by R.K. Willardson, E. Weber. Effect in Solid State Physics, vol 68 (Academic, San Diego, 2001)
60. H. Hanzawa, N. Umemura, Y. Nishida, H. Kanda, Disorder effect of nitrogen impurities, irradiation–induced defects and ^{13}C composition on the Raman spectrum in syntethic I^b diamond. Phys. Rev. **B54**(6), 3793–3799 (1996)
61. V.G. Plekhanov, Isotope effects in lattice dynamics. Phys. Uspekhi **46**(7), 689–715 (2003)

62. R.M. Chrenko, ^{13}C–doped diamond: Raman spectra. Appl. Phys. **63**(12), 5873–5875 (1988)
63. K.C. Hass, M.A. Tamor, T.R. Anthony, W.F. Banholzer, Effect of isotopic disorder on the phonon spectrum of diamond. Phys. Rev. **44**, 12046–12053 (1991)
64. S.H. Solin, A.K. Ramdas, Raman spectrum of diamond. Phys. Rev. **B1**(4), 1687–1699 (1970)
65. V.G. Plekhanov, Isotope effects on the lattice dynamics of crystals. Materials Sci. Eng. **R35**(4–6), 139–237 (2001)
66. R.J. Elliott, J.A. Krumhansl, P.L. Leath, The theory and properties of randomly disordered crystals and physical systems. Rev. Mod. Phys. **46**(3), 465–542 (1974)
67. I.F. Chang, S.S. Mitra, Long wavelength of optical phonons in mixed crystals. Adv. Phys. **20**(85), 360–404 (1971)
68. I.P. Ipatova, in, *Optical Properties of Mixed Crystals* (Modern Problems in Condensed Matter Sciences, vol 23) ed. by R.J. Elliott, I.P. Ipatova, Universal parameters in mixed crystals (North–Holland, Amsterdam, 1988), Ch. 1, pp. 1–34
69. V.G. Plekhanov, Experimental evidence of strong phonon scattering in isotopical disordered systems: the case LiH_xD_{1-x}, Phys. Rev. **B51**, 8874–8878 (1995), ArXiv: cond - mat/0907.3817
70. V.G. Plekhanov, Direct observation of two–mode LO(Γ) phonons at large concentration of isotopes in LiH_xD_{1-x}. Opt. Spectr. **75**(1), 51–53 (1993). (in Russian)
71. V.G. Plekhanov, Isotope and disorder effects in the Raman spectra of LiH_xD_{1-x} crystals. J. Raman Spectr. **32**, 631–642 (2001)
72. V.G. Plekhanov, Fundamentals and applications of isotope effect in modern technology, J. Nucl. Sci. and Technol. (Japan) **43**(4), 375–381 (2006), ArXiv: cond–mat/0807. 2521 (2008)
73. M.A. Herman, W. Richter, H. Sitter, *Epitaxy, Physical Principles and Technical Implementation*, vol. 62, Springer Series in Materials Science (Springer, Berlin, 2004)
74. K. Barnham, D. Vvedensky, *Low-dimensional Semiconductor Structures* (Cambridge University Press, Cambridge, 2009)
75. http://www.uccs.edu/tchriste/courses/ PHYS 549/ 549 lectures/mbe. html.
76. S. Kiravittaya, A. Rastelli, O.G. Schmidt, Advanced quantum dot configurations, Rep. Prog. Phys. **72**, 046502 (p. 34) (2009)
77. A. Grenville, R.L. Hseih, R. von Bunan et al., Makle–Dyson optics for $0.25 \cdot 10^{-6}$ m litography and beyond. J. Vacuum Sci. Technol. **B9**, 3108–3112 (1991)
78. C.I.H. Ashby, *Etching of GaAs: Overview, in Properties of Gallium Arsenide*, 2nd edn. (Institute of Electrical Engineers, London, 1990)
79. T. Ito, Sh. Okazaki, Pushing the limits of litography. Nature **406**, 1027–1031 (2000)
80. V.J. Low, S.G. Ingram, M. Tewordt et al., Reactive ion etching of GaAs using CH_4. Semicond. Sci. Technol. **6**, 411–413 (1991)
81. D.E. Sykes, in *Methods of Surface Analysis* ed. by T.M. Walls. Dynamical secondary ion mass spectroscopy, (Cambridge University Press, Cambridge, 1989), pp. 216–262
82. V.G. Plekhanov, Wannier–Mott excitons in isotope—disordered crystals. Rep. Prog. Phys. **61**(8), 1045–1095 (1998)
83. P. Ballet, J.B. Smathers, H. Yang et al., Control of size and density of InAs/(Al, Ga)As self-organized islands. J. Appl. Phys. **90**(1), 481–487 (2001)
84. E.G. Britton, K.B. Alexander, W.M. Strobbs et al., The atomic scale characterization of multilayer semiconductor structures using TEM. GEC J. Res. **5**, 31–39 (1987)
85. W.M. Stobbs, in *The Physics and Fabrication of Microstructures and Microdevices*, ed. by M.J. Kelly, C. Weisbuch. Recently developed TEM approach for the characterization of semiconductor heterostructures and interfaces (Springer, Berlin, 1986), pp 136–149
86. D.M. Bruls, P.M. Koenraad, H.W.M. Salemink et al., Stacked long–growth–rate InAs quantum dots studied at the atomic level by cross-sectional STM. Appl. Phys. Lett. **82**(21), 3752–3755 (2003)

87. B. Grandidier, Y.M. Niquet, J.P. Nys et al., Imaging the wave–function amplitudes in cleaved semiconductor quantum boxes. Phys. Rev. Lett. **85**(5), 1068–1071 (2000)
88. S. Kret, T. Benabbes, C. Delamarre et al., High resolution electron microscope analysis of lattice distortions and In segregation in highly strained $In_{0.35}Ga_{0.65}As$ coherent islands grown on GaAs (001). J. Appl. Phys. **86**(4), 1988–1993 (1999)
89. A.A. Berezin, Isotope superlattices and isotopically ordered structures. Solid State Commun. **65**(8), 819–821 (1988)
90. E.E. Haller, Isotope heterostructures selectively doped by neutron transmutation. Semicond. Sci. technol. **5**(4), 319–321 (1990)
91. M. Cardona, P. Etchegoin, H.D. Fuchs et al., Effect of isotopic disorder and mass on the electronic and vibronic properties of three-, two- and one-dimensional solids. J. Phys. Condens Matter **5**(1), A61–A72 (1993)
92. J. Spitzer, T. Ruf, W. Dondl et al., Raman scattering by optical phonons in isotopic $^{70}(Ge)n^{74}(Ge)n$ superlattices. Phys. Rev. Lett. **72**(10), 1565–1568 (1994)
93. E. Silveira, W. Dondl, G. Abstreiter et al., Ge self–diffusion in isotopic $^{70}(Ge)_n^{74}(Ge)_m$ superlattices: A Raman study. Phys. Rev. **B56**(4), 2062–2069 (1997)
94. M. Nakajima, H. Harima, K. Morita et al., Coherent confined LO phonons in $^{70}Ge/^{74}Ge$ isotope superlattices generated by ultrafast laser pulses, Phys. Rev. B63, pp. 161304–161314 (R) (2001)
95. A.V. Kolobov, K. Morita, K.M. Itoh et al., A Raman scattering study of self-assembled pure isotope Ge/Si (100) quantum dots. Appl. Phys. Lett. **81**(21), 3855–3857 (2002)
96. T. Kojima, R. Nebashi, Y. Shiraki et al., Growth and characterization of $^{28}Si/^{30}Si$ isotope superlattices. Appl. Phys. Lett. **83**(12), 2318–2320 (2003)
97. L.M. Zhuravleva, V.G. Plekhanov, Nuclear technology in creation of low-dimensional isotope-mixed structures. Nanoindustry **4**(16), 28–30 (2009) (in Russian), www.nanoindustry.su
98. P.W. Anderson, Absence of diffusion in certain random lattices. Phys. Rev. **109**(5), 1492–1505 (1958)
99. H. Bilz, W. Kress, *Phonon Dispersion Relations in Insulators* (Springer, Berlin, 1979)
100. G.L. Bir, G.E. Picus, *Symmetry and Deformation in Semiconductors* (Science, Moscow, 1972). (in Russian)
101. G. Fasol, M. Tanaka, H. Sakaki et al., Interface roughness and dispersion of confined LO phonons in GaAs/AlAs quantum wells. Phys. Rev. **B38**(22), 6056–6065 (1988)
102. M. Namiki, S. Pascazio, Quantum theory of measuremen based on the many–Hilbert–space approach. Phys. Reports **232**(6), 301–411 (1993)
103. N. Gerasimenko, Ju. Parhomenko, *Silicon–Material of Nanoelectronics* (Technosphera, Moscow, 2007). (in Russian)
104. B.B. Kadomtsev, *Dynamics and Information* (UFN, Moscow, 1997). (in Russian)
105. A.M. Fox, Optoelectronics in quantum well structures. Contemp. Phys. **37**(2), 11–125 (1996)
106. H. Grabert (ed.), Special issue on Single Charge Tunneling, Zs. Physik, vol 85, Suppl 3 (1991)
107. H. Grabert, M.H. Devored (eds.), *Single Charge Tunneling: Coulomb Blockade Phenomena in Nanostructures*, vol. 294, NATO ASI Series B (Plenum, New York, 1992)
108. S. Washburn, R.A. Webb, Quantum transport in small disordered samples from the diffuse to the ballistic regime. Rep. Prog. Phys. **55**(8), 1311–1383 (1992)
109. D.V. Averin, A.N. Korotkov, K.K. Likharev, Theory of single electron charging of quantum wells and dots. Phys. Rev. **44**(12), 6199–6211 (1991)
110. J. Bylander, T. Duty, P. Delsing, Current measurement by real–time counting of single electrons. Nature **434**(1), 361–364 (2005)
111. D. Bimberg, M. Grundman, N.N. Ledentsov, *Quantum Dot Heterostructure* (Wiley, Chichester, 1999)
112. L. Jacak, P. Hawrylak, A. Wojs, *Quantum Dots* (Springer, Berlin, 1998)

113. G.W. Bryant, G.S. Solomon (eds.), *Optics of Quantum Dots and Wires* (Artech House Inc., London, 2005)
114. H.J. Krenner, S. Stufler, M. Sabathil et al., Recent advances in exciton–based quantum information processing in quantum dot nanostructures. New J. Phys. **7**(1), 185–27 (2005)
115. R.S. Knox, *Theory of Excitons, Solid State Phys*ics, Suppl 3 (Academic, New York, 1963)
116. R.J. Nelson, in *Excitons*, ed. by E.I. Rashba, M.D. Sturge. Excitons in semiconductor alloys, (North–Holland Publ. Co, Amsterdam, 1982), Ch. 8, pp. 319–348
117. K.K. Bajaj, Use of excitons in material characterization of semiconductor system. Materials Sci. Eng. R. **24**(1), 59–120 (2001)
118. J.M. Luttinger, W. Kohn, Motion of electrons and holes in perturbed periodic fields. Phys. Rev. **97**(4), 869–883 (1955)
119. J.M. Luttinger, Quantum theory of cyclotron resonance in semiconductors: General theory. Phys. Rev. **102**(4), 1030–1041 (1956)
120. K. Seeger, *Semiconductor Physics* (Springer, New York, 1973)
121. A. Baldareschi, N.O. Lipari, Energy levels of direct excitons in semiconductors with degenerate bands. Phys. Rev. **B3**(2), 439–451 (1971)
122. G. Bastard, E.E. Mendez, L.L. Chang, L. Esaki, Exciton binding energy in quantum wells. Phys. Rev. **B26**(4), 1974–1979 (1982)
123. L.V. Keldysh, Excitons in semiconductor–dielectric nanostructures, phys. stat. solidi A **164**(1), 3–12 (1997)
124. R.C. Miller, D.A. Kleinman, W.T. Tsang, Observation of the excited level of excitons in GaAs quantum wells, Phys. Rev. **B24**(2), 1134–1136 (1981); phys. stat. solidi A **B25**, 6545–6549 (1982)
125. R.L. Greene, K.K. Bajaj, D.E. Phelps, Energy levels of Wannier excitons in GaAs–$Ga_{1-x}Al_xAs$ quantum–well structures, phys. stat. solidi A **B29**(4), 1807–1812 (1984)
126. R.L. Greene, K.K. Bajaj, Binding energies of Wannier excitons in GaAs–$Ga_{1-x}Al_xAs$ quantum–well structures. Solid State Commun. **88**(11–12), 955–959 (1993)
127. M. Altarelli, Electronic structure and semiconductor–semimetal transitions. Phys. Rev. **B28**(2), 842–845 (1983)
128. M. Altarelli, Electronic structures of two-dimensional systems. J. Luminesc. **30**(1–4), 472–487 (1985)
129. A. Fasolino, M. Altarelli, in Two-Dimensional Systems, Heterostructures and Superlattices, ed. by G. Bauer, F. Kucher, H. Heinrich. Springer Series in Solid State Sci., vol 43, pp. 176–212 (1984)
130. R. Dingle, in *Festkörperprobleme*, vol 15 of Advances in Solid State Phys., ed. by H.J. Quesser (Braunschweig, Pergamon/Vieweg, 1975), p. 21
131. J. Hegarty, M.D. Sturge, Studies of exciton localization in quantum-well structures by non-linear recniques. JOSA **B2**(7), 1143–1154 (1985)
132. P. Dawson, K.J. Moore, G. Duggan et al., Unambiguous observation of the 2S state of the light- and heavy-hole excitons in GaAs–(AlGa)As MQW structures. Phys. Rev. **B34**(8), 6007–6010 (1986)
133. F. Rossi, E. Molinari, Linear and nonlinear optical properties of realistic quantum–wire structures: The dominant role of Coulomb correlation. Phys. Rev. **B53**(24), 16462–16473 (1996)
134. M. Bruno, M. Palummo, A. Marini et al., Excitons in germanium nanowires. Phys. Rev. **B72**, 153310–153314 (2005)
135. S. Osscini, *Light Emitting Silicon for Microphotonics*, vol. 194, Springer Tracrs in Modern Physics (Springer, Berlin, 2003)
136. S.A. Moskalenko, Towards to theory of Mott excitons in alkali halides crystals. Opt. Spectr. **5**(2), 147–155 (1958)
137. M.A. Lampert, Mobile and immobile effective–mass–particle complexes in nonmetallic solids. Phys. Rev. Lett. **1**(12), 450–453 (1958)

138. V.G. Plekhanov, Fundamentals and applications of isotope effect in solids. Prog. Mat. Sci. **51**(3), 287–426 (2006)
139. B. Hönerlage, R. Levy, J.B. Grun et al., The dispersion of excitons, polaritons and biexcitons in direct–gap semiconductors. Phys. Reports **124**(3), 163–253 (1985)
140. D. Birkedal, J. Singh, V.G. Lyssenko et al., Binding of quasi-two-dimensional biexcitons. Phys. Rev. Lett. **76**(4), 672–675 (1996)
141. G. Bacher, T. Kümmel, Optical properties of epitaxially grown wide bandgap single quantum dots, in *Single Semiconductor Quantum Dots*, ed. by Peter Michler (Springer, Berlin, 2009)
142. G. Chen, T.H. Stievater, E.T. Batteh et al., Biexciton quantum coherence in a single quantum dot. Phys. Rev. Lett. **88**(11), 117901–117904 (2002)
143. Special issue on high excitation and short pulse phenomena, J. Luminesc. **30**(1–4) (1985)
144. K. Herz, T. Kümmel, G. Bacher et al., Biexcitons in low-dimensional CdZnSe/ZnSe structures, phys. stat. solidi A **164**(1), 205–208 (1997)
145. B. Jusserand, M. Cardona in *Light Scattering in Solids*, ed. by V. M. Cardona, G. Güntherodt. Raman spectroscopy in Light scattering of vibrations in superlattice (Springer, Berlin, 1989) pp. 49–152
146. N. Balkan (ed.), *Hot Electrons in Semiconductors: Physics and Devices* (Oxford University Press, Oxford, 1998)
147. B.K. Ridley, Hot electrons in low-dimensional structures. Rep. Prog. Phys. **54**, 169–256 (1991)
148. B.K. Ridley, *Electrons and Phonons in Semiconductor Multilayers* (Cambridge University Press, Cambridge, 1997)
149. M. Babiker, Coupling of polar optical phonons to electrons in superlattice and isolated quantum wells. Semicond. Sci. Technol. **7**, B52–B59 (1992)
150. S. Das Sarma, V.B. Campos, M.A. Stroscio et al., Confined phonon modes and hot–electron energy relaxation in semiconductor microstructures. Semicond. Sci. Technol. **7**, B60–B66 (1992)
151. E. Molinari, C. Bungaro, M. Gulia et al., Electron–phonon interactions in two-dimensional systems: A microscopic approach. Semicond. Sci. Technol. **7**, B67–B72 (1992)
152. T. Tchuchiya, T. Ando, Electron–phonon interaction in semiconductor superlattice. Semicond. Sci. Technol. **7**, B73–B76 (1992)
153. H. Gerecke, F. Bechstedt, The electron–optical phonon interaction in semiconductor microstructures. Semicond. Sci. Technol. **7**, B80–B82 (1992)
154. B.-F. Zhu, Optical phonon modes in quantum wires. Semicond. Sci. Technol. **7**, B88–B90 (1992)
155. K.T. Tsen, Picosecond time–resolved Raman studies of electron–optical phonon interactions in ultrathin GaAs–AlAs multiple quantum well structures. Semicond. Sci. Technol. **7**, B191–B194 (1992)
156. T. Inoshita, H. Sakaki, Electron relaxation in a quantum dot: Significance of multiphonon processes. Phys. Rev. **B46**, 7260–7263 (1992)
157. R. Heitz, M. Grundman, N.N. Ledentsov et al., Multiphonon–relaxation processes in self-organized InAs/GaAs quantum dots. Appl. Phys. Lett. **68**, 361–363 (1996)
158. G. Abstreiter, G. Böhm, K. Brunner, et al. in *Optical Phenomena in Semiconductor Structures of Reduced Dimensions*, ed. by D.J. Lockwood, A. Pinzuk. Luminescence properties of GaAs quantum wells, wires, dots and antidots, NATO ASI Series E, Applied Sciences, vol 248 (Kluwer Academic Publishers, Dordrecht, 1993)
159. V.I. Pipa, V.V. Mitin, M. Stroscio, Acoustic phonon bottleneck in quantum dots: Role of deformation variation of electron effective mass. Solid State Commun. **117**, 713–717 (2001)
160. U. Bockelman, G. Bastard, Phonon scattering and energy relaxation in two-, one-, and zero-dimensional electron gases. Phys. Rev. **B42**, 8947–8951 (1990)

161. U. Bockelman, in *Inersubband Transitions in Quantum Wells,* Phonon scattering and relaxation properties of lower dimensional electron gases, NATO ASI Series B: Physics, vol 288 (Plenum Press, New York, 1993), pp. 105–118
162. H. Bensity, C.M. Sotomayor-Torres, C. Weisbuch, Intrinsic mechanism for the poor luminescence properties of quantum–box systems. Phys. Rev. **B44**, 10945–10948 (1991)
163. E. Burstein, C. Weisbuch, *Confined Electrons and Photons: New Physics and Applications* (Plenum Press, New York, 1995)
164. M.A. Stroscio, M Dutta, *Phonons in Nanostructures* (Cambridge University Press, Cambridge, 2005)
165. S. Kiravittaya, A. Rastelli, O.G. Schmidt, Advanced quantum dot configurations, Rep. Prog. Phys. **72**, 046502 (p. 34) (2009)
166. L. Challis (ed.), *Electron–Phonon Interaction in Low-Dimensional Structures* (Oxford University Press, Oxford, 2003)
167. N. Bannov, V. Mitin, M. Stroscio Confined acoustic phonons in semiconductor slabs and their interaction with electrons, phys. stat. sol. **(b) 183**, 131–138 (1994)
168. G. Yu, K.W. Kim, M.A. Stroscio et al., Electron–phonon scattering rates in rectangular quantum wires. Phys. Rev. **B50**, 1733–1738 (1994)
169. P. Yu, M. Cardona, *Fundamentals of Semiconductors* (Springer, Heidelberg, 1996)
170. L.D. Landau, E.M. Lifshitz, *Theory of Elasticity* (Science, Moscow, 1987). (in Russian)
171. S.A. Cavill, P. Hawker and A.J. Kent, *Carrier–phonon interactions in semiconductor quantum dots and wires*, ed. by L. Challis. Electron-Phonon Interactions in Low-Dimensional Structures (Oxford University Press, Oxford, 2010), pp. 115–147
172. J.S. Blakemore, Semiconducting and other major properties of gallium arsenide. J. Appl. Phys. **53**, R123–R181 (1982)
173. M.P. Blencowe, *Low-Dimensional Semiconductor Structures: Fundamentals and Device Applications*, ed. by K. Barnham, D. Vvedensky. Phonons in Low Dimensional Semiconductor Structures (Cambridge University Press, Cambridge, 2001), pp. 123–148
174. J.I. Pankove, *Optical Processes in Semiconductors* (Prentice Hall Inc., Englewood Cliffs, 1971)
175. F. Rossi, G. Goldoni, E. Molinari, Theory of excitonic confinement in semiconductor quantum wires. J. Phys. Condens. Matter **11**, 5969–5988 (1999)
176. A.V. Akimov, *Electron-Phonon Interactions in Low-Dimensional Structures*, ed. by L. Challis. Exciton–phonon interaction in quantum wires (Oxford University Press, Oxford, 2010), pp. 239–267
177. R. Cingolani, K. Ploog, Frequency and density dependent radiative recombination processes in III–V quantum wells and superlattice. Adv. Phys. **40**, 535–623 (1991)
178. J. Lee, E.S. Koteles, M.O. Vassel, Luminescence linewidths of excitons in GaAs quantum wells below 150 K. Phys. Rev. **B33**, 5512–5516 (1986)
179. H. Hillmer, A. Forschel, S. Hausman et al., Optical investigations on the mobility of two-dimensional excitons in GaAs/$Ga_{1-x}Al_xAs$ quantum wells. Phys. Rev. **B39**, 10901–10912 (1989)
180. R. Tsu, *Superlattice to Nanoelectronics* (Elsevier Science, Amsterdam, 2005)
181. J.H. Collet, H. Kalt, Le.Si. Dang et al., Relaxation of excitons in coherently strained CdTe/ZnTe quantum wells. Phys. Rev. **B43**, 6843–6846 (1991)
182. R.P. Stanley, J. Hegarty, R. Fischer et al., Hot–exciton relaxation in $Cd_xZn_{1-x}Te$/ZnTe multiple quantum wells. Phys. Rev. Lett. **67**, 128–131 (1991)
183. H.C. Casey, M.B. Panish, *Heterostructure Lasers* (Academic, New York, 1978)
184. P.S. Zoty, *Quantum Well Lasers* (Academic, Boston, 1993)
185. Y. Arakawa, in *Confined Electrons and Photons*: *New Physics and Applications,* Semiconductor Nano–Structure Lasers: Fundamentals and Applications, ed. by E. Burstein, C. Weisbuch. NATO Series B: Physics, vol 340 (Plenum Press, New York, 1995), pp. 647–673

186. L.A. Colderen, S.W. Corzine, *Diode Lasers and Photonic Integrated Cicuits* (Wiley, New York, 1995)
187. V.M. Ustinov, A.E. Zukov, A.Yu. Egorov, N.A. Maleen, *Quantum Dot Lasers* (Oxford University Press, Oxford, 2003)
188. N.N. Ledentsov, V.M. Ustinov, V.A. Shchukin et al., Quantum dot heterostructures: Fabrication, properties, lasers. Fiz. and Teh. Polup. (Physics and Technics of Semicond.) **32**(4), 385–410 (1998). (in Russian)
189. K. Ikeda, H. Seguchi, F. Minami et al., Phonon bottleneck effects in InAs/GaInP quantum dots. J. Luminesc. **108**, 273–276 (2004)
190. B. Damilano, N. Grandejan, J. Massies et al., GaN and GaInN quantum dots: an efficient way to get luminescence in the visible spectrum range. Appl. Surf. Sci. **164**, 241–245 (2000)
191. Y. Kuwahara, Y. Fujiyama, M. Iwaya et al., Nitrides based light–emitting solar cell, phys. stat. sol. **(c) 7**, 1807–1809 (2010)
192. K. Kuroda, T. Kuroda, K. Watanabe et al., Distribution of exciton emission linewidth observed for GaAs quantum dots grown by droplet epitaxy. J. Luminesc. **130**, 2390–2393 (2010)
193. I.I. Abramov, E.G. Novik Classification of single–electronics devices, Fiz. i Techn. Poluprov. (Phys. and Techn. Semicond.) **33**(11), 1388–1394 (1999) (in Russian)
194. A.V. Eletskii, Mechanical properties of carbon nanostructures and related materials. Uspekhi Fiz. Nauk (Moscow) **177**(3), 233–274 (2007). (in Russian)
195. M.A. Kastner, The single electron transistor. Rev. Mod. Phys. **64**(3), 849–858 (1992)
196. D.V. Averin, A.A. Odintsov, S.A. Vyshenski, Ultimate accuracy of single–electron dc current standards. J. Appl. Phys. **73**(3), 1297–1308 (1993)
197. Y. Ono, A. Fujiwara, K. Nishiguch et al., Manipulation and detection of single electrons for future information processing. J. Appl. Phys. **97**(3), 031101–031119 (2005)
198. N.N. Ledentsov, V.M. Ustinov, V.A. Shchukin et al., Quantum dot heterostructures: Fabrication, properties, lasers. Fiz. and Teh. Polup. (Physics and Technics of Semicond.) **32**(4), 385–410 (1998). (in Russian)
199. J.M. Martinez–Duart, R.J. Martin–Palma, F. Agullo–Rueda, *Nanotechnology for Microelectronics and Optoelectronics* (Elsevier, Amsterdam, 2006)
200. L. Sirigu, D.Y. Oberli, L. Deriorgi et al., Excitonic lasing in semiconductor quantum wires. Phys. Rev. **B61**(10), R10575–R10584 (2000)
201. S.M. Sze, *Physics of Semiconductor Devices* (Wiley, New York, 1981)
202. P.W. Shor, Polynomial–time algorithm for prime factorization and discrete logarithms on a quauntum computers. SIAM J. Comput. **26**(4), 1494–1509 (1997)
203. L.K. Grover, Quantum mechanics helps in searching for a needle a haytack. Phys. Rev. Lett. **79**(2), 325–328 (1997)
204. R.P. Feynman, Stimulating physics with computers. Int. J. Theor. Phys. **21**(2), 467–488 (1982)
205. V.G. Plekhanov, Quantum information and quantum computation, Transactions of Computer Science College, No 1, Tallinn, 2004, pp. 161–282 (in Russian)
206. V.G. Plekhanov, Isotopetronics and quantum information, deposited in VINITI (Moscow) N 425–B2011 from 28.09.2011 (unpublished)
207. P. Shor, Scheme for reducing decoherence in quantum memory. Phys. Rev. **A52**(4), 2493–2496 (1995)
208. A.M. Steane, Error correction codes in quantum theory. Phys. Rev. Lett. **77**(5), 793–796 (1996)
209. A.M. Steane, Quantum computing. Rep. Prog. Phys. **61**(2), 117–173 (1998)
210. G. Benenti, G. Casati, G. Strini, *Principles of Quantum Computation and Information* (World Science, Singapore, 2005)
211. J. Preskill, Reliable quantum computers. Proc. R. Soc. (London) **A454**(2), 385–410 (1998)
212. B.E. Kane, A silicon–based nuclear spin quantum computer. Nature **393**(1), 133–137 (1998)
213. B.E. Kane, Silicon–based quantum computation. Fortschr. Phys. **48**(4), 1023–1041 (2000)

214. A.M. Tyryshkin, S.A. Lyon, A.V. Astashkin, Electron spin relaxation times of phosphorus donors in silicon. Phys. Rev. **B68**(9), 1932074 (2003)
215. D.K. Wilson, G. Feher, Electron spin resonance on donors in silicon. Phys. Rev. **124**(4), 1068–1083 (1961)
216. J.S. Waugh, C.P. Slichter, Mechanism of nuclear spin–lattice relaxation in insulators at very low temperatures. Phys. Rev. **B37**(8), 4337–4339 (1988)
217. B.E. Kane, N.S. McAlpine, A.S. Dzurak, B.G. Clark, Single spin measurement using single–electron transistors to probe two–electron systems. Phys. Rev. **B61**(4), 2961–2972 (2000)
218. A.J. Skinner, M.E. Davenport, B.E. Kane Hydrogenic spin quantum computing in silicon, Phys. Rev. Lett. **90**(8), 087901–087904 (2003)
219. J.R. Tucker, T.C. Shen, The road to a silicon quantum computer. Quant. Inform. Processing **3**(1–5), 105–112 (2004)
220. X. Hu, Spin–based quantum dot quantum computing, ArXiv: cond - mat/0411022 (2004)
221. R. Vrijen, E. Yablonovich, K. Wang et al., Electron spin resonance transistors for quantum computing in silicon–germanium heterostructures. Phys. Rev. **A62**, 12306–12309 (2000)
222. I. Shlimak, V.I. Safarov, I. Vagner, Isotopically engineered Si/SiGe nanostructures as basic elements for a nuclear spin quantum computer. J. Phys. Condens. Matter **13**, 6059–6065 (2001)
223. I. Shlimak, I. Vagner, Quantum information processing based on ^{31}P nuclear spin qubits in a quai–one-dimensional ^{28}Si nanowire. Phys. Rev. **B75**(4), 045336–045346 (2007)
224. I. Shlimak, V. Ginodman, A. Butenko et al., Electron transport in a slot–gate Si MOSFET, ArXiv: cond - mat./0803.4432
225. F. Schäffler, High–electron–mobility Si/SiGe heterostructures: Influence of the relaxed buffer layer. Semicond. Sci. Technol. **7**(2), 260–267 (1992)
226. V.G. Plekhanov, Isotopetronics–new direction of nanoscience, ArXiv: gen. ph/ 1007.5386 (2010)
227. V.G. Plekhanov, Isotopes in quantum information, Preprint N 2 of Computer Science College, Tallinn (2007) (in Russian)
228. D.P. DiVincenzo, Two–bit are universal for quantum computation. Phys. Rev. **A51**(2), 1015–1022 (1995)
229. D.P. DiVincenzo, Quantum computation. Science **270**, 256–261 (1995). 13 Oct

Index

V. G. Plekhanov, *Isotope Low-Dimensional Structures*, SpringerBriefs in Physics,
DOI: 10.1007/978-3-642-28613-1, © The Author(s) 2012